Electronic and Magnetic Properties of Metal Doped Silicon-Carbide Fullerene-type Nanostructures

By Hussain Jabreel Alathlawi

DISSERTATION

Presented to the Faculty of the Graduate School in Partial fulfillment

Of the Requirements for the Degree of Doctor of Philosophy at

THE UNIVERSITY OF TEXAS AT ARLINGTON

December 2021

Supervising Committee:

Muhammad N. Huda, Supervising Professor

Zdzislaw Musielak

Qiming Zhang

Ali Koymen

Mingwu Jin

Acknowledgments

First and foremost, I want to express my gratitude to Dr. Muhammad Huda, my PHD supervisor, for his invaluable advice, unwavering support, and patience throughout my studies. His vast knowledge and wealth of experience have inspired me academically throughout my research and my daily life. I was extremely fortunate to have a supervisor who was genuinely concerned about my work and who responded to my questions and concerns in timely manner. I can still feel it, and I cannot thank him enough for everything he has done for me. Without his assistance, I would not have been able to succeed in this field.

I would also want to thank my committee members, Dr. Ali Koymen, Dr Mingwu Jin, Dr. Zdzislaw Musielak, Dr. Qiming Zhang for their, assistance, and guidance. I have had the pleasure of taking their classes and furthering my knowledge as a result of their focused guidance.

I am grateful to the Saudi Arabian Cultural Mission (SACM) at the United States and Jazan University for the financial support I have received. Also, I gratefully acknowledged the generous computation time at the High-Performance Computing (HPC) Center of the University of Texas at Arlington and Texas Advanced Computing Center (TACC).

I am very grateful to my parents and siblings for supporting me with their best to complete my degrees in the United States of America. Last but not the least, I am very much thankful and grateful to my wife, Naemah Zaeri, and my sons, Basam and Hussam Alathlawi for their commitment, support, patient, and encouragement in keeping me on track for the completion of my doctoral degree.

This work is dedicated to my parents, Jabreel Alathlawi and Madiah Magaly,

And to my devoted wife, Naemah Zaeri, and my sons, Basam and Hussam Alathlawi,

as well as my siblings.

Abstract

Silicon carbide (SiC) is a technologically significant material. A recent report on the abundance of C_{60} fullerenes in interstellar space, along with the presence of SiC precursors, sparked interest in potentially similar SiC nanostructures. C_{60} and C_{70} fullerenes were found experimentally and are an exceptionally stable form of carbon. As Si and C have similar valence electron configurations, it has been long envisioned that Si and SiC could also form similar fullerene-type structures. In this dissertation, $Si_{30}C_{30}$ fullerene-derived clusters were studied from the first principles theory, starting from an ideal Si_{60} fullerene template with various arrangements of silicon and carbon atoms and then relaxing them without any symmetry constraint. Hydrogen passivation was considered as well to model the effect of ligands that may be available during chemical synthesis processes. We have found that, after passivation, the relative stability order of different configurations of $Si_{30}C_{30}$ clusters (isomers) changed compared to the unpassivated structures, while some structures collapsed. We have also noticed several Si–Si and Si–C double bonds on the unpassivated structures.

Endohedral doping of several transition metal atoms (Fe, Nb, Hf, Ta, and W) atoms in C_{60}, C_{70}, $Si_{30}C_{30}$ (sphere structure), and $Si_{35}C_{35}$ structures was then considered. The doping was found to increase binding energy compared to original structures without doping. On the other hand, Fe, Nb, Hf, Ta, and W atoms in the center of C_{60}, C_{70}, $Si_{30}C_{30}$ (sphere structure), and $Si_{35}C_{35}$ structures maintained a significant value of magnetic moments. With hydrogen passivation, the magnetic moment on W atom was enhanced. Moreover, rare-earth atoms (La, Ce, Pr, and Nd) have been studied as doping atoms in C_{60}, C_{70}, $Si_{30}C_{30}$ (sphere structure), and $Si_{35}C_{35}$ structures. They help to increase the stability of structures and decrease the diameter. Also, Pr and Nd doped atoms hold a high value of magnetic moments inside fullerenes.

We present ab initio molecular dynamic (AIMD) simulation on endohedral doping structures in $Si_{30}C_{30}$ (sphere structure), and $Si_{35}C_{35}$ structures. Overall, the result shows the magnetic moment decreases on some of the transition metals (Nb, Hf, Ta, and w) and rare-earth (La and Ce) atoms as the temperature increases. On the other hand, the Fe, Pr, and Nd atoms maintain the value of magnetic moments at $Si_{30}C_{30}$ (sphere structure) while the temperature increases up to 300K. For $Si_{35}C_{35}$ structures, the Nd atom has showed a good value of magnetic moment up to 300K. The overall spherical nature was maintained for the SiC fullerenes as the temperature increases.

Our study in the dissertation provides a fundamental understanding of the SiC fullerenes, their stabilities and magnetic moments at room temperature. The study will motivate their synthesis and applications in electronic and magnetic devices in near future.

Contents

CHAPTER 3:

CHAPTER 4:

Chapter 1

1.1. Introduction

Despite the development of electronic industries, there are still challenges in memory devices capacity. Studying fullerenes can help in the spintronic application, where electron spins can be used in solid-state electronics[1]. Furthermore, monitoring and control of the spin provide a degree of flexibility to solid-state devices, allowing the construction of innovative devices. Also, fullerene can help in electrical transport in semiconductors[2] [3]. So far, fullerenes have been used to develop a variety of industrial applications, including solar cells, superconductors, and molecular electronics [4].

Palmer and Shelef published the quantitative overview of early studies on carbon clusters in their article on the composition of carbon vapor in 1968[5]. However, much progress has been achieved in the meantime, and the general situation has been updated by Weltner and Van Zee[6]. In 1985 the fullerene was discovered[7]. Fullerenes are one of the most prominent groups of structures, and since discovery they enjoyed a significant focus on current material nanoscience study. Buckminsterfullerene (C_{60}) is the most common fullerene, containing 60 carbons atoms organized in a spherical shape. The structure is made up of 20 hexagons and 12 pentagons [8][9][10]. Fullerenes are very stable materials that can withstand tremendous pressure; after being exposed to over 3,000 atmospheric pressure[7]. The presence of the fullerenes as a group has been proven, and it is reasonable to adopt a name that can apply to the entire group; for example, C_{60} fullerene or C_{70} fullerene. C_{60} and C_{70} are large clusters of carbon atoms. Moreover, in crystalline carbon, C_{60} and C_{70} fullerenes have been thoroughly studied for physical and chemical properties[11] [12][13].

Fullerenes' response to the optical limiting phenomena and intensity-dependent index of refraction offers promises in terms of protecting eyes and sensors from strong light sources. In addition, fullerenes are the finest acceptor component currently accessible due to their strong electron affinity and a great capacity to transfer charge[14][15]. The fullerene has the potential to expand niche applications in chemically synthesized electronic devices requiring high-quality organic memory that is consistent with other devices such as transistors, light-emitting diodes, and solar cells[16]. The fullerene is a valuable molecular device with applications in medicinal chemistry and materials research[11] [12][13]. Electro-active and optical restricting features can be accomplished due to the integration of fullerene in the polymers. This might primarily be used in surface coating.[17] C_{60} Fullerene has shown great promise in biological and medical applications. C_{60} fullerene, for example, is an excellent free radical scavenger. Therefore, it may be employed as a cell protector or to minimize oxidation stress. In addition, fullerene is an interesting molecule for controlled medication release. The reason is that they are multifunctional; they can act as drug "absorbance" to generate nanometric particles[18][19][20].

There is a new astronomical discovery that found a great number of C_{60} fullerenes in interstellar space. Under the specific condition, SiC nanoclusters generated around dead stars were hypothesized as the forerunner for producing these interstellar C_{60} fullerenes [21]. Previous research demonstrated that $Si_{60}H_{60}$ [22] has good symmetry and is energetically stable because of the strong bonds among both Si and H. $Si_{60}H_{60}$, however, has weaker Si-Si bonds compared to less stable unpassivated Si_{60} fullerene due to the lack of the sp^2 hybridization between Si-Si bonds in $Si_{60}H_{60}$ fullerene [23]. Silicon fullerenes are comparable to C_{60} fullerene due to the similar valance electrons properties of Si and C atoms. Based on that, SiC can form similar fullerene-type structures. Previous research has shown that Si_mC_n ($m + n = 60$) clusters can form before

transforming into C_{60} [24] or other carbon-based structures. Also, the stable configurations of large fullerene clusters, $C_{40}Si_{20}$, $C_{36}Si_{24}$, and $C_{30}Si_{30}$, were recently documented theoretically [24]. Moreover, the theoretical research on $Si_{60}C_{2n}$ (n = 1, 2), $Si_{40}C_{20}$, $Si_{36}C_{24}$, and $Si_{60}C_{20}$ showed that the SiC fullerenes have higher stability than the pure Si_{60} fullerene [25][26][27], where the stable fullerenes consist of the carbon structures inside or on the surface of the fullerene. Theoretical research reported different stable isomers of smaller fullerenes $Si_{20}C_n$ clusters with endohedral doping of carbon atoms [28]. However, silicon carbide (SiC) and Si fullerenes can be modeled after C_{60} fullerene. Si atom preferred Sp^3 bonds, which means Si_{60} fullerene will not be entirely symmetrical and stable like C_{60} fullerene, as shown in some published works [29][23][30][31]. Moreover, $C_{30}Si_{30}$ fullerene was found the most stable structure among Si_mC_n (m + n = 60) clusters [32][33]. Note, in these published works, the relative thermodynamic stability was obtained by DFT that ignores the temperature effects. However, the most stable system can become dynamically unstable at higher temperatures, and a comparatively less stable structure can be dynamically more stable at higher temperatures [34]. Stability with respect to increasing temperature for these SiC fullerenes were not studied in the previously mentioned published literature.

1.2. Motivation

In spherical cage structures, it is possible to enclose atoms or molecules inside the hollow of the fullerenes; this is called endohedral doping of fullerenes. Research on endohedral doping of metal atoms in C_{60} has been reported, for example, $Li@C_{60}$ [35][36], $Rb_3@C_{60}$, and $K_3@C_{60}$ compound [37][9]. Also, others studied different types of endohedral doping on larger cage-type fullerenes, such as $Sc_2@C_{66}$, $Sc_3N@C_{68}$, $Sc_3N@C_{82}$, $Sc_2@C_{68}$, [38][39]. Several endohedral dopants were examined in Si cages[40][41][41] to stabilize and develop fullerene-

like structures materials with customized properties. In addition, in the twenty-first century, the endohedral metal doping fullerene has been intensively studied in the organic spintronics field. The reason is that the doping atoms can have a significant magnetic moment in the center of the cage. The SiC fullerenes are used in various technical applications, including power electronics[42][43][44][45][46]. So, studying endohedral doping of $Si_{30}C_{30}$ and $Si_{35}C_{35}$ could be useful in new-generations electronic applications.

1.3. Literature Reviews on Fullerenes and Endohedral Doping

C_{60} fullerene has been studied experimentally at room temperature, where the single and double bonds were found with bond lengths of 1.391 Å and 1.455 Å, respectively [47]. In addition, the molar volume is V= 429 cm^3 mol^{-1}, and the square root of the cohesive energy density is = 9.8 $cal^{1/2}$ $cm^{-3/2}$ of C_{60} was found in another experimental study at room temperature [48]. Also, reported diameter, electron affinity (EA), ionization potential (IP), and highest occupied molecular orbital (HOMO)-lowest unoccupied molecular orbital (LUMO) gaps of the C_{60} fullerene are 7 Å, 2.6-2.8 eV, 7.61 eV [8], and 6.8V [49], respectively. A theoretical study of C_{60} fullerene has reported a value of HOMO-LUMO gap of 2.723 eV [50]. C_{60} was found to be a magic number regardless of whether carbon type was negatively, positively, or naturally charged by beam cluster study [51][8][52]. $C_{48}B_{12}$ and $C_{48}N_{12}$ have been theoretically (DFT) reported as accepter and donor fullerenes[53]. Where another theoretical study of $C_{48}N_{12}$ structure shows a value of HOMO-LUMO gap by 2.72 eV. [54]. A biological study on C_{60} reported that it is not carcinogenic on the skin. The C_{70} fullerene is another type of fullerene that that was reported as a stable structure[8]. An experimental study of C_{70} molecular structure reports between 20 and 300K. The C-C bond

lengths have a longer range than C_{60}, where the lengths of the C-C bonds ranges between 1.38 and 1.48A [55]. Moreover, the binding energy per atom and diameter between the polar pentagons have been reported experimentally, which are 7.42 eV and 7.906 Å [56][57].

According to theoretical studies, Si_{60} is not as energetically stable as C_{60} fullerene. Furthermore, the C_{60} encapsulated inside a Si_{60} was found to be energetically unstable. [30][58] [30] [22][23]. Furthermore, the C_{60}, C_{24}, and C_{20} encapsuled within the Si_{60} study are energetically unstable. On the other hand, $Si_{40}C_{20}$ and $Si_{36}C_{24}$ fullerene-like structures are more stable than Si_{60} fullerene. The reason is that the Si-C and C-C interactions are stronger on the surface than inside the fullerene [25]. Similar theoretical research reported that for these sizes of SiC fullerenes, the higher the number of Si atoms in the SiC cluster make the structure relatively less stables [58]. On the other hand, increasing number of C-C bonds in segregated $Si_{12}C_{12}$ clusters would increase the stability of these structures [59]. Indeed Si-C interactions have a role in the stability of the $Si_{20}C_n$ cluster [60]. According to the thermodynamic stability analysis of $Si_{30}C_{30}$, the more stable structure at 0K might be dynamically unstable at higher temperatures [34][61].

C_{60} fullerene is a spherical cage structures[8], and it is possible to dope atoms or molecules inside the hollow cage of the fullerenes; the endohedral doping of fullerenes. Research on endohedral doping of metal atoms in C_{60} has been reported, for example, $Li^+@C_{60}$ is an endohedral fullerene that address the problem of solar cell stability [35][36]. The theoretical study of Li atom movement between the faces of the isolated molecule has been examined, suggesting that the Li may move between local minima at high temperatures[62][63]. Spectroscopic evidences showed the mobility of Li atom inside the cage at a temperature over 100-150K[64][36][65]. The investigation of $K@C_{60}$ in the thin film revealed a zero resistance around 5K [37]. Another study reported that magnetic moment of superconducting particles of alkali metal doped fullerenes

$Rb_3@C_{60}$ and K_2RbC_{60} revealed significant hysteresis, as expected for non-ideal superconductors[66][37][9]. The $Gd@C_{60}$ has been studied for biological applications, that reports interaction energy between endohedral doping and Lysozyme by -18.7 Kcal/mole[45], where the double and single C-C bonds are 1.39 and 1.45, respectably[67]. There is a theoretical and experimental study on the $Be@C_{60}$. The study starts at 0.1 fs, the basic time step, and the temperature 1000K. The result shows that the C_{60} cage was damaged when the Be atom had 100 eV kinetic energy[43]. There are experimental studies of La[35], Y, and Sc at C_{82} and C_{84} fullerenes [68][69][70][71][72]. The La atom has been studied inside C_{60}, C_{70}, and C_{84}. The studies report that La atom is more stable within the C_{60} cage; the La atom within C_{60} gives its 6s electrons to the carbon cage's delocalized aromatic shell system[73][68]. Theoretically study of $Sc_2S@C_{72}$ and $Sc_2S@C_{70}$ has been reported. The result showed that the spin densities of endohedral doping are the same as molecular orbitals distributed on the cage surface[74]. The noble-gas atoms (He, Ar, Ne, Xe, Kr)[75][76], P, and N[76] have been theoretically study in the center of C_{70} fullerene as well.

1.4. The Goal of the Study

As mentioned above, it is possible to add atoms at the center of fullerenes to study electronic and magnetic properties. The first goal of this dissertation is to investigate the electronic and magnetic properties of endohedral C_n fullerenes; n = 60 or 70 and Si_mC_n fullerenes; m = n = 30 or 35 atoms because there is no study yet on the endohedral doping of $Si_{30}C_{30}$ and $Si_{35}C_{35}$fullerenes. The doping atoms will be transition metal atoms (M); (M=Nb, Fe, Hf, Ta, and W) and rare-earth atoms (R); (R=La, Ce, Pr, and Nd). The second goal is to study the effects of hydrogen passivation on Si_mC_n isomers. The third goal is how increasing temperature affects the stability and magnetic moment properties on endohedral doped $Si_{30}C_{30}$ and $Si_{35}C_{35}$ fullerenes. This study of this

dissertation will provide a fundamental understanding of the SiC fullerenes that will guide their synthesis and various applications.

The theoretical approaches and systematic studies are described in the following chapters. The density functional theory provides the theoretical basis for our work, briefly explained in chapter 2. In chapter 3, pristine fullerene of C_{60}, Si_{60}, $Si_{30}C_{30}$, C_{70}, and $Si_{35}C_{35}$, are presented in detail, and the effects of hydrogen passivation of $Si_{30}C_{30}$ isomers are discussed. Chapter 4 discusses the electronic and magnetic properties for transition metal atoms doping (Nb, Fe, Hf, Ta, and W) in $C_{60,}$ $Si_{30}C_{30}$ C_{70}, and $Si_{35}C_{35}$ fullerenes. In chapter 5, the electronic and magnetic properties are discussed for rare earth atoms doping [La, Ce, Nd, and Pr]. Chapter 6 shows the effect of temperature on the magnetic and electronic properties of endohedrally doped transition metal and rare earth atoms in $Si_{30}C_{30}$ and $Si_{35}C_{35}$ fullerenes. The effect of temperature was calculated by using ab initio molecular dynamics (AIMD) simulations. Finally, in chapter 7, the conclusion of our work and an overall direction about future work will be presented.

Chapter 2

Methodology

2.1 Density Functional Theory (DFT)

The theoretical framework of this study is Density Functional Theory (DFT), which is implemented in supercomputing systems at Texas Advanced Computing Center (TACC) in Austin, TX using Gaussian 09 [77] code and Vienna Ab initio Simulation Package (VASP) [78][79][80][81]. It is currently one of the most successful theories used to analyze crystal structures and electronic condensed matter for more than two decades. Every year, more than 1500 publications are published in the density functional theory (DFT) framework throughout all scientific fields.

The best way to understand Solid State Physics or condensed matter is to study the subject at its most accurate and fundamental level. This type of research can lead to the discovery of condensed matter's substantial properties and the effects of numerous imperfections. Density functional theory (DFT) is an example of a tool that can be useful in a field where academics have been successfully employing it for over three decades. It is now the most successful and promising method for computing matter’s electronic structures. Besides, it is applied to molecules, solids, atoms, nuclei, and quantum and classical fluids. This theory is aimed to provide the ground state features of materials, and the electron density is its key entity.

The fundamental theory driving the computational calculations performed in this dissertation is detailed in the following sections. The original work of density functional theory was presented in two articles published in 1964 and 1965 by Hohenberg and Kohn, and Kohn and Sham, [78][79]respectively.

2.1.1 The Electronic Many-Particle Problem

The Most pertinent concern in condensed matter theory is how to deal with many particles systems within a quantum mechanical framework. The density functional theory can deal with a large system with many interacting particles. So, for many-particle systems, the calculation starts from the time-independent, non-relativistic Schrödinger equation for solid-state, atomic, and molecular materials.

$$\hat{\mathrm{H}}\Psi = E\Psi \tag{2.1.1}$$

where $\hat{\mathrm{H}}$ is a Hamiltonian operator, E is the system's energy, and Ψ the wavefunction. So, the Hamiltonian operator of a non-relativistic many-particle system is written as

$$\hat{\mathrm{H}} = -\frac{\hbar^2}{2m}\sum_i^N \boldsymbol{\nabla}_i^2 - \frac{\hbar^2}{2M_I}\sum_I^M \boldsymbol{\nabla}_I^2 - \sum_{i=1}^N \sum_{I=1}^M \frac{Z_I e^2}{4\pi\epsilon_0 |r_i - R_I|} + \frac{1}{2}\sum_{i=1}^N \sum_{j>i}^N \frac{e^2}{4\pi\epsilon_0 |r_i - r_j|} + \frac{1}{2}\sum_{I=1}^M \sum_{J>I}^M \frac{Z_I Z_J e^2}{4\pi\epsilon_0 |R_I - R_J|} \tag{2.1.2}$$

The first and second terms in equation (2.1.2) represent the electronic and nuclei kinetic energy, the third term is electron-nuclei interactions, the fourth term describes electron-electron interactions, and the last term represents nuclei-nuclei interactions. Also, the indicate N, i, and j represent the electrons and M, I, J represent nuclei counting indices, *m* donates an electron mass, and M_I for nuclei mass, *e* the elementary charge, $4\pi\epsilon_0$ coulombs constant, and ħ Planck constant. In this Hamilton equation (2.1.2), the most challenging part to dealing with is the electron-electron interactions (fourth term) which makes the Hamilton equation (2.1.1) very difficult to solve. However, we may simplify it by using the Born-Oppenheimer approximation, which is described in the following.

2.1.2 Born-Oppenheimer Approximation.

The Born-Oppenheimer approximation considers that nuclei are considerably heavier than electrons, and nuclei have lower velocities than electrons. As a result of the Born-Oppenheimer approximation, we can separate electron and nuclei motions and consider the components in the equation that correspond to electron states independently from atomic nuclear states. As a result, the many-particle system may be simplified to an electronic Hamiltonian:

$$\hat{H}_{elec} = -\frac{\hbar^2}{2m}\sum_i^N \boldsymbol{\nabla}_i^2 - \sum_{i=1}^N \sum_{I=1}^M \frac{Z_I e^2}{4\pi\epsilon_0 |r_i - R_I|} + \frac{1}{2}\sum_{i=1}^N \sum_{j>i}^N \frac{e^2}{4\pi\epsilon_0 |r_i - r_j|} \quad (2.1.3)$$

Or more compactly

$$\hat{H}_{elec} = T + V_{ext} + V_{ee}\,. \quad (2.1.4)$$

where T is the kinetic energy operator for electrons and V_{ee} electrons coulomb interaction potential. V_{ext} external potential generated by the nuclei of the materials. Due to the Born-Oppenheimer approximation, the nuclei are external fixed objects which exert their coulomb potential to the electrons.

The many bodies Schrödinger equation can be written as:

$$H\psi = (T + V_{ext} + V_{ee})\psi = E\psi \quad (2.1.5)$$

The expectation value of the Hamiltonian yield the total energy of the system.

$$E = \langle \psi | H | \psi \rangle \quad (2.1.6)$$

$$E = T + V_{ee} + \int d^3r\, V_{ext}(r)\, n(r) \quad (2.1.7)$$

Here $n(r)$ is the electron density. The role of electron density in the formulation of density functional theory (DFT) must first be understood; thus, it is introduced here. The following section briefly explains the shift from equation (2.1.6), a wave function-based formalism to the electron density approach. As a result, it is critical that we take a step bake before moving forward.

2.2 Density Functional Theory.

Density functional theory (DFT) is a theory that can be described in two steps which are: First, the DFT theorems offered by Hohenberg-Kohn in their paper[78], then there's Kohn and Sham[79] formalism, which translates multi-electron representations into single-particle treatment. However, before these two steps, it is worth summing up the background of DFT.

- **Hartree and Hartree-Fock Approach**

The assumption behind the Hartree approach is non-interacting electrons. As a result, each electron, *i*, should satisfy the following Schrodinger equation

$$\mathrm{H_{eff}}\,\psi_i(\mathrm{r}) = \left(-\frac{1}{2}\nabla^2 + \mathrm{V_{(eff)}}\right)\psi_i(\mathrm{r}) = \epsilon_i\psi_i(\mathrm{r}). \qquad (2.2.1)$$

The effective Hamiltonian is $\mathrm{H_{eff}}$ and electrons move in an effective potential $\mathrm{V_{eff}}$. The eigenstates define the ground state in this approach, which follows the Pauli principle. This approach, however, has a significant drawback in terms of determining the $\mathrm{V_{eff}}$ which here is a mean-field potential experienced by an electron generated by the rest of the electrons in the many-electron system. Here the total energy is the sum of ϵ_is, and the system's wave-function is the product of the single particle wavefunctions $\psi_i(\mathrm{r})$, known as Hartree product.

2.2.1 Hohenberg-Kohn Theorem.

Hohenberg and Kohn established density functional theory (DFT) as an accurate quantum mechanical theory in 1964 by proving two theorems[78].

First theorem:

A many Bodies system's ground state energy is a unique functional of ground-state electron density, $n(r)$. Furthermore, two distinct V_{ext} cannot provide the same exact ground-state electron density. Assume that two different external potentials are compatible with the same non-degenerate ground state density $n(r)$. Let the potentials be referred to as V_a and V_b.

The ground state charge density n(r) for *N* electrons

$$n(r) = \sum_{i=1}^{N} |\Psi(r)|^2. \quad (2.2.3)$$

The Hamiltonians determine by their potentials, H_a and H_b:

$$H_b = T + V + V_{b(ext)}\ ,\ H_a = T + V + V_{a(ext)} \quad (2.2.4)$$

Associate with each H_a and H_b a ground state eigenfunction ψ_0 and eigenvalue E_0.

$$(H_a\ \psi_{0a} = E_{0a}\psi_{0a},\quad H_b\ \psi_{0b} = E_{0b}\psi_{0b}) \quad (2.2.5)$$

Therefore, ψ_{0a} and ψ_{0b}, respectively, are different, and we can use ψ_{0b} as trial wave function for $\hat{H}$. We are going to use the Variational theorem: the expectation value of H_a over the wave function ψ_{0b} must be higher than or equal to the ground state energy of ψ_{0a}.

$$E_{0a} \leq < \psi_{0b}|H_a|\psi_{0b} > \quad (2.2.6)$$

$$E_{0a} \leq \int <\psi_0 b\ |\ H_a\ - H_b|\psi_{0b}> + < \psi_{0b}|\ H_b|\psi_{0b}> = E_{0b} + \int n(r)\ [\ v_a\ - v_b]\ dr \quad (2.2.7)$$

Similarly for the HamiltonianH_b,

$$E_{0b} \leq \int <\psi_0 a \mid \mathrm{H}_b - \mathrm{H}_a|\psi_{0a}> + <\psi_{0a}| \mathrm{H}_a|\psi_{0a}> = E_{0a} + \int n(r)\,[v_b - v_a]\,dr \qquad (2.2.8)$$

The sum of equations (2.2.7) and (2.2.8) to get

$$E_{0a} + E_{0b} \leq E_{0b} + E_{0a} \qquad (2.2.9)$$

which is not possible. Hence. From we can say conclude that there cannot be two different V_{ext} that produce the same ground-state electron density.

Second theorem:

The ground state energy can be obtained variationally: the density that minimizes the total energy is the exact ground-state density.

$$E[n(r)] \geq E_{\mathrm{gs}}[n(r)] \qquad (2.2.10)$$

2.2.2 The Kohn-Sham Method:

The Kohn-Sham method is a mapping a many-particle system to a non-interacting single particles system, assuming the same charge densities for real and hypothetical non-interacting many-particles.

In equation (2.1.7), we can rewrite the expression for the total energy differently by combining the first two terms as a universal functional.

$$\mathrm{E} = T[\mathrm{n(r)}] + U_{ee}[\mathrm{n(r)}] + \int d^3r\, V_{ext}(r)\, n(r) = F[n(r) + \int d^3r\, V_{ext}(r)\, n(r) \qquad (2.2.11)$$

where, $F[n(r)] = T[\mathrm{n(r)}] + V_{ee}[\mathrm{n(r)}]$

Here $F[n(r)]$ is the universal functional, and it is not dependent on the external potential $V_{ext}(r)$. The $T[\mathrm{n(r)}]$ and $V_{ee}[\mathrm{n(r)}]$ unknown, and we need to evaluate them.

It's important to consider both the classical Coulomb interaction and the quantum mechanical properties of the electrons in the system. As a result, the electrons are non-interacting and form a homogeneous ideal gas. The universal functional equation is shown as:

$$F[n(r)] = T_s[n(r)]+U[n(r)]+E_{XC}[n(r)]. \quad (2.2.12)$$

$$\text{Where } U[n(r)] = \frac{1}{2}\int \frac{n(r)\, n(r')}{|r-r'|}\, dr\, dr' \quad (2.2.13)$$

The T_s [n(r)] is the kinetic energy of the independent particles, U [n(r)] the classical Coulomb interaction energy, and E_{XC}[n(r)] all of the many-body effects of electron-electron interactions are integrated into a single entity termed the exchange-correlation energy functional. Now, the total energy of equation (2.2.11) can be written as,

$$E[n(r)] = T_s[n(r)]+= \frac{1}{2}\int \frac{n(r)\, n(r')}{|r-r'|} dr\, dr' + \int n(r) V_{ext}(r)\, dr + E_{XC}[n(r)]. \quad (2.2.14)$$

Applying the variational principle to the total energy functional (2.2.14) to get

$$\mu = \frac{\delta E[n(r)]}{\delta\, n(r)} = \frac{\delta T\,[n(r)]}{\delta^{s} n(r)} + \frac{1}{2}\int \frac{n(r')}{|r-r'|}\, dr' + V_{ext}(r) + \frac{\delta E_{XC}[n(r)]}{\delta\, n(r)} \quad (2.2.15)$$

where μ is known as chemical potential, also known as the Lagrange multiplier. Although the exact functional for E_{xc}[n(*r*)], as shown in equation (2.2.14), is not yet accessible, various approximations have been constructed and utilized to compute the total energy of many-particle systems using the DFT framework; these will be discussed in the next section.

We can use the variational principle to calculate the total energy of the hypothetical non interacting system. Additionally, electrons are thought to be moving in the field of an effective potential. The energy functional is:

$$E[n(r)] = T_s[n(r)] + \int d^3 r\, V_{eff}(r)\, n(r). \quad (2.2.16)$$

Now we apply the variational principle to equation (2.2.16) to get

$$\mu = \frac{\delta E[n(r)]}{\delta\, n(r)} = \frac{\delta T\,[n(r)]}{\delta\, n(r)} + V_{eff}(r) \qquad (2.2.17)$$

So, equations (2.2.15) and (2.2.17) can be simplified as

$$V_{eff}(r) = \frac{1}{2}\int \frac{n(r')}{|r-r'|}\, dr' + V_{ext}(r) + \frac{\delta E_{XC}[n(r)]}{\delta\, n(r)} \qquad (2.2.18)$$

Where $\frac{\delta E_{XC}[n(r)]}{\delta\, n(r)} = V_{XC}(r)$ (2.2.19)

The $V_{XC}(r)$ is the exchange-correlation potential.

The effective potential now converts the many-particle problems to a single particle form, and the equivalent effective Hamiltonian for this scenario is

$$H_{eff} = -\frac{1}{2}\nabla^2 + V_{(eff)}. \qquad (2.2.20)$$

Then, the single-particle Schrödinger equation will be

$$H_{eff}\,\psi_i(r) = \left(-\frac{1}{2}\nabla^2 + V_{(eff)}\right)\psi_i(r) = \epsilon_i \psi_i(r). \qquad (2.2.21)$$

Where, $\psi_i(r)$ are the Kohn-Sham orbitals and ϵ_i are the energy eigenvalues of Kohn- Sham equation.

For solving the Kohn-Sham equation for many-body problems, a flow chart diagram of the density functional theory self-consistent loop is shown in the following.

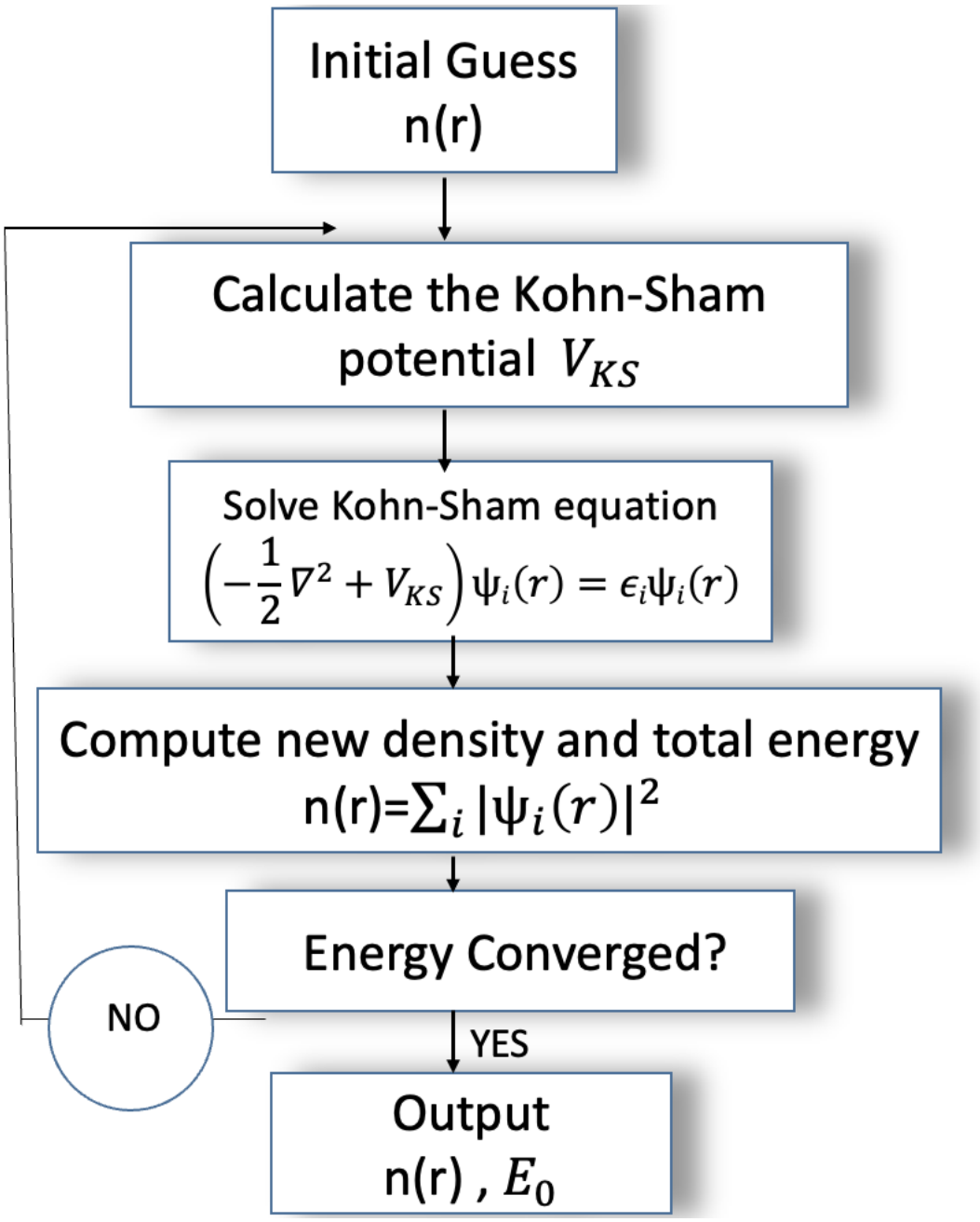

Figure. 2.1: the cycle self-consistent of Kohn-Sham equation

2.2.3 Approximation of Exchange-correlation

The local density approximation (LDA), generalized gradient approximation (GGA), and hybrid functional are popular approximations of exchange-correlation $E_{XC}[n(r)]$.

2.2.3.1 Local Density Approximation (LDA)

The local-density approximation (LDA) to the exchange-correlation energy functional $E_{XC}[n(r)]$ [82][83] relies simply on the magnitude of electron density at each place in the space**.**

$$E_{xc}^{LDA}[n] = \int dr\, n(r)\epsilon_{xc}(n(r)). \qquad (2.2.22)$$

Where $\frac{\delta E_{Xc}^{LDA}[n(r)]}{\delta\, n(r)} = V_{Xc}^{LDA}$

V_{Xc}^{LDA} the exchange-correlation potential for LDA approximation and the exchange-correlation energy per particle of a homogenous electron gas with density $n(r)$ is ϵ_{xc}.

2.2.3.2 Generalized Gradient Approximation (GGA):

For the exchange-correlation energy, generalized gradient approximations (GGA) usually outperform the local-density approximation (LDA) description of atoms, molecules, and solids[84].

$$E_{xc}^{GGA}[n] = \int dr\, n(r)\, f\big(n(r), \nabla n(r)\big). \qquad (2.2.23)$$

Equation (2.2.23) represents the generalized gradient approximations (GGA). The exchange-correlation energy functional is affected by both the magnitude and gradient of the electronic density.

2.2.3.3 Hybrid Functional Approximation:

Hybrid functional are a family of density functional theory (DFT) approximations to the exchange-correlation energy functional that combine a piece of exact exchange from Hartree-Fock theory with the rest of exchange-correlation energy from density functional theory (DFT)

An example of a hybrid functional is B3LYP; Becke, 3parametters, Lee-Yang–Parr[85][86]. The following equation represents the hybrid functional of B3LYP functional.

$$E_{XC}^{B3LYP} = a\ E_X^{HF} + (1-a)E_X^{LDA} + b\Delta E_X^B + \mathrm{c}\ E_C^{LDA} + (1-\mathrm{c})E_C^{LYP} \qquad (2.2.24)$$

In equation (2.2.24), the subscript X and C represent exchange and correlation terms, respectively. Here E_X^{HF} is the Hartree-Fock exchange. Becke used his exchange function to add LDA correlation (E_C^{LDA}) and LYP correction to the local density approximation (E_C^{LYP}). Also, Becke optimized three parameters, a, b, and c are constant values.

2.3. Ab Initial Molecular Dynamic (AIMD) Simulation:

Molecular dynamics calculations performed in this dissertation to study Temperature effects. In molecular dynamics, dynamical evolution of atoms is studied in the framework of statistical mechanical ensemble theories. For the dynamical evolutions, forces between the atoms needed to be calculated. In ab initio molecular dynamics theory (AIMD), these forces are calculated from the electronic structures of the system of interest by self-consistent first-principles theories, such as via DFT. With the calculated force, the atoms evolve in time by mean of Newtonian dynamics. In AIMD, electronic structures are integrated to directly solve the static quantum mechanical properties in each molecular dynamic steps based on a set of the fixed nuclear location at the point in time. [87].

The interface of Ab initio molecular dynamics (AIMD) represented

$$M\ddot{R} = F_I \quad (2.3.25)$$

$$M\ddot{R} = -\nabla_I V(R_I(t)) \quad (2.3.26)$$

Here $\ddot{R}$ is the acceleration. As a result of the forces calculated from the electronic structures, the Hellmann-Feynman force, the nuclei move in an effective potential according to classical mechanics. This potential V is a function of just the nuclear position at time t due to averaging $<\Psi|H_{ele}|\Psi>$ across the electronic degree of freedom.

$$M\ddot{R} = -\nabla_I \min <\Psi|H_{ele}|\Psi> \quad (2.3.27)$$

$$E\,\Psi = \Psi\, H_{ele} \quad (2.3.28)$$

The electronic ground state is a result of the Born-Oppenheimer Molecular Dynamic method (BOMD) method.

- **Verlet Method:**

The Verlet approach is a numerical method for solving Newton's equations of motion. It is often used in molecular dynamics simulation to compute particles trajectories. First, we consider the initial position $r_i(t_0)$ and velocity $v_i(t_0)$ of the nuclei. Then we can calculate the potential of the system by DFT to calculate the force using equation (2.3.26).

Newton's Second Law of motion

$$F = ma = m\frac{\partial v}{\partial T} = m\frac{\partial^2 r}{\partial t^2} \quad (2.3.29)$$

Where the position and velocity after integration will be

$$r = r_0 + v\,t \tag{2.3.30}$$

$$v = v_0 + a\,t \tag{2.3.31}$$

Now at time step Δt, we can solve the equation of motion by a Taylor series expansion:

$$r = r(t+\Delta t) = r(t) + v(t)\,\Delta t + \frac{1}{2}\,a\,\Delta t^2 \tag{2.3.32}$$

$$v = v(t+\Delta t) = v(t) + a\,(t)\,\Delta t \tag{2.3.33}$$

So, the Verlet Method derive can be written

$$r = r(t+\Delta t) = r(t) + v(t)\,\Delta t + \frac{1}{2}\,a\,\Delta t^2$$

$$r = r(t-\Delta t) = r(t) + v(t)\,\Delta t + \frac{1}{2}\,a\,\Delta t^2$$

Adding these two equations to get

$$r(t+\Delta t) + r(t-\Delta t) = 2r(t) + a\,\Delta t^2 \tag{2.3.34}$$

Or

$$r(t+\Delta t) = 2r(t) - r(t-\Delta t) + a\Delta t^2 \tag{2.3.35}$$

The Verlet method calculates the new position by using position and acceleration at time $t+\Delta t$ and position from $t-\Delta t$. To solve the molecular dynamic simulation of a system of particles evolves in time is shown in the following flow-chart.

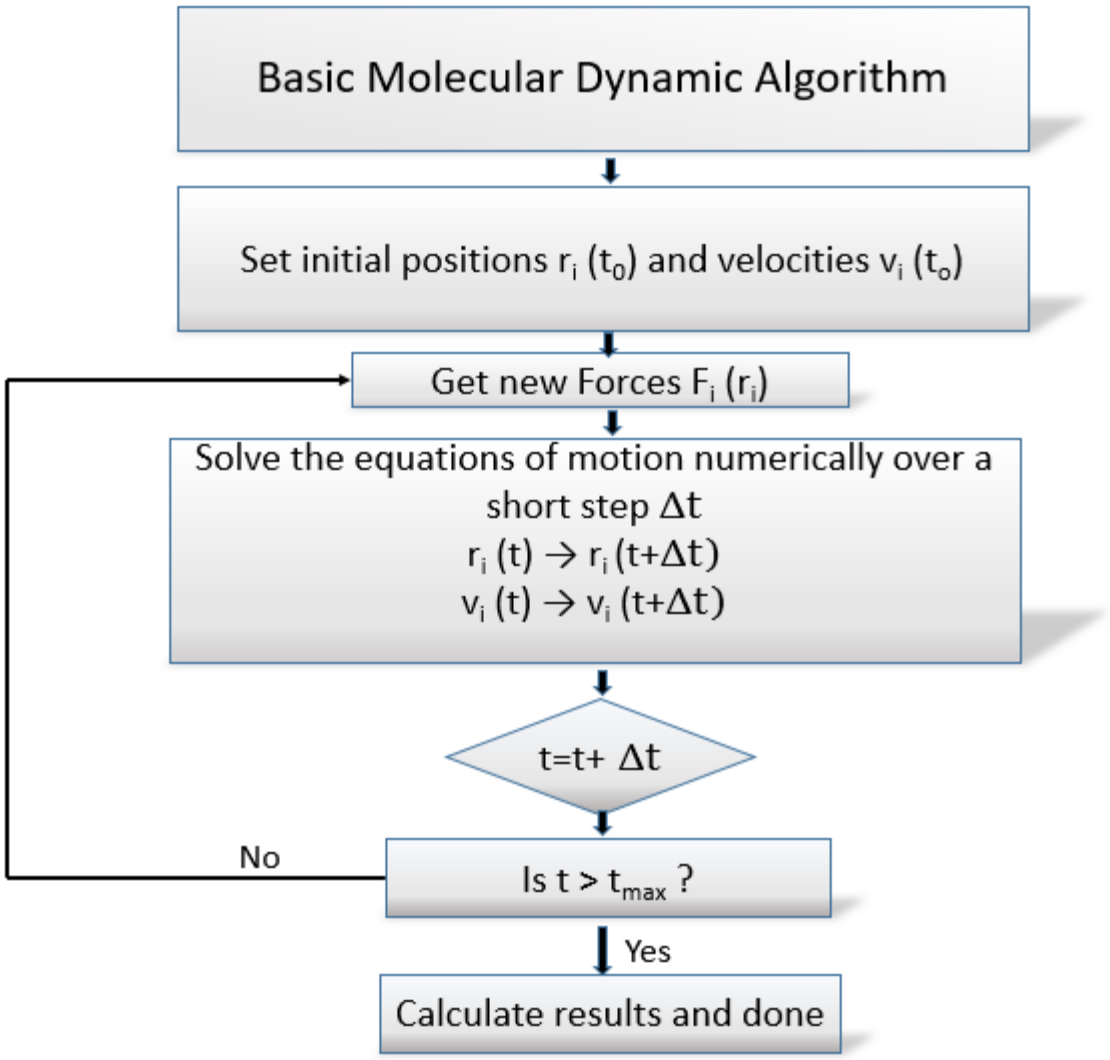

Figure 3.2.1: the cycle molecular dynamic

Chapter 3

3.1. Pristine Fullerene

In this chapter, we are going to investigate the electronic properties of C_{60}, C_{70}, $Si_{60,}$ $Si_{30}C_{30}$, and $Si_{35}C_{35}$ fullerenes. First, we will show the methods that we use in our investigation. Then, show the results in detail.

3.1.1. Computational Methods:

The DFT [88], with B3LYP hybrid functional [89] as applied in the Gaussian 09 set of codes and atomic wave functions LAN2DZ base set [77] (Los Alamos National Laboratory 2 Double-Zeta) [90] is used to analyze the C_{60}, and $Si_{30}C_{30}$ fullerenes. Also, their endohedrals doping of transition metal atoms (W, Fe, Ta, Hf, and Nb).

The binding energy (E_b) in uniting (eV/atom), the highest occupied molecular orbital (HOMO) - the lowest occupied molecular orbital (LUMO) in a unit of (eV) and other structural characteristics were measured. For example, the binding energy value can be measured by following these equations.

$$E_b(\mathrm{X}_n) = \frac{E(\mathrm{X}_n) - nE(\mathrm{X})}{n} \qquad (3.1.1)$$

Equations (1) calculate the binding energy of C_{60} and Si_{60} fullerenes. Also, $E(\mathrm{X}_n)$ are total energies of f C_{60}, $C_{70,}$ or Si_{60} fullerenes; where X= C or Si and n=60 or 70 atoms. E(X) is the C or Si atomic energies.

For the binding energy of $Si_{30}C_{30}$ or $Si_{35}C_{35}$ fullerenes, we used the following equations,

$$E_b(\mathrm{Si}_n\mathrm{C}_b) = \frac{E(\mathrm{Si}_n\mathrm{C}_b) - nE(\mathrm{Si}) - bE(\mathrm{C})}{n+b} \quad (3.1.2)$$

In equation (3.1.2), the$E(\mathrm{Si}_n\mathrm{C}_b)$, are the total energies of relaxed fullerenes a. $E(\mathrm{Si}), and\ E(\mathrm{C})$ are the atomic energies for silicon, carbon. Where, n+b= 60 or 70 atoms.

3.1.2. C_{60} Fullerene:

The carbon atoms on C_{60} fullerene are all bonded with either single or double covalent bonds. Also, the C_{60} fullerene is a symmetrical sphere. As a result, if atoms are put in the center of the C_{60} fullerene, the doped atoms do not interact much with the cage wall. To start the calculation, we have considered the value for binding energy eV/atom and HOMO-LUMO gap eV of C_{60} fullerene. The binding energy and HOMO-LUMO gap values are -6.60 eV/C-atom and 2.878 eV, respectively. In the corresponding experimental values, which are 7.4 eV/atom and above 2.5 eV, respectively[91] [92]. Also, we have to consider the value of diameter, double, and single bonds for C_{60} fullerene. The calculation value are 7.149 Å, 1.394 Å, and 1.458 Å, respectively, and in the corresponding experimental values, which are 7 Å and 1.39 Å for single bond and 1.45 Å double bond[93][47][94].

Table: 3.1.1: shows the binding energy (E_b) (eV/atom), HOMO-LUMO gaps (eV), bonds lengths (Å), and diameters (Å) of relaxes structure of C_{60}, and C_{70} fullerene. Multiplicity (Mu).

Type of fullerenes	E_b (eV/atom)	HOMO-LUMO gaps (eV)	Smallest double bonds(Å)	Average double bonds(Å)	Smallest double bonds(Å)	Average double bonds(Å)	Diameter (Å)	multiplicity	Exp-diameter (Å)
C_{60}	-6.60	2.878	1.394	1.394	1.458	1.458	7.149	Singlet	7.0 [8]
C_{70}	-6.637	2.683	1.397	1.421	1.458	1.458	7.132(z-axis) 8.335(x-axis)	Singlet	7.906 [56][57]

3.1.3. C_{70} Fullerene

The second most common fullerene, C_{70} fullerene, and its derivatives have increased interest in a variety of areas, ranging from medicines to materials research. This is because of the binding energy per atom of C_{70} fullerene[57], which is bigger than C_{60}. In addition, carbon fullerene possesses a strong covalent is one of its most interesting characteristics. As a result, fullerene's carbon is saturated, and the cage surface has no unpaired electrons.

We start our study with C_{70} fullerene. This structure shows a low binding energy value of -6.637 eV/atom, as shown in Table 3.1.1. Also, for electron properties, The C_{70} fullerene shows a significant value of the highest occupied molecular orbital (HOMO)- the lowest occupied molecular orbital (LUMO) by 2.683 eV. Furthermore, due to the C_{70} fullerene shape, single, and double bonds are not the same in whole stricture, where the smallest single bond (Bs) and a double bond (Bd) are 1.458 Å and 1.397 Å. In addition, the diameters are 7.132 for the z-axis and 8.335 for the x-axis.

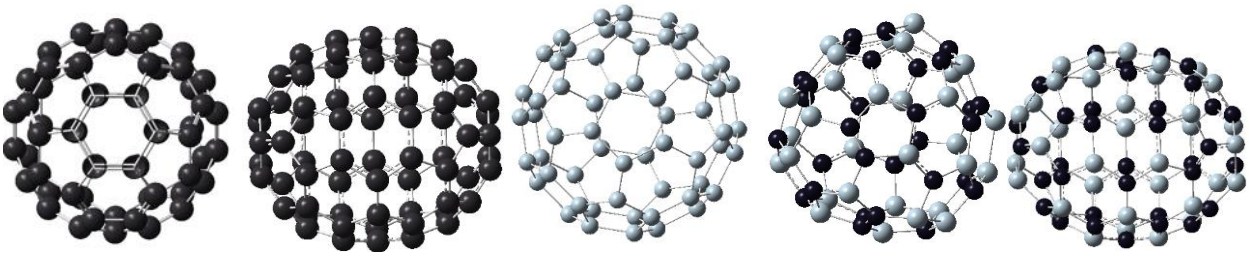

(a) C_{60} (b) C_{70} (c) Si_{60} (d) $Si_{30}C_{30}$ (e) $Si_{35}C_{35}$

Figure 3.1.1: showed the relaxed structures of C_{60}, C_{70}, $Si_{60,}$ $Si_{30}C_{30}$, and $Si_{35}C_{35}$ fullerenes.

3.1.3. Si_{60} Fullerene

Figure 3.1.1 shows relaxed Si_{60} structure with this symmetry. This is the only structure in this study which was relaxed with symmetry constraint. As a result, the final structure remained a fullerene structure; whereas it has been reported that, a fully relaxed structure of Si_{60} structure is usually a distorted one [22], [95], [96]. The average bond length of Si_{60} in figure 3.1.1 is 2.03 Å where also the diameter is 11.40 Å. The purpose of symmetry constraint relaxation was that the relaxed fullerene Si_{60} was used as a template to construct the $Si_{30}C_{30}$ structures studied in this paper.

3.1.4 SiC Fullerenes.

3.1.4. A $Si_{30}C_{30}$ Fullerenes.

The results and discussion for the $Si_{30}C_{30}$ structure are based on unsegregated fullerene. This structure has the maximum number of Si-C bonds among all the $Si_{30}C_{30}$ structures we considered in our previous study[32]. The numbers of Si-C bonds are 78, and the number of Si-Si and C-C bonds are six bonds for each. Because it retains almost a spherical cage structure, it is called a sphere structure, as shown in figure 3.1.1. The average diameter of 8.94 Å and average Si-Si and C-C bonds by 2.26Å and 2.25Å, and it stabilized with a spin-multiplicity in a singlet state. The calculated binding energy is 6.002 eV/atom. Moreover, the sphere structure is found to be the ground state structure at global minima with no negative frequency.

Table: 3.1.2: shows the binding energy (E_b) (eV/atom), HOMO-LUMO gaps (eV), average bonds lengths Å, and diameters Å of relaxes structure of Si_{60}, $Si_{30}C_{30}$, and $Si_{35}C_{35}$ fullerene and multiplicity (Mu).

	E_b (eV/atom)	HOMO-LUMO gaps (eV)	Average C-C Bonds Å	Average Si-Si Bonds Å	Average Si-C Bonds Å	Average Diameter Å	Mu
Si_{60}	-3.999	1.421	----	2.033	-------	11.40	singlet
$Si_{30}C_{30}$	-4.712	1.524	1.40	2.26	1.750	8.94	singlet
$Si_{35}C_{35}$	-4.708	1.874	1.416	2.318	1.845	10.812 (x-axis) 9.134 (z-axis)	singlet

3.1.4.B $Si_{35}C_{35}$ fullerenes.

The fullerene-C70 s is a wide class of fullerene derivatives[97][35]. So, by replacing 35 C-atoms with 35 Si-atoms, $Si_{35}C_{35}$ segregated fullerene is made with a maximum number of Si-C bonds, 92 bonds. Also, minimum Si-Si and C-C bonds, 7 bonds. Where also, endohedral doping of $Si_{35}C_{35}$ fullerene is a class of fullerene derivatives.

Our result shows that how the strong Si-C bond is. The more Si-C bonds in the structure, the ellipsoid shape we will get, as shown in figure3.1.1. The $Si_{35}C_{35}$ fullerene has a larger inner space with 10.812 Å on x-axis and 9.134 Å on z-axis. Where $Si_{35}C_{35}$ fullerene has -4.708 eV/atom which is higher 0.004 eV/atom than $Si_{30}C_{30}$ fullerene. On the other hand, it has higher HOMO-LUMO gap as same as Si-Si bond length of 1.874eV and 2.318Å compared to Si_{60} and $Si_{35}C_{35}$ fullerene.

3.1.4.C $Si_{30}C_{30}$ Fullerenes Isomers and their Hydrogen Passivation:

1. Structures Analysis

As mentioned in the introduction, earlier silicon-carbide clusters based on Si_{60} fullerene structure resulted in highly distorted structures. Among those, some SiC structures-maintained cage like features. For the present study, to build $Si_{30}C_{30}$, the first step was to take the symmetry-restricted relaxed Si_{60}-fullerene, and then thirty carbon atoms at different possible symmetry configurations have replaced the Si atoms. Due to differences in electronic properties of Si-Si and C-C bonds, SiC fullerene-like structures do not have high symmetry [98][99]. The relaxed Si_{30}-C_{30} configurations, those have been investigated in this study are shown in Figure 3.1.2. Note, all these $Si_{30}C_{30}$ structures, though started from an ideal Si_{60} fullerene structure, relaxed completely without any symmetry constraint. Table 3.1.4 shows the binding energies, HOMO-LUMO gaps, and bond-lengths for these $Si_{30}C_{30}$ structures.

As the initial geometry was a fullerene structure, some of the Si atoms will have unsaturated dangling bonds, where Si atoms are supposed to make π-bonds and the bond lengths are too large to Si-p orbital's side-wise overlap. To passivate these unsaturated bonds in the $Si_{30}C_{30}$ structures hydrogen atoms were added to each Si atom in the unrelaxed $Si_{30}C_{30}$ fullerenes initially, and then optimized completely ($Si_{30}C_{30}H_{30}$); the initial set of structures were the same as were in the figure 3.1.2, but here with passivating H atoms. The relaxed set of passivated structures is shown in figure 3.1.3. After relaxation, in some structures, few Si atoms lost passivating H-atoms, and these H-atoms then re-boned with nearby C atoms. Hence, these H atoms also act as an indicator to investigate the local bonding coordination and configurations. Binding energies, the HOMO-LUMO gaps and bond lengths for $Si_{30}C_{30}H_{30}$ are given in Table 3.1.4.

In the following, to facilitate further discussion, names will be assigned to each of the structures in figure 3.1.2. As the initial structures in figure 3.1.3 were the same as in figure 3.1.2, but with added H-passivation, so the names in figure 3.1.3 has an H-prefix with them. The

structures in figures 3.1.2 and 3.1.3 are arranged in the order of their stability. In the remaining of the paper, these names will be referred to when discussing these structures.

The first one in Figure 3.1.2(a) is **C_{30}-bowl** structure: the left side of this structure is 30 carbon atoms make a bowl-like configuration, and 30 Si atoms are on the right of it. The initial Si_{60} fullerene was segregated with 30 C and 30 Si atoms with a boundary in the middle, and then relaxed completely without any symmetry constraints. The 30 C atoms relaxed into almost like a half of C_{60} fullerene sphere. The **C_{30}-bowl** structure has Si-C bonds only at the two regions' boundary. There are 10 Si-C bonds with an average of 1.88 Å.

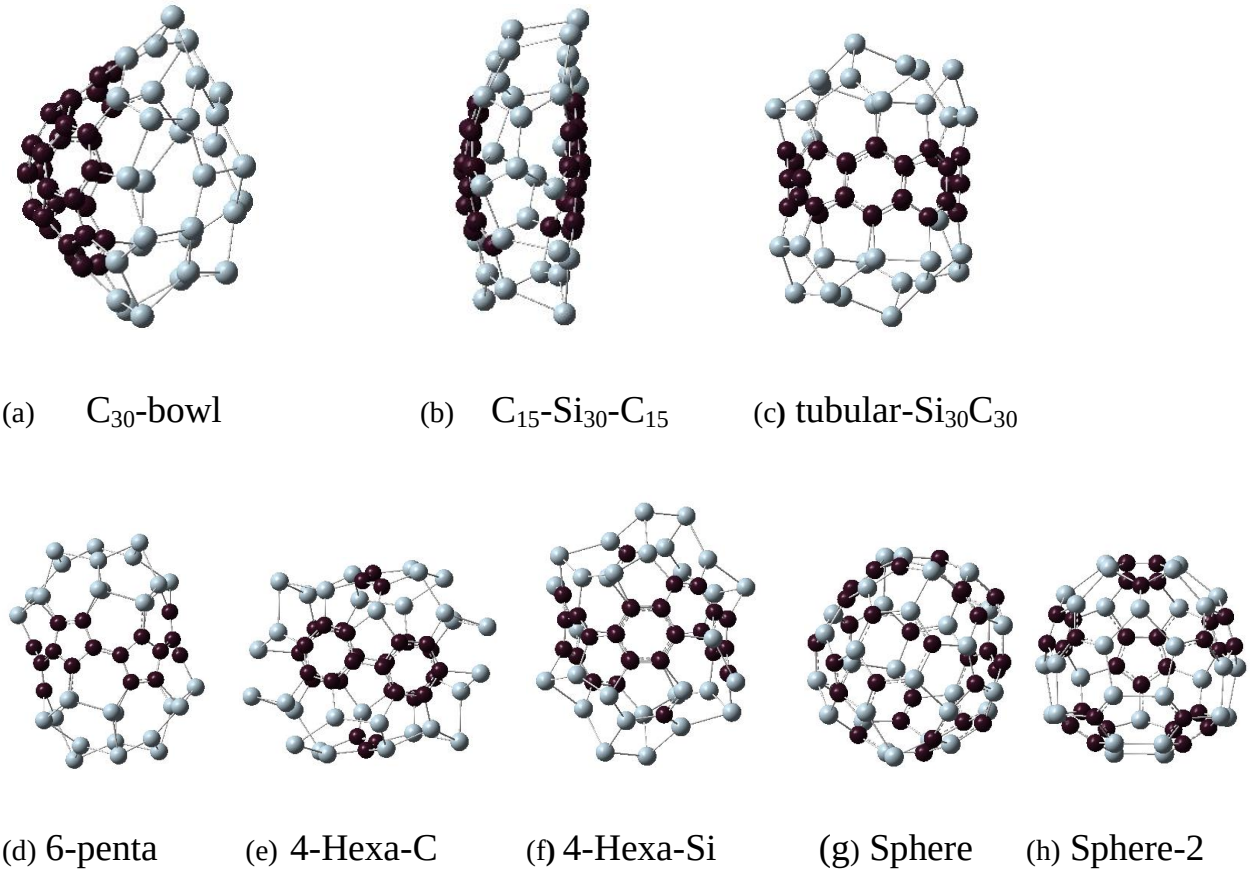

Figure. 3.1.2. Different isomers of $Si_{30}C_{30}$ structures configured from figure 1 and then relaxed complexly without any symmetry constraint. The names of these structures are explained in the text. Structures are presented from (a) to (h) in order of their stability.

In Figure 3.1.2 (b) another Si_{60} derived structures, **C_{15}-Si_{30}-C_{15}**, where 15 C atoms make caps in the left and right ends of the fullerene cage and the thirty silicon atoms are in the middle. In figure 3.1.2(c), the similar model was constructed, but in this time the 15 silicon atoms are located in the right and left end, and the thirty atoms of carbons are in the middle of fullerene, Si_{15}-C_{30}-Si_{15}. However, because of the shape of the relaxed structure, we name it as a **tubular-$Si_{30}C_{30}$** structure. Both of these structures have 18 Si-C bonds with the same average bond lengths

of 1.86 Å.

The next structure in figure 3.1.2 (d), is named as **6-penta**, where six pentagons in Si_{60} were substituted by C atoms, and the rest were Si atoms. In this structure, there are Si and C pentagons, and the others are Si-C hexagons. There are 18 Si-C bonds with the average bond length of 1.84 Å.

In figure 3.1.2 (e), the structure named **4-Hexa-C**, where we select the four hexagon faces replaced by carbon atoms in the diagonally opposite sides of the Si_{60} fullerene sphere (front and back in the viewing direction), and three carbon atoms in the top and bottom in the pentagon faces of the fullerene. In figure 3.1.2 (f), a complimentary structure of figure 2(e) was constructed where the position of Si and C were swapped. We call it 4-Hexa-Si. The final relaxed structures of these two configurations are significantly different, as seen in the figures 3.1.2(e) and (f). However, the total Si-C bonds in these two structures are same, 30, with the average bond lengths of 1.89 Å

Table 3.1.3. The following table shows the binding energies (E_b), HOMO-LUMO gaps, and the average bond length of Si-C, C-C, and Si-Si bonds of $Si_{30}C_{30}$ structures.

Type of structure	E_b (eV/atom)	HOMO-LUMO gap (eV)	Shortest Si-C bond length (Å)	Shortest Si-Si bond length (Å)	C-C bond length (Å)	Si-C bond length (Å)	Si-Si bond length (Å)
C_{30}-bowl	-6.214	1.286	1.81	2.29	1.39	1.88	2.43
C_{15}-Si_{30}-C_{15}	-6.174	1.171	1.83	2.30	1.43	1.86	2.39
tubular-$Si_{30}C_{30}$	-6.124	1.358	1.80	2.28	1.44	1.86	2.38
6-penta	-6.088	1.160	1.80	2.30	1.37	1.84	2.35
4-Hexa-C	-6.070	0.998	1.83	2.02	1.43	1.89	2.39
4-Hexa-Si	-6.056	1.503	1.80	2.01	1.59	1.89	2.27
sphere	-6.013	1.604	1.81	2.02	1.61	1.88	2.33
Sphere2	-5.975	0.972	1.80	2.27	1.42	1.86	2.38
C-bowl	-7.669	1.118			1.34	0	0
Si-bowl	-3.722	1.139		2.26	0	0	2.39

In figures 3.1.2(g) and (h), we model the structures to minimize the number of C-C and Si-Si bonds to maximize the number of Si-C bonds. In the structure, as shown in figure 3.1.2(g), Si and C atoms were placed alternatively, as much as possible, however, there remained some Si-Si and C-C bonds in the structure. The relaxed structure was somewhat a spherical one; therefore, we named it as **sphere**. The total number of Si-C bonds are 56 for this structure with average bond length of 1.88 Å. The last structure we tried in this group is in figure 3.1.2(h), where the structure starts with a pentagon face by silicon atoms (the frontal pentagon). The next neighbor atoms were replaced by carbon atoms and after that, the next neighbors were kept silicon atoms, and went on alternating till the structure ends with the pentagon face of carbon atoms (the back pentagon). So, in this structure two diagonally opposite pentagons are made of Si and C atom, respectively. This structure also preserves its spherical nature, and we named it **sphere-2**. The total number of Si-C

bonds in this structure is 60, the highest in all the $Si_{30}C_{30}$ configurations studied in this paper. The average Si-C bond lengths here is 1.86 Å.

The hydrogen passivated structures are presented in figure 3.1.3. They were constructed the same way as described above, with added hydrogen on Si atoms; hence these passivated $Si_{30}C_{30}H_{30}$ structures are named with an H-prefix.

2. Electronic Properties

The relaxed **C_{30}-bowl** structure in figure 3.1.2(a) shows the distortion in the Si_{30} side, as expected. The reason is the tendency for Si atoms to form sp^3 bonds with each other, as compared to the favorability of sp^2 C-C bonds. On the C-side, the C_{30} bowl is almost a part of the C_{60} fullerene, except at the boundary where Si-C bonds formed. The average bond length of C -C is 1.39 Å and the average Si-C bond length is 1.88 Å, presented in Table 3.1.3. In addition, the experimental value of S=C double bond length reported to be 1.77 Å [100] which is close to shortest S-C bond length 1.81 Å in this structure presented in Table 3.1.3The binding energy of this structure was -6.214 eV/atom, which is the most stable one in the group of structures studied in this paper. Also, this structure is more stable than previously studied similar Si and C segregated $Si_{40}C_{20}$ and $Si_{36}C_{24}$ fullerene-derived structures with a binding energies of -4.748 eV/atom and -4.977 eV/atom, respectively [25]. A trend that emerges from these three segregated silicon-carbide structures is that, as C atoms are increasing in the carbon side, the clusters' stabilities become higher. All these three structures have dipole moments of about 1.4 Debye. So, the orbital charge distribution is not spherical, which is obvious from their non-zero dipole moment.

Table 3.1.4. The following table shows the binding energies (E_b), the HOMO-LUMO gaps, and the shortest Si-Si, Si-C bond length of passivated structures $Si_{30}C_{30}H_{30}$ structures.

Type of passivated structure (Si_{30}-$C_{30}H_{30}$)	E_b (eV/atom)	HOMO-LUMO gap (eV)	Shortest Si-C bond length (Å)	Shortest Si-Si bond length (Å)	C-C bond length (Å)	Si-C bond length (Å)	Si-Si bond length (Å)
H-4-Hexa-C	-6.439	0.375	1.86	2.37	1.42	1.92	2.41
H-C_{30}-bowl	-6.249	1.108	1.92	2.36	1.43	1.94	2.43
H-tubular-$Si_{30}C_{30}$	-5.880	1.328	1.85	2.29	1.45	1.82	2.42
H-C_{15}-Si_{30}-C_{15}	-5.795	1.537	1.84	2.30	1.42	1.96	2.39
H-6-penta	-5.632	0.699	1.84	2.30	1.21	1.90	2.42
H-Sphere2	-5.631	1.343	1.82	2.24	1.38	1.86	2.40
H-Sphere	-5.517	0.567	1.74	2.27	1.48	1.88	2.36
H-4-Hexa-Si	-5.483	1.668	1.91	2.28	1.34	1.94	2.55

Fig. 3.1.2(b) shows the relaxed **C_{15}-Si_{30}-C_{15}** structure where two groups of 15 carbon atoms are placed on the right and left side of the fullerene. These two C_{15}-caps consist of two hexagons and two pentagons, and they almost became flat upon relaxation, not like C_{15} bowls. As a result, the 30 Si atoms are spread out almost in a bi-layer structure with two C_{15} caps in the middle, with a bi-layer separation distance of 4.55 Å in the middle for C-C distance, and around the edge the shortest Si-Si distance was 2.38 Å. The shortest Si-C bond length is 1.83 Å, also, the average of C-C bond length in a layer is 1.43 Å. This structure is the second stable fullerene structures with E_b of -6.174 eV/atom, and HOMO-LUMO gaps 1.171 eV.

Due to the strong C-C bond and weak Si-Si bond in **tubular-$Si_{30}C_{30}$**, the 30 carbon atoms tightened the fullerene around the middle and silicon atoms that located on the caps extended a little bit without breaking the Si-Si bond, and the structure looks like a closed tube. The E_b is -6.124 eV/atom with -0.050 eV higher than ($C_{15}Si_{30}C_{15}$). However, the Si and C atoms distribution

is more symmetric than the previous structures, as is evident by the lower dipole moment; a reduction of about 50%.

The relaxed **6-penta** is shown in figure 3.1.2(d), and it has a binding energy of -6.088 eV/atom with an average C-C bond length of 1.37 Å, lowest among all $Si_{30}C_{30}$ structures in considered Table 3.1.3, whereas the average Si-C bond length was also lower, 1.84 Å. This structure has a similarity with the previous structure of Figure 3.1.2(c) tubular-$Si_{30}C_{30}$, the main difference being 6-penta has 30 C atoms as pentagons around the middle. Though lower in stability, 6-penta is higher in symmetry with a very low dipole moment 0.13 Debye.

4-Hexa-C structure shows the distorted open structure because some Si-Si bonds broke during relaxing the structure (figure 3.1.2(e)). The binding energy is 0.144 eV/atom higher that the most stable structure in Table 3.1.3 and has smaller value of HOMO-LUMO gap of 0.998 eV. Its complementary structure, the **4-Hexa-Si** structure shown in figure 3.1.2(f), where Si atoms were switched with C atoms in 4-Hexa-C. The **4-Hexa-Si** has a higher binding energy of -6.056 eV/atom; however, the binding energy difference between these two structures is only 0.014 eV/atom. It also has a higher HOMO-LUMO gap of 1.503 eV. Also, it does not show distorted open structure as was found in 4-Hexa-C structure with a smaller average Si-Si bond-lengths of 2.27 Å, 0.12 Å lower than that of 4-Hexa-C. The average Si-C bond lengths for these two structures are same, 1.89 Å; it is the largest Si-C bond length of all relaxed structures in Table 3.1.3. These two structures have zero dipole moments, implying that the effective negative and positive charge centers coincide at the center of these two cages. This also signify an overall "spherical" nature of orbital charge distributions for these two structures.

The structure named **sphere** in figure 3.1.2(g), has E_b increased by 0.201 eV/atom compared to that of the most stable C_{30}-bowl with the largest HOMO-LOMO gaps value of 1.604

eV. The last structure is shown in Fig. 3.1.2(h), **sphere-2.** However, it has the highest E_b -5.975 eV/atom and the lowest HOMO-LUMO gap 0.972 eV, as presented in Table 3.1.3. These last two almost spherical $Si_{30}C_{30}$ structure have binding energy difference of 0.038 eV/atom. After relaxing these two configurations we found that, even though the spherical geometric nature of the fullerene was not significantly distorted like the other configurations in this study, the orbital charge distributions were significantly distorted. The dipole moments were 2.15 and 3.20 Debye, respectively for sphere and sphere-2.

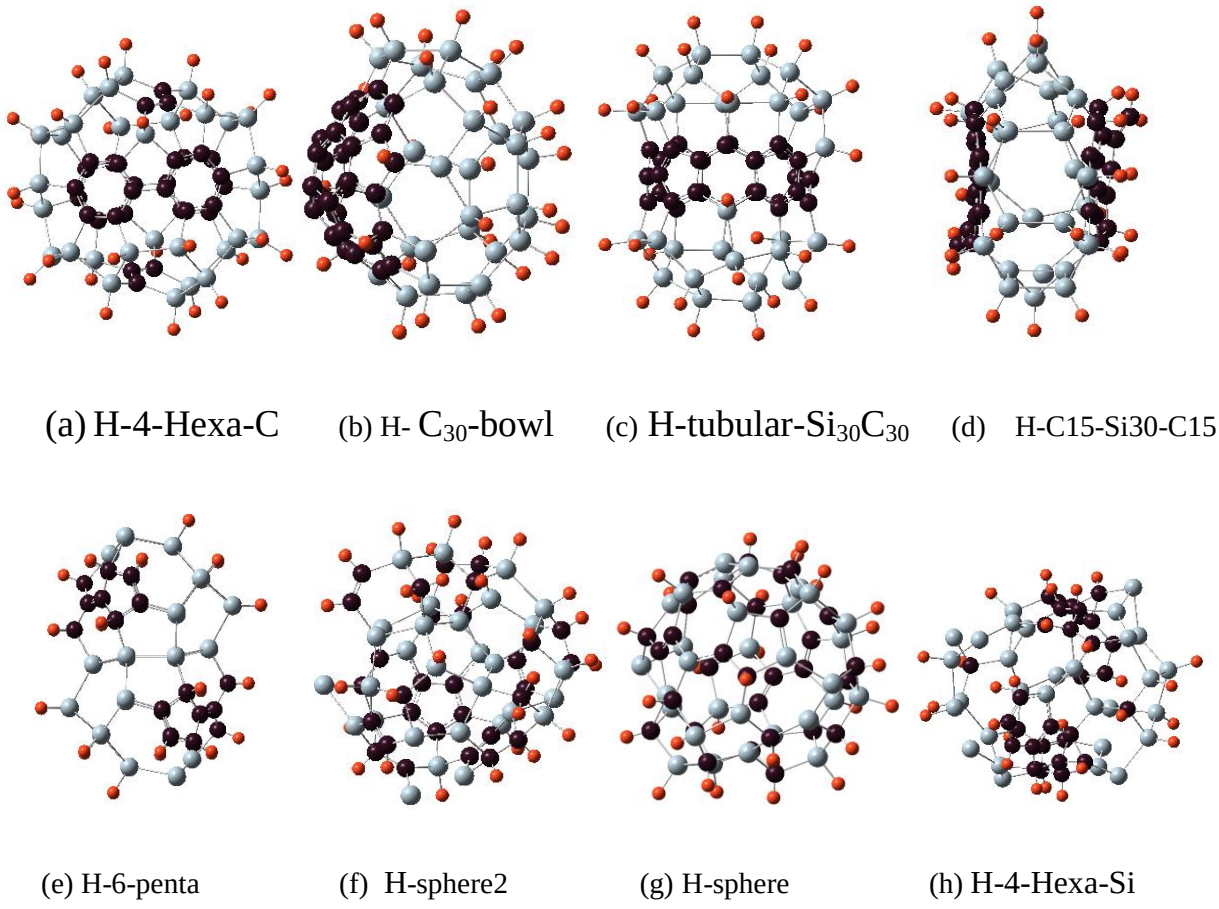

(a) H-4-Hexa-C (b) H- C_{30}-bowl (c) H-tubular-$Si_{30}C_{30}$ (d) H-C15-Si30-C15

(e) H-6-penta (f) H-sphere2 (g) H-sphere (h) H-4-Hexa-Si

Figure 3.1.3. Different isomers of $Si_{30}C_{30}$ structures with hydrogen passivation, $Si_{30}C_{30}H_{30}$, where hydrogen atoms bonded with the three-fold coordinated Si atoms on Si_{60} surface. The $Si_{30}C_{30}$ configurations and the naming conventions are the same as in the figure 2; for hydrogen passivation, each cluster name has an H prefix. Structures are presented from (a) to (h) in order of their stability.

All the structures discussed above have no higher spin state; that is, they have spin multiplicity 1. The range of binding energy within the scope of this study is (-6.089 ± 0.080) eV/atom, which implies that the fullerene derived $Si_{30}C_{30}$ structures overall are very stable. The Si-C bond lengths remained consistent across the structures, with an average value of (1.868 ± 0.017) Å. In addition, the binding energy trend follows the increasing order of the number of C-C bond in the structures. Figure 3.1.4 represents such a plot, which shows that the stability of the structures increases as the number of C-C bond increases in the $Si_{30}C_{30}$ structures. Except for the two least stable structures on the top left corner of the plot, all the structures follow the trend.

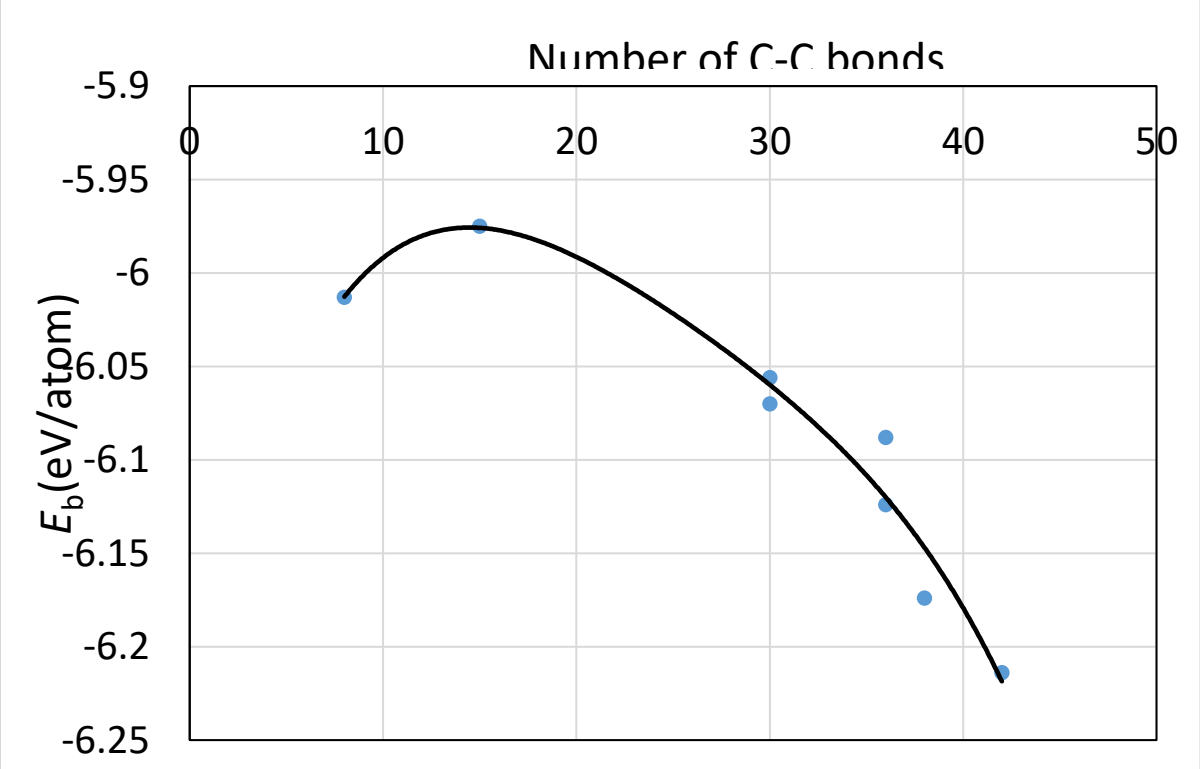

Figure 3.1.4: The trend of binding energy of unpassivated structures with respect the C-C bonds in the structures from figure 2. The solid line is a polynomial fit of the calculated binding energies represented by the solid circular dots. Except for the two least stable structures on the top left corner of the plot, all the structures follow the trend that the stability of a structure increases as the number of C-C increases in a structure.

For comparison purposes, we have also investigated C_{30} and Si_{30} "half-fullerene" as two bowl-structures separately as shown in figures 3.1.5(a) and (b), respectively. The binding energy for C_{30} is -7.669 eV/atom and has a HOMO-LUMO gap of 1.117 eV, as listed in Table 3.1.3. The Si_{30} structure is relatively less stable with the higher binding energy of -3.722 eV/atom, with a slightly higher HOMO-LUMO gap of 1.139 eV, also listed in Table 3.1.3. Then, we put these two Si_{30} and C_{30} half-fullerene at 5 Å apart, as shown in figure 3.1.6, named as **Si_{30}-C_{30}-Bowl**. After full relaxation, these two "half-fullerenes" came together and made the bond between Si and C atoms, with a distorted relaxed configuration. This configuration, **Si_{30}-C_{30}-Bowl**, has a binding energy of -6.130 eV/atom and HOMO-LUMO gap 1.046 eV. The main difference between this structure and the C_{30}-bowl structure of figure 3.1.2(a) is the input structure: before relaxation, the input structure for C_{30}-bowl was constructed from Si_{60} fullerene. If we compare the stability between these two structures, the C_{30}-bowl has -0.084 eV/atom more stable than Si_{30}-C_{30}-Bowl**.** Also, in Si_{30}-C_{30}-Bowl, the carbon part of the structure is more distorted than the C_{30}-bowl. The two approaches for obtaining a similar $Si_{30}C_{30}$ structure shows that (i) even the stronger part of the structure, here the C_{30} part, can be susceptible to distortions due to different initial conditions, (ii) initial condition also determines the final stability of the clusters. Hence, in selecting the precursors while synthesizing these clusters, initial conditions need to be determined by considering these facts.

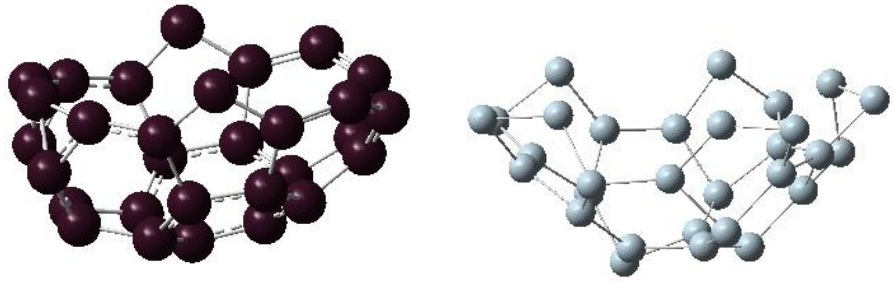

(a) (b)

Figure 3.1.5. Relaxed structures of (a) C_{30} fullerene as bowl and (b) Si_{30} fullerene as bowl.

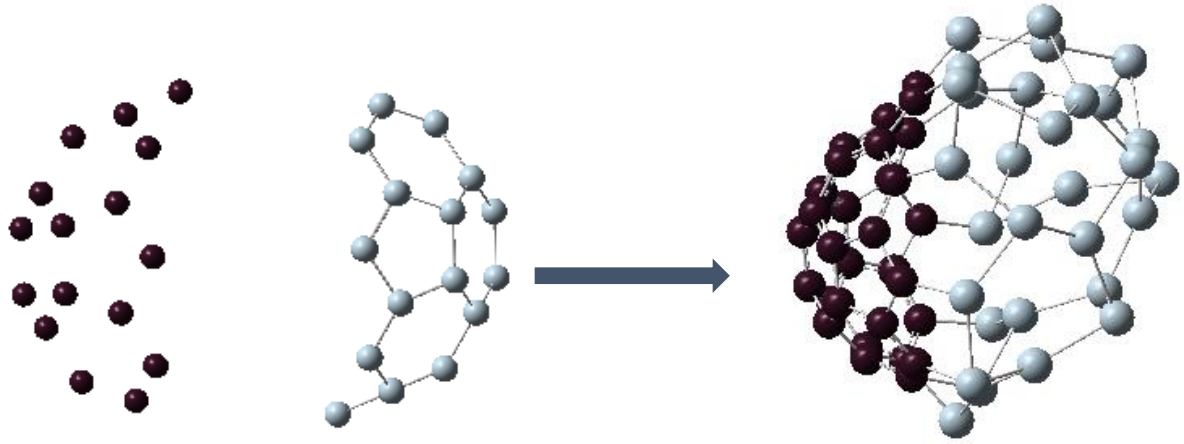

(a) (b)

Figure 3.1.6. (a) Initial configuration of fullerene with left bowl of carbon (C_{30}) and right bowl of silicon (Si_{30}) with 5Å distance between them. (b) The structure after geometry relaxation. This configuration is similar to figure 3.1.1(a), however, the carbon side looks more distorted due to the different initial condition.

3. The Hydrogen Passivated Fullerene

Under passivation, the fullerenes structures relaxed differently compared to their unpassivated counterparts. We note here again that the initial structures were the same as for the unpassivated ones, as presented in figure 3.1.2; the difference is that for the passivated initial fullerene configuration, each Si atom bonded with an additional hydrogen atom. Upon relaxation,

some of the passivated structures have shown interesting behaviors; such as some hydrogen atoms broke bonds with the Si atoms, and then re-bonded with nearby C atoms. This phenomenon resulted in significant structural changes as compared to their unpassivated counterparts. Hence, the relative stability order of the structures changed due to H-passivation, as can be found from the binding energies in tables 1 and 2.

To estimate the stabilities of the passivated structures, we calculate the binding energies of ($Si_{30}C_{30}H_{30}$) in the following way. First, we calculated the energy of the carbon-hydrogen bond,$[E(\mathrm{C}-\mathrm{H})_b]$ by removing a hydrogen atom from the surface of a passivated structure that was bonded with a carbon atom, and calculates the energy of the remaining structure without relaxing. Then, this energy and the energy of a hydrogen atom $\left(\frac{1}{2}E(\mathrm{H}_2)\right)$ was subtract from the total energy of passivated structure [E ($Si_{30}C_{30}H_{30}$)] to provide the energy value of $[E(\mathrm{C}-\mathrm{H})_b]$ (equation (3.1.3)). Second, similarly by removing a hydrogen atom bonded with a Si atom we have calculated the term $[E(\mathrm{Si}-\mathrm{H})_b]$ as in equation (4). If there are n number of C-H bonds and m numbers of Si-H bonds, $[n\,E(\mathrm{C}-\mathrm{H})_b + mE(\mathrm{Si}-\mathrm{H})_b]$ is the binding energy contributed by the H related bonding to the structures, and $(n\ +\ m) = 30$. The idea here is to take out the hydrogens' contribution to the binding energy from the passivated $Si_{30}C_{30}$ clusters. Now, given that the total atomic energies of b and d numbers of Si and C atom, $[bE(\mathrm{Si}) + dE(\mathrm{C})]$, the binding energy of ($Si_{30}C_{30}H_{30}$) structures are calculated by the following equations:

$$E(\mathrm{C}-\mathrm{H})_b = E(\mathrm{Si_{30}C_{30}H_{30}}) - [E(\mathrm{Si_{30}C_{30}H_{29}}) + \tfrac{1}{2}E(\mathrm{H_2})] \quad (3.1.3)$$

$$E(\mathrm{Si}-\mathrm{H})_b = E(\mathrm{Si_{30}C_{30}H_{30}}) - [E(\mathrm{Si_{30}C_{30}H_{29}}) + \tfrac{1}{2}E(\mathrm{H_2})] \quad (3.1.4)$$

$$E_b(\mathrm{Si_{30}C_{30}H_{30}}) = \frac{E(\mathrm{Si_{30}C_{30}H_{30}}) - [bE(\mathrm{Si}) + dE(\mathrm{C})] - [nE(\mathrm{C}-\mathrm{H})_b + mE(\mathrm{Si}-\mathrm{H})_b]}{60} \quad (3.1.5)$$

Where $E(...)$ refers to the total energy of the system indicated in the parenthesis.

The results of E_b and HOMO-LUMO gaps of relaxed passivated structures are listed in Table 3.1.4. **H-4-Hexa-C** structure in figure 3.1.3(a) shows the most stable structure with hydrogen passivation with the E_b of $-6.439\ \mathrm{eV/atom}$, and with a significantly lower HOMO-LUMO gap of $0.375\ \mathrm{eV}$. This is mainly due to the fact that hydrogen passivated Si atoms have 4-fold coordination and created favorable sp^3 like bonding environment. This is the only structure in this study where all the thirty Si atoms are 4-fold coordinated and the thirty C atoms are 3-fold coordinated. Hence, the two C hexagons on each side of the structure have adopted flatter configuration due to C-C sp^2 bonding, and hydrogenated silicon atoms occupy the curved edge sides with sp^3 bonds. Therefore, the initial $Si_{30}C_{30}$ sphere became a squashed structure by carbon hexagons from both sides. The stability of **H-4-Hexa-C** increased significantly compared to its unpassivated counterpart 4-Hexa-C (figure 3.1.2(e)). Even though stability increased by -0.369 eV/atom due to hydrogen passivation, the dipole moment increased by 0.16 Debye compared to its unpassivated structures.

The second most stable passivated structure was found to be the **H-C_{30}-bowl** structure figure 3(b) with a binding energy of $-6.249\ \mathrm{eV/atom}$. The passivation helped to reduce the distortion on the silicon side as compared to the unpassivated C_{30}-bowl structure. The relaxed H-C_{30}-bowl has four H atoms migrated to make C-H bonds. These four hydrogen atoms made bonds with the neighboring carbon atoms, and the Si-C-H bonds made a sp^3 bonding environment. The value of the HOMO-LUMO gap of the H-C_{30}-bowl structure is $1.108\ \mathrm{eV}$. Passivation for this structure also increased the dipole moment by 0.97 Debye, with a total dipole moment of 2.64 Debye. A highly non-spherical shape, especially on the Si part, is the main reason for the higher dipole moment.

H-tubular-$Si_{30}C_{30}$ structure figure 3.1.3(c) shows that all H atoms are still bonded with Si atoms after the relaxation, and the final structure looks like a dumb-bell shaped structure, as the 30 carbon atoms in the middle slightly tighten the structure. The binding energy is -5.880 eV/atom, and HOMO-LUMO gap of 1.328 eV and with a significantly short Si-Si average bond length of 2.29 Å. In the following, the HOMO plots will show that some of these bonds may qualify for Si-Si double bonds. This is one of the structures, where hydrogen passivation reduces the dipole moment by 0.10 Debye.

Figure 3.1.3(d) shows the **H-C_{15}-Si_{30}-C_{15}** structure where the C_{15} units squeezed the structure from the right and left cap of the bowl of fullerene. Some of the carbon atoms from these two C_{15}-units has significant distortions after relaxation; as a result, 12 hydrogen atoms broke bonds with silicon atoms and created new bonds with unsaturated carbon atoms; seven hydrogen atoms on one side and five on the other. Higher C-H bonds show here higher distortions. The number of Si-C bonds in the unpassivated structure (figure 3.1.2(b)) was 18, after passivation number of Si-C bonds reduced to 14. This shows significant reconfigurations within the structure after hydrogen passivation; as a result, the passivated structure is less stable by 0.979 eV/atom as compared to the unpassivated one (C_{15}-Si_{30}-C_{15}). The passivated structure has E_b of -5.795 eV/atom and HOMO-LUMO gap of 1.537 eV. The dipole moment of this structure is 3.81 Debye.

H-6-penta structure in figure 3.1.3(e) has an easily recognizable symmetry, there is a vertical mirror plane, and the two sides are then related by the mirror reflection and a 180^o degree rotation, which results in an inversion symmetry. Due to the inversion symmetry, this is the only hydrogen-passivated structure with a dipole moment of 0.00 Debye. The silicon atoms around the middle tightened the passivated relaxed structure. The mid-section Si atoms lose their hydrogen

atoms to the carbon atoms, as those Si atoms are four-fold coordinated. Each of side H-6-penta structure has three pentagon faces of carbon atoms, which bonded with three hydrogen atoms. This structure loses four Si-C bonds upon passivation, as does the previous structure. However, here some Si atoms, which lost hydrogen, bonded with each other to make the mid-section 4-fold coordination as seen in figure 3.1.3(e). This structure has the binding energy of -5.632 eV/atom and the HOMO-LUMO gap of 0.699 eV.

Figure 3.1.3(f) presents the **H-sphere2** structure, which distorted significantly after relaxation; its distortions are quite evident from the fact that it has the highest dipole moment among all the $Si_{30}C_{30}$ structures considered here, about 6 Debye. Note, the sphere2 (figure 3.1.2(h)) has the highest dipole moment of 3.20 Debye in their respective unpassivated structures group as well. Nineteen (19) hydrogen atoms rebounded with carbon atoms after relaxation. Therefore, the bonding features have been significantly changed as well throughout the surface of the structure. H-sphere2 structure has the binding energy of -5.631 eV/atom and a HOMO-LUMO gap of 1.343 eV.

For **H-sphere** in figure 3.1.3(g), the stability decreased by 0.922 eV/atom, and the HOMO-LUMO increased gap by 0.192 eV compared to the most stable structure H-4-Hexa-C. No significant distortion was found in this structure after relaxing; in fact, it remained like a spherical cage. In addition, the value of Si=C double bond length reported to be 1.77 Å [48][47] in earlier literature, which is larger than the average Si-C bond length, 1.74 Å, found in this structure as listed in Table 3.1.4; i.e., we have some Si=C double bonds here. 16 hydrogen atoms migrated to carbon atoms from Si atoms.

The least stable **H-4-Hexa-Si** structure is presented in figure 3.1.3(h), shows a distorted passivated structure. In this structure, 21 hydrogen atoms broke bonds with silicon atoms and

bonded with carbon atoms. There were 30 Si-C bonds in 4-Hexa-Si structure, whereas H-4-Hexa-Si has 23 of them. Also, the unpassivated 4-Hexa-Si has zero dipole moment with inversion symmetry, while with passivation, it gained a moment of 5.42 Debye. These are indications of the extent of distortions. The binding energy is -5.483 eV/atom and the HOMO-LUMO gap is 1.668 eV. Its stability is the lowest and the gap is the highest among all the $Si_{30}C_{30}$ structures considered here.

A note regarding hydrogen atoms migration from the silicon atoms to the carbon atoms: First, the reason each Si atom was bonded with one hydrogen atom was that in the starting templet Si_{60} fullerene, all the Si atoms are three-fold coordinated. Usually, larger Si-Si and Si-C bonds would not allow for any double bonds. However, because of relaxation, the local environment forces some of the Si-C and Si-Si distances to shorten enough to have double bonds. When a double bond is made involving a Si atom, that Si atom may not need that previously attached hydrogen atom. As a result, Si-H bonds became weaker during the relaxation. Second, in $Si_{30}C_{30}$ clusters with no hydrogen passivation, as each of the atom, either Si or C, before relaxation started with 3-fold coordination. When a carbon atom near a Si atom favors sp^3 bonds due to a local configuration, it gets the hydrogen from the Si atom as a C-H bond is much favorable than a Si-H bond. In this case, a carbon atom with a hydrogen atom became four-fold-coordinated. In both of these scenarios, hydrogen detached from these Si reattached to a nearby sp^3-like C atom.

4. HOMO-LUMO properties

In general, silicon prefers sp^3 hybridization, and forcing it to form sp^2 bonds leads to destabilization. The carbon can accommodate both sp^3 as well as sp^2 hybridization due to shorter C-C bond lengths [31][47][49][97][98][99]. However, there were reports of sp^2-like hybridization in silicon-carbide, and this matched with SiC graphene-like configurations, such as SiC multi-wall

nanotube [47][49]. Due to local chemical configurations in $Si_{30}C_{30}$ fullerenes, the molecular orbital calculations may establish the sp^2-like π bonds that we hypothesized in earlier sections. The orbital plots can verify such features. Figures 3.1.7 and 3.1.8 show the HOMO and LUMO plots for all the structures, without and with hydrogen passivation, respectively. In the following, we discuss a few selected HOMO and LUMO plots from the figures.

The HOMO plot of the C_{30}-bowl structure in figure 3.1.7(a) shows the π bond-like feature on the silicon side at the left-most part of the figure. Here, the Si-Si bond shows a bond-length of 2.31 Å. For comparison, previously published Si-Si double bonds were in the range of 2.15 to 2.23 Å [50][53]. On the other hand, for passivated H-C_{30}-bowl structure in figure 3.1.8(b), there is no sp^2 hybridization on the silicon side as all Si atoms, except four Si atoms, are passivated with hydrogen and have four-fold sp^3-like coordination; however, the π bond does show up on the carbon side of structure figure 3.1.8(b). In figure 3.1.8(c) for the H-tubular-$Si_{30}C_{30}$ structure, both the HOMO and LUMO appear on the carbon atoms in the middle of the structure. Si atoms do contribute significantly to these frontier orbitals, because the hydrogen passivated silicon atoms created almost perfect sp^3-like bonding environment with bonding angles of about 104°, whereas the ideal sp^3 bonding angles are 109.5°.

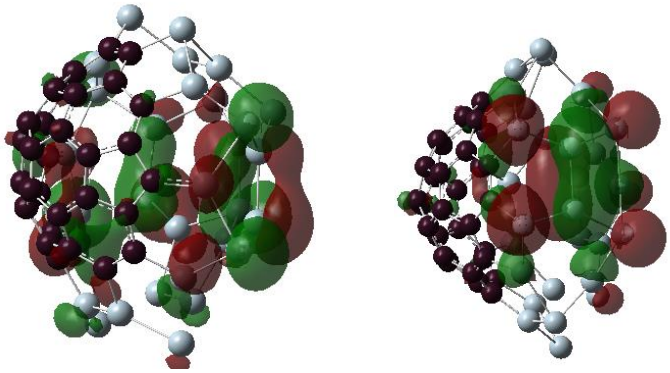

(a) C_{30}-bowl

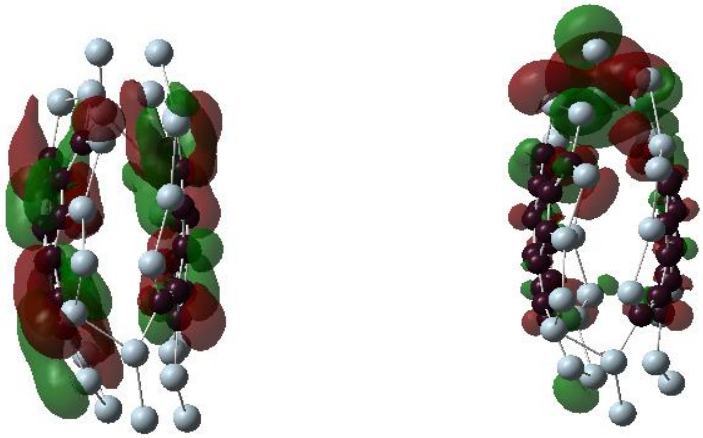

(b) C_{15}-Si_{30}-C_{15}

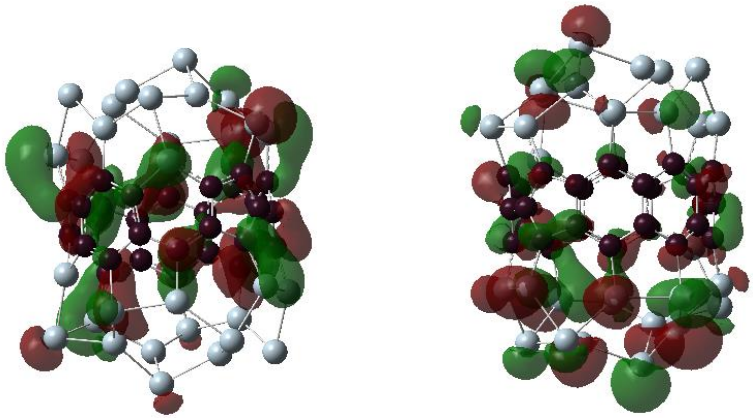

(c) tubular-$Si_{30}C_{30}$

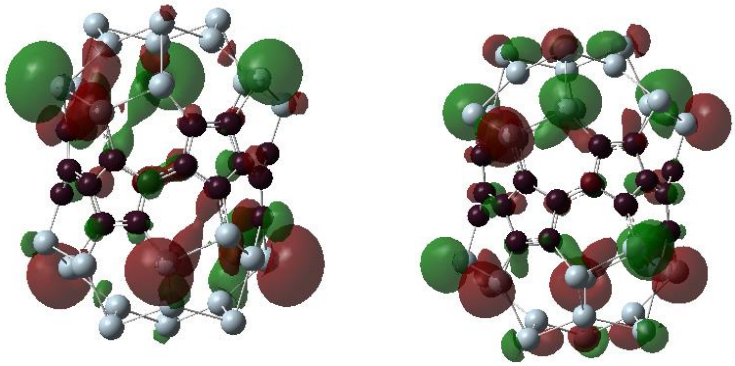

(d) 6-penta

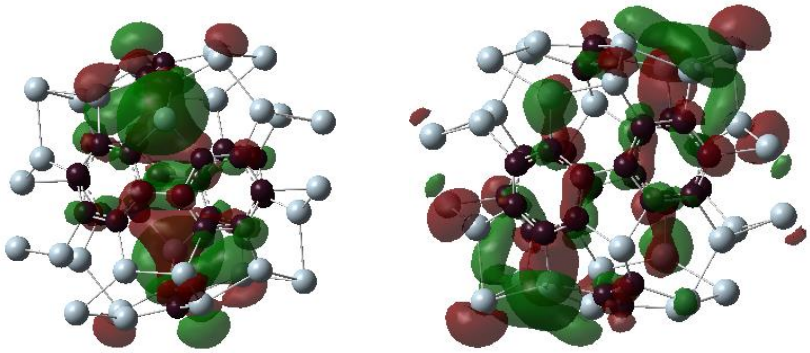

(e) 4-Hexa-C

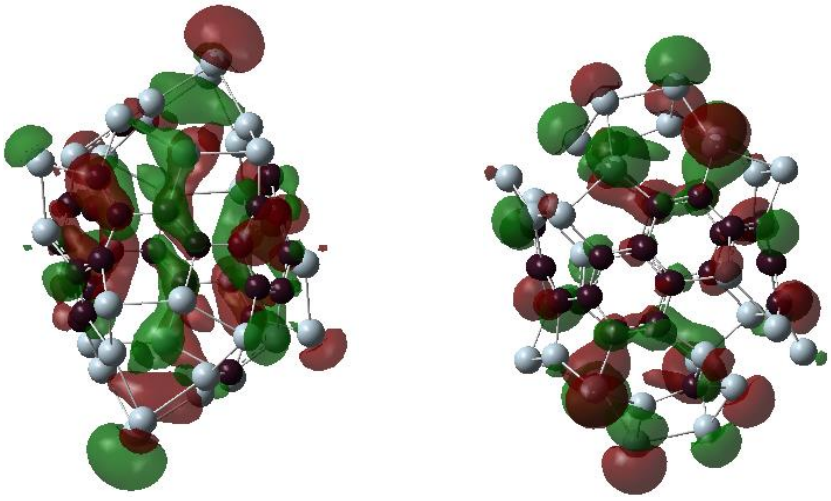

(f) 4-Hexa-Si

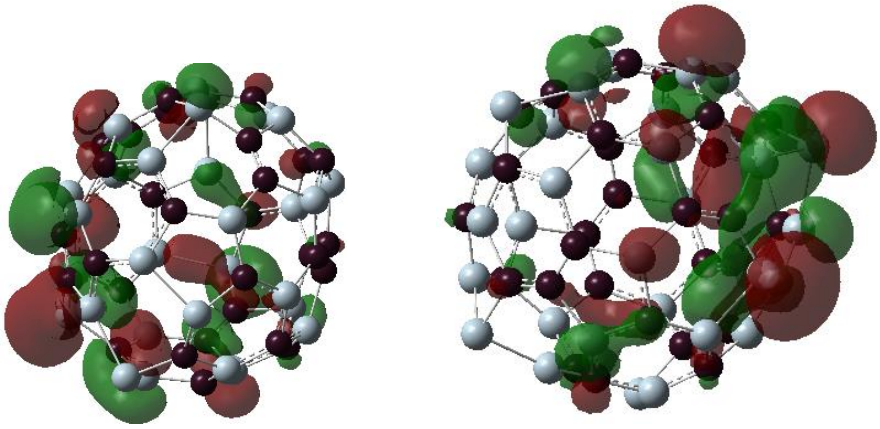

(g) sphere

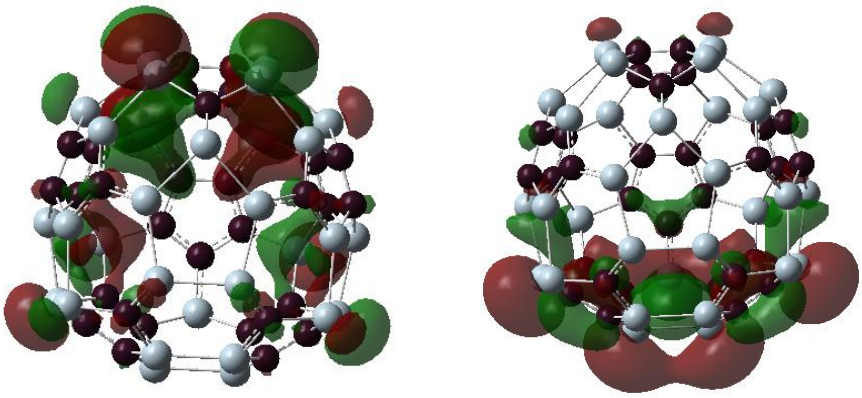

(h) sphere2

Figure 3.1.7. The left panel shows the HOMO and the right panel shows the LUMO plots started from the most stable strucure to the lowest stable strucure for unpassivated $Si_{30}C_{30}$ clusters. Structures are presented from (a) to (h) in order of their stability.

C_{15}-Si_{30}- C_{15} has HOMO, in figure 3.1.7(b) on both the C_{15} sides, almost symmetrically distributed, except on the two mid carbon atoms on both faces, these two carbon atoms are doubly bonded on the respected faces. Most of the Si atoms are not contributing to HOMO. LUMO consists of mostly Si atoms on one of the mostly distorted side of the structure. Interestingly, **H-C_{15}-Si_{30}- C_{15}** in figure 3.1.8(d) shows the HOMO in one of the C_{15} caps, particularly on the side where more hydrogen atoms are broken away from Si atoms and re-bonded with C-atoms. On the other hand, LUMO, as its unpassivated counterpart, is on the side of the structure that is more distorted with Si atoms without hydrogen atoms. The highest contribution for LUMO came from a pair of Si and C atoms that are separated by 3.66 Å.

HOMO and LUMO are mainly distributed on the Si caps in the 6-penta structure in figure 7(d). Unlike some other structures, no π-bond like feature was found on the HOMO plot. H-6-penta in figure 3.1.8(e) has main contributions to HOMO and LUMO are from the Si atoms that are three-fold coordinated and without hydrogen atoms, and from a few carbon atoms. Therefore, bonding-antibonding splitting that created HOMO and LUMO occurs almost on the same set of atoms. The eight four-fold-coordinated Si atoms in the mid-section of the structure remained tightly bound, with no contribution to either HOMO or LUMO. H-sphere2 has the shortest Si-Si bond, 2.24 Å, which is significantly close to experimental Si-Si double bond length values, as quoted earlier [50-53]. The HOMO plot in figure 3.1.8(f) reflects the π bond between two silicon atoms.

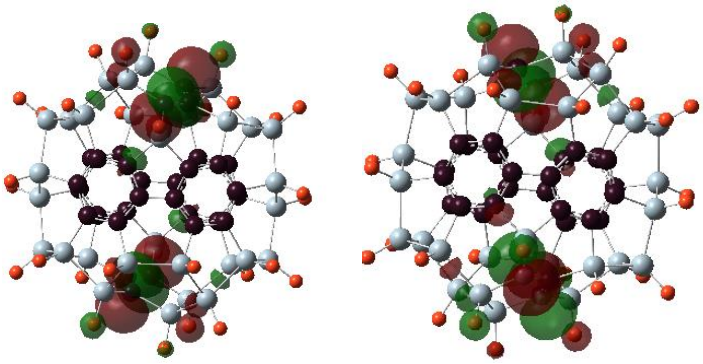

(a) H-4-Hexa-C

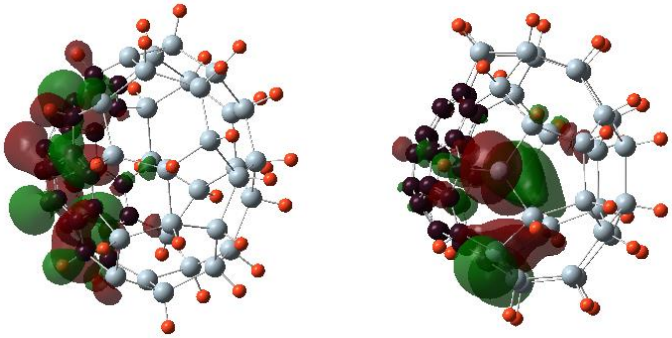

(b) H-C_{30}-bowl

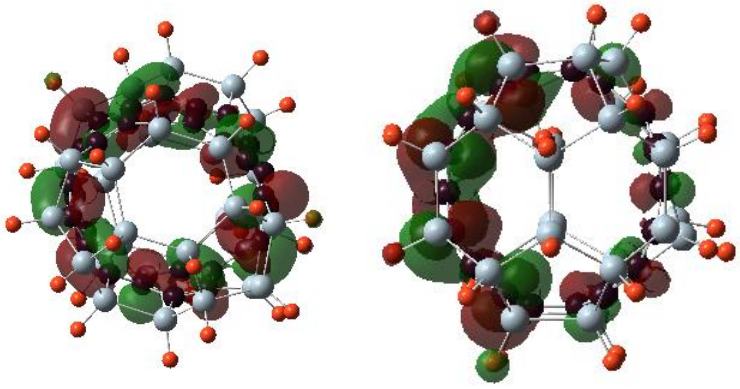

(c) H-tubular-$Si_{30}C_{30}$

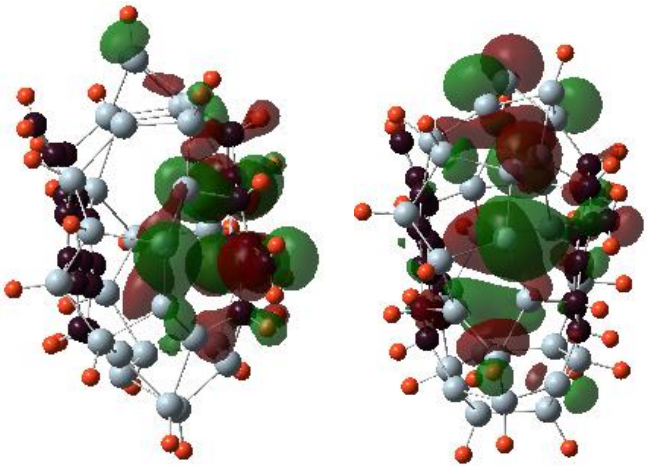

(d) H-C_{15}-Si_{30}-C_{15}

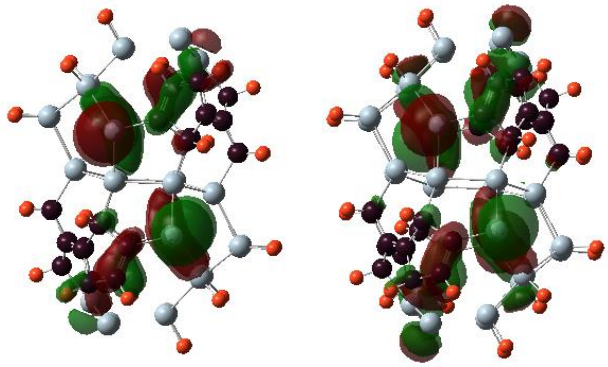

(e) H-6-penta

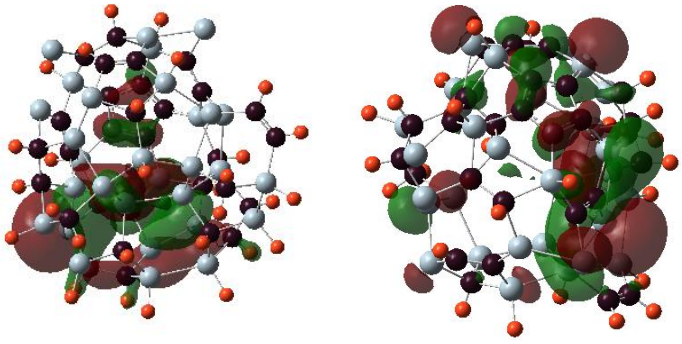

(f) H-sphere2

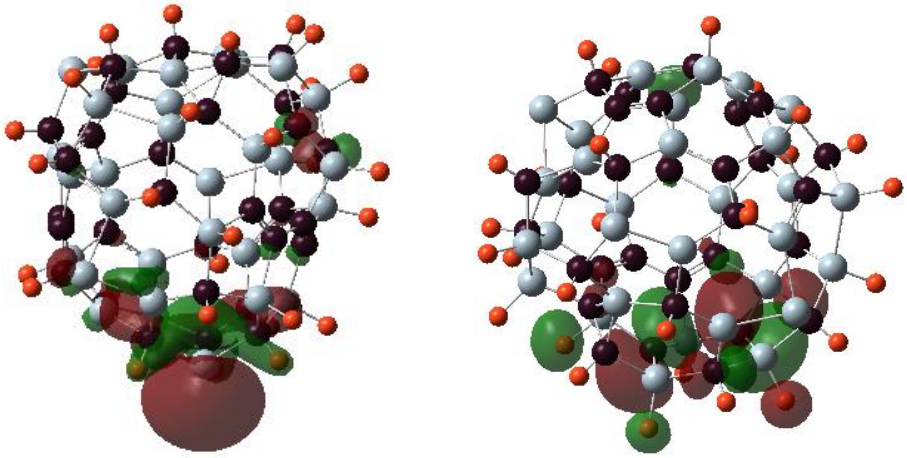

(g) Sphere

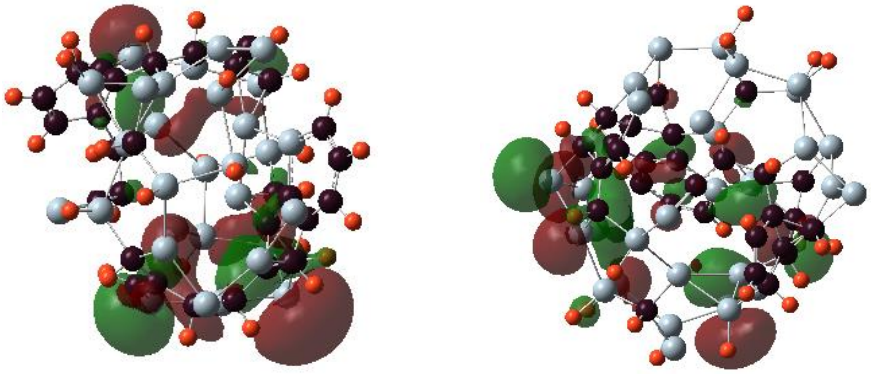

(h) H-4-Hexa-Si

Figure 8: The left panel shows the HOMO and the right panel shows the LUMO plots started from the most stable strucure to the lowest stable strucure for hydrogenpassivated $Si_{30}C_{30}H_{30}$ clusters. Structures are presented from (a) to (h) in order of their stability.

Regarding the double bonds, we make some remarks here: when a bond is well-formed, the orbitals' energy for that bond becomes lower in energy and it does not contribute to HOMO. In the unpassivated $Si_{30}C_{30}$ structures, atoms that contribute to HOMO are prone to distortion or are not still in their preferred bonding state. For example, in the C_{30}-bowl structure, both HOMO and LUMO have major contributions from the unpassivated Si atoms. Once these Si atoms are hydrogenated, in the H-C_{30}-bowl structure Si part of the structure does not contribute to these frontier orbitals anymore, and these Si atoms tend to have sp^3 like bonding with the help of passivating agents such as hydrogen. Therefore, some Si-Si double-bonds showing up in HOMO in the unpassivated structures are prone to be reactive with chemical stimulations; with passivation, these bonds orient in standard sp^3 hybridization. For example, in both the most stable C_{30}-bowl and lest stable sphere-2 structures, there were indications for Si-Si double bonds from the HOMO plots. However, with hydrogen passivation, these double bond features were lost. This will be more natural features, as any chemical synthesis of these structures will possibly be passivated by the available ligands in the synthesis environment. Hence, the detection of Si-Si double bonds in these larger structures is unlikely.

Chapter 4

4.1. Endohedral Doping of Transition Metal Atoms at C_{60}, $Si_{30}C_{30}$, C_{70} and $Si_{35}C_{35}$ Fullerenes

In this section we are going to investigate the magnetic and electronic properties of endohedral doping of transition metal atoms (Fe, Nb, Hf, Ta, and W) at C_{60}, $Si_{30}C_{30}$, C_{70} and $Si_{35}C_{35}$ fullerenes.

4.1.1. Computational Methods

A. Gaussian 09:

The DFT [88], with B3LYP hybrid functional [89] as applied in the Gaussian 09 set of codes and atomic wave functions LAN2DZ base set [77] (Los Alamos National Laboratory 2 Double-Zeta) [90] is used to analyze the C_{60}, and $Si_{30}C_{30}$ fullerenes. Also, their endohedrals doping of transition metal atoms (W, Fe, Ta, Hf, and Nb).

The binding energy (E_b) in uniting (eV/atom), the highest occupied molecular orbital (HOMO) the lowest occupied molecular orbital (LUMO) in a unit of (eV), a magnetic moment in uniting of and other structural characteristics were measured. For example, the binding energy value can be measured by following these equations.

$$E_b(\mathrm{C_{60}M}_d) = \frac{E(\mathrm{C_{60}M}_d) - 60E(\mathrm{C}) - dE(\mathrm{M}_d)}{60+d} \qquad (4.1.1)$$

Equation (4.1.1) represents the equation of binding energy, where $\mathrm{E(C_{60}M}_d)$ is the total energy of relaxed structure and $E(\mathrm{C})\ and\ E(\mathrm{M}_d)$ are the total atomic energy of carbon and doping of transition metal atoms; M= (Fe, Nb, Hf, Ta, and W) ; d=1.

For the binding energy of endohedral doping Si_mC_n fullerenes can be calculated by the following equation,

$$E_b(\mathrm{Si}_m\mathrm{C}_n\mathrm{M}_d) = \frac{E(\mathrm{Si}_n\mathrm{C}_b\mathrm{M}_d) - nE(\mathrm{Si}) - mE(\mathrm{C}) - dE(M)}{m+n+d} \quad (4.1.2)$$

Equations (4.1.2) represent the equation of binding energy of $\mathrm{Si}_m\mathrm{C}_n\mathrm{M}_d$ fullerenes. Also, $E(\mathrm{C}), E(Si), E(M)$ and $E(\mathrm{Si}_m\mathrm{C}_n\mathrm{M}_d)$ are total atomic energies of the C, Si, and transition metal atoms M= (Nb, Fe, Hf, Ta, and W) and total energy of relaxed $E(\mathrm{Si}_n\mathrm{C}_b\mathrm{M}_d)$ fullerene. Where m=n= 30 or 35 atoms, d = 1 or 2 atom(s), m+n+d= 61, 62, or 71 atoms.

4.1.2. Endohedrals Doped C_{60} Fullerene:

Endohedral fullerenes have extra atoms, ions, or clusters within the spheres, also called endofullerenes (Chai, et al., 1991). The carbon atoms on C_{60} fullerene are all bonded with either single or double covalent bonds. Also, the C_{60} fullerene is a symmetrical sphere. As a result, if atoms are put in the center of the C_{60} fullerene, the doped atoms do not interact much with the cage wall. They can retain almost all spin magnetic moments corresponding to the dopant atoms' electron configurations. The study here aims to examine the magnetic properties of the C_{60} fullerene structure and its stability. Also, we propose that adding a transition metal Fe, Nb, Hf, Ta, and W atoms in the center of the C_{60} fullerene will effect on the magnetic properties on the fullerene. Also, it will increase the single and double bond length of the C_{60} fullerene. Figure 4.1.1 shows the relaxed structures of the M@C_{60} fullerenes. Also, figure 4.1.2 show the binding energy of C_{60} and its endohedrally doped of transition metal atoms where the stability decreases while when we add a transition metal atom in the center of C_{60} fullerenes.

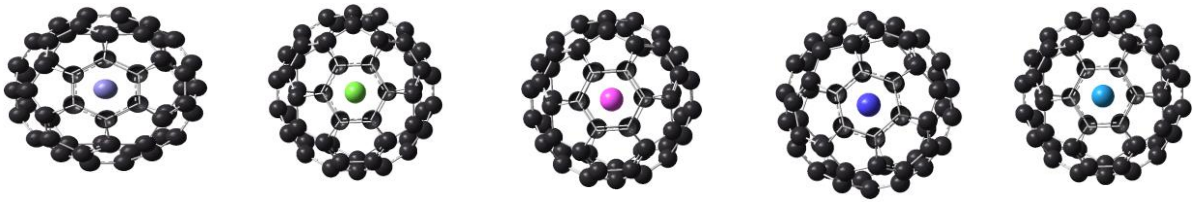

(a) $Fe@C_{60}$ (b) $Nb@C_{60}$ (c)$Hf@C_{60}$ (d) Ta@C60 (e) $W@C_{60}$

Figure 4.1.1: showed the relaxed structures of $M@C_{60}$ fullerene, where M= Fe at (a), Nb at (b), Hf at (c), Ta at (d), and W at (e).

The $Fe@C_{60}$, shown in figure 4.1.1(a) fullerene, is the second most stable structure of endohedral doping of transition metal study. This structure has binding energy by -6.466 eV/atom and a HOMO-LUMO gap of 2.358 eV, compared to the HOMO-LUMO gap of C_{60} fullerene, which decreases 0.43eV. The $Fe@C_{60}$ diameter has a value of 7.139 Å, which is 0.01 Å shorter than calculated pristine C_{60} fullerene. The optimized bond lengths for $Fe@C_{60}$ are within 1.405-1.406 Å and 1.45 Å for double and single bonds, respectively. As expected, these two bonds length are larger than the C_{60} fullerene values of 1.394 and 1.458 Å.

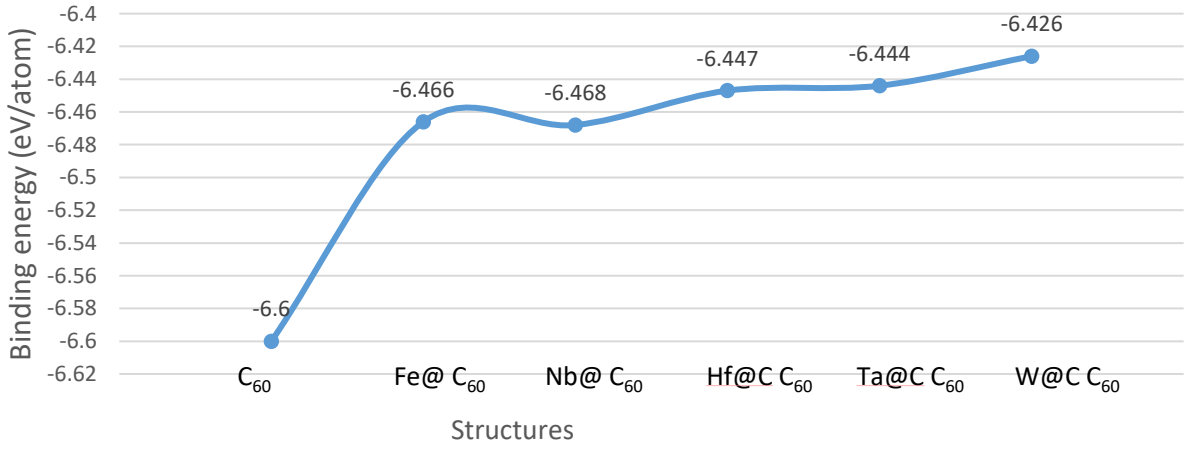

Figure 4.1.2 shows the binding energy of C_{60} and its endohedrally doped of transition metal atoms

The Nb atom isolated in the center of the C_{60} fullerene is the most stable structure among the $M@C_{60}$ fullerenes studied here. It has the binding energy -6.468 eV/atom. Also, the $Nb@C_{60}$ fullerene has the highest HOMO-LUMO gap of 2.990 eV, which is 0.112 eV higher than C_{60}

fullerene. Moreover, the diameter of the fullerene increased for the endohedrals doped of Nb atom with a value of 7.152Å, compared to the pristine C_{60} diameter of 7.149 Å calculated and 7 Å experimentally[8]. Also, the bonds between carbon atoms were increased by 0.02Å on double and single bonds compared to the C_{60} double and single bonds values.

Table 4.1.1: The calculation of binding energy(E_b), HOMO-LUMO gap (E_g (eV)), diameter (D) (Å), single and double bonds (b_s and b_d) (Å).

M@C_{60}	E_b (eV/atom)	HOMO-LUMO gaps (eV)	Shortest single bond(Å)	Average single bond(Å)	Shortest double bond(Å)	Average double bond(Å)	Diameter(Å)	Multiplicity
Fe@C_{60}	-6.466	2.358 0.951	1.465	1.465	1.405	1.406	7.139	Triplet
Nb@C_{60}	-6.468	2.990 0.818	1.452	1.457	1.396	1.401	7.152	Quartet
Hf@C_{60}	-6.447	0.712 2.032	1.464	1.465	1.406	1.411	7.15	Triplet
Ta@C_{60}	-6.444	1.706 1.864	1.466	1.466	1.408	1.408	7.163	Quartet
W@C_{60}	-6.426	1.666 0.905	1.465	1.466	1.407	1.408	7.159	Triplet

The following structure is called Hf@C_{60} fullerene when the Hf atom is doped in the center of C_{60} fullerene. The binding energy increased by 0.154 eV compering to the calculated binding energy of C_{60} fullerene. As a result, HOMO-LUMO gaps are found at the Hf@C_{60} fullerene by 0.712 eV. This is the smallest value of HOMO-LUMO gaps among other endohedral doping transition metals atoms in this paper. Other effects on the electronic configuration of transition metal doped (Hf) on C_{60} fullerene are increasing the diameter, double, and single bonds by 0.02 Å, 0.02 to 0.03 Å, and 0.01 to 0.02 Å.

The Ta@C_{60} fullerene (figure 4.1.1(d)) has 0.156 eV higher binding energy than the C_{60} fullerene. However, comparing the HOMO-LUMO gap, the Ta@C_{60} fullerene has a lower value than C_{60} fullerene by 1.172 eV. Ta atom doping increased the diameter and the double and single bonds by 0.01Å and 0.02Å.

Finally, figure 4.1.1(e) represents the snapshot structure of W@C_{60} fullerene. The W@C_{60} fullerene is an unstable structure among other systems in this section because it has the highest binding energy value -6.426 eV/atom. The W@C_{60} fullerene has a value of HOMO-LUMO gap by 1.666 eV, which is lower 1.212 eV than the C_{60} HOMO-LUMO gap, as shown in table1. Moreover, W doped atom has shown electronic effects on C_{60} fullerene by increasing the diameter, double and single bonds 0.02Å

4.1.3. Endohedral Doping of Transition Metal Atoms in $Si_{30}C_{30}$:

4.1.3-A Tungsten (W) Atoms Doping at C_{30}-bowl Structure and their Passivation:

For the endohedral doping of the tungsten atom, the configuration of the C_{30}-bowl structure is considered. The reason for selecting the C_{30}-bowl is that without passivation, it was the most stable $Si_{30}C_{30}$ configuration, and it kept a cage-type feature; secondly, its stability increased with passivation (by 0.035 eV/atom), and the cage feature improved as well. Figure 4.1.3(a) shows the relaxed **W-C_{30}-bowl** structure. The initial structure was constructed from $Si_{30}C_{30}$ fullerene in C_{30}-bowl configuration and W atoms were placed at the sphere's center, and then the structure was relaxed without any symmetry constraint. Figure 4.1.3(b) similarly obtained structure, this with a W-dimer inside the cage, **W_2-C_{30}-bowl**. The W_2-C_{30}-bowl was found magnetically not very interesting, as the W-dimer in the cage prefers not to retain spin magnetic moments. So the

following discussion is based on a single W atom in $Si_{30}C_{30}$, W-C_{30}-bowl structure (figure 4.1.3(a)).

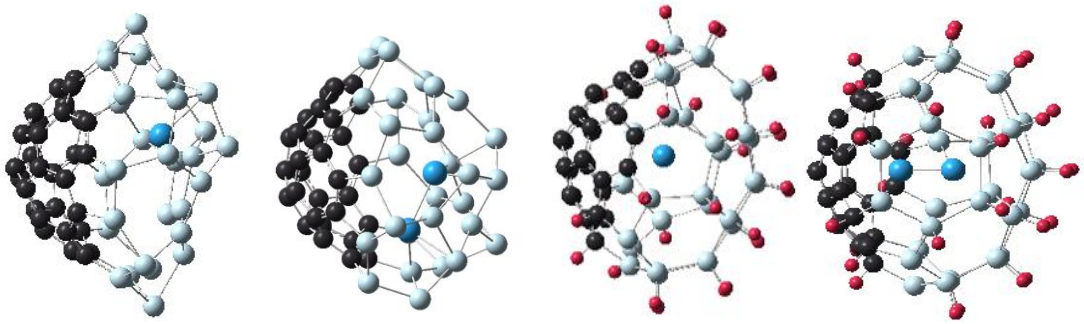

(a)W-C_{30}-bowl (b) W_2-C_{30}-bowl (c) H-W-C_{30}-bowl (d) H-W_2-C_{30}-bowl

Figure 4.1.3: These figures show the C_{30}-bowl structure with tungsten atom(s) in the center for unpassivated and passivated structures.

Sever spin-multiplicities have been considered for W-C_{30}-bowl. From the binding energy, the spin-triplet state was found to be 1.403 eV more stable than the singlet state. In all spin-states considered, after relaxation, the W atom moved towards the Si side. The C_{30} side remained almost unaffected with fullerene-like structure. In the triplet state, there is only one W-Si bond, with a bond length of 2.57 Å, which is similar to other W-Si bonds found in the literature [35]. On the other hand, in the singlet state, the W atom is three-fold coordinated with an average bond-length of 2.53 Å. For the triplet spin state structure, W atom does possess almost all the spin, namely 1.85 μ_B, out of total magnetic moment of 2 μ_B. In contrast, in the hydrogen passivated H-W-C_{30}-bowl structure, where Si atoms are passivated by hydrogen atoms, the spin-magnetic moment on the W atom is 1.99 μ_B, and the W atom remained almost at the center of the cage without any bond. A similar effect was found for the structure with an even higher spin-multiplicity of 5 state, 3.99 μ_B

was found on the W atom out of total 4 μ_B and sitting at the center of the H-W-C_{30}-bowl structure. With hydrogen passivation, spin-multiplicity state 5 is slightly more stable than spin-multiplicity state 3 for the H-W-C_{30}-bowl structure, by 0.030 eV. Retention of spin magnetic moment on the endohedral transition atom is much higher in $Si_{30}C_{30}$ cages than what was reported inside smaller Si cages [54].

In addition, W atom increased the binding of C_{30}-bowl structure by 0.084 eV/atom and decreased the dipole moment by 59%; this implies that the stability of the overall structure improved by the W atom doping. Note that with W in H-C_{30}-bowl, the HOMO-LUMO gap increased to 1.597 eV, implying increased electronic stability compared to the undoped structure. In short, two important findings here are with W atom in conjunction with hydrogen passivation: (i) higher spin moment is retained at the W atom sitting at the center of the cage, and (ii) the cage stability increases.

4.1.3-B Single Atom Doping at Sphere Structure:

The doping atom in the fullerene center can have a significant magnetic moment. In addition, electronic properties such as bond length and diameter will be affected. So, the magnetic and electronic properties aim for this endohedral doping of transition metal atoms study and do not predict the ground-state structure. The endohedral metal atom doped structures will be represented by sphere-M_a, where M_a is the transition metal atoms inside the sphere structure, where M= Fe, Nb, Hf, Ta, and W; a=1, and 2. The electronic structures of sphere-M_a were calculated with various spin-multiplicities calculations. Not all bonds in Sphere structure are saturated, as was found for the C_{60} fullerene. As a result, there will be some dangling bonds on the surface of the sphere structure. So, we expect higher interactions between the doped atom and the cage surface compared

to that found in the C_{60} structure. Figure 4.1.5 shows the binding energy for $Si_{30}C_{30}$ fullerene and its endohedrally doped of transition metal atoms. Also, it shows that the stability decreases with transition metal doping in $Si_{30}C_{30}$ fullerene.

Figure 4.1.4-(a) shows the relaxed structure of endohedral doped of Fe atom, called sphere-Fe. Moreover, in the electron properties, the sphere-Fe structure has a binding energy of -4.623 eV/atom, and the HOMO-LUMO gap is 0.712eV. The Fe atom remains almost in the center of the cage, with an average diameter of sphere-Fe is 9.148 Å. The sphere-Fe average Si-Si bonds length has 0.011 Å longer comparing the average Si-Si bonds length to the sphere, without any doping atom, structure, figure3.1.1. Also, the average of C-C, Si-Si, and Si-C bonds are 1.462 Å, 2.262 Å, and 1.829 Å.

Nb atom is the 4d orbital of the transition metal atom, with an electronic configuration $4d^4 5s^1$. Figure 4.1.4 (b) shows the relaxed endohedral doping of the niobium atom. For sphere-Nb with different spin multiplicities considered. The doublet state is more stable than the quartet state by 0.016 eV/atom. In addition, sphere-Nb structure has the lowest binding energy for Endohedral doping of Transition Metal Atoms in $Si_{30}C_{30}$. The diameter of sphere-Nb is 9.067 Å which is longer than sphere diameter by 0.127 Å.

For sphere-Hf, the Hf atom doping in the center of the sphere structure revealed an opposite trend compared to the ones discussed above. Moreover, the triplet state for the sphere-Hf structure showed higher stability than the single state calculation by 0.012 eV/atom, as shown in Table 4.1.2. The diameter of sphere-Hf is 9.067 Å and the C-C bond is 1.451 Å.

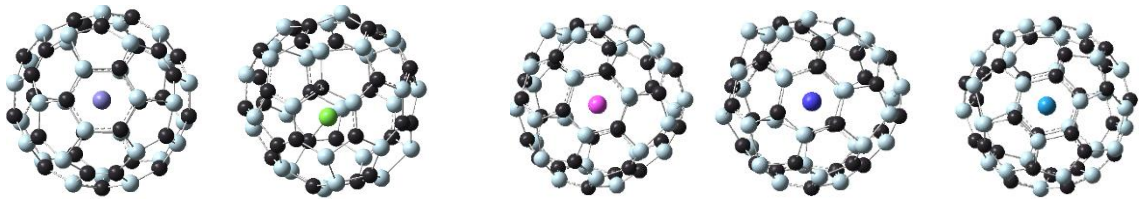

(a) sphere-Fe (b) sphere-Nb (c) sphere-Hf (d) sphere-Ta (f) sphere-W

Figure 4.1.4: showed the relaxed structures of endohedral doping of transition metal M inside the sphere, where M= Fe, Nb, Hf, Ta, and W.

Tantalum atom is a transition metal atom with 5d orbital, and the electronic configuration is $4f^{14}5d^{3}6s^{2}$. The Ta atom(s) doped sphere structure, sphere-Ta, is shown in finger4.1.4-(d). With different spin state calculations, the doublet state calculation shows the stability of sphere -Ta among all the spin state calculations, which lower 0.008 eV/atom than quartet's state. In addition, sphere-Ta diameter and average C-C, and Si-Si bonds are 9.071 Å, 1.421 Å, and 2.276 Å.

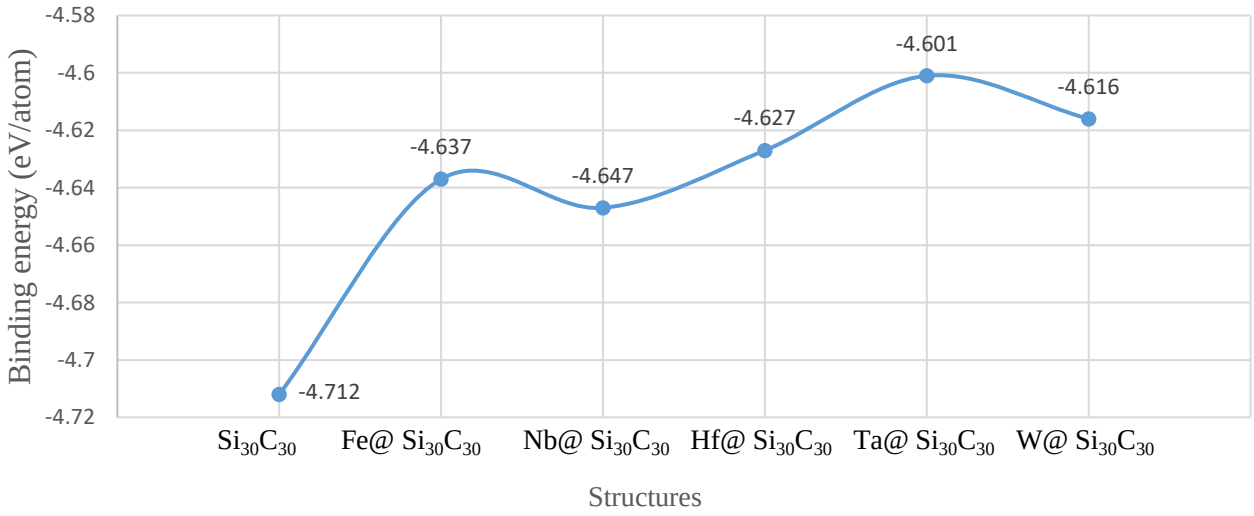

Figure 4.1.5 shows the binding energy for $Si_{30}C_{30}$ fullerene and its endohedrally doped of transition metal atoms

Figure 4.1.4-(f) shows the relaxed structures for endohedral doped W atom. The cage is sphere-W, with an average diameter of 9.12 Å, which is wider than the pristine sphere structure by 0.182Å. Also, the average of Si-Si bonds length is increased by 0.02Å compared to sphere

structure. The sphere-W structure shows a value of binding energy(E_b), is -4.616 eV/atom for the electronic properties, and the HOMO-LUMO gap is 0.792 eV.

Table.4.1.2: show the calculation of the binding energy (E_b)(eV/atom), HOMO-LUMO gaps (Eg (eV)), dipole moment, and atomic charge of M, multiplicity.

Sphere-M	Eb(eV/atom)	HOMO-LUMO gaps (eV)	atomic charge of M atoms	dipole moment (Debye)	Multiplicity
sphere-Fe	-4.590	0.488	0.909	0.270	Singlet
sphere-Fe	-4.637	0.712 2.032	0.673	0.264	Triplet
Sphere-Nb	-4.647	0.695	4.4583	0.742749	Doublet state
sphere-Nb	-4.631	0.566	1.4815	0.937511	Quartet state
sphere-Hf	-4.614	0.785	1.0749	0.477	Singlet state
sphere- Hf	-4.627	0.815 1.537	0.9150	0.344	Triplet state
sphere-Ta	-4.601	1.003 0.638	3.3284	0.231	Doublet state
sphere-Ta	-4.593	1.116 0.754	2.0204	0.232563	Quartet state
sphere-W	-4.599	1.631	0.657	0.210	
sphere-W	-4.616	0.792 0.952	1.261	0.282	Triplet state

4.1.3-C Dimer-Atom Doping:

In this section, we study the electron properties of transition metal atom dimers in the sphere structure. While the transition metal atoms of 4d and 5d orbitals. The transition metal atoms Nb, Ta, Hf, W, and Fe, are chosen to form dimers. Figure 4.1.6 shows the relaxed structures of endohedral doping of transition metal M_2 inside the sphere, where M= Nb. Ta, Hf, W, and Fe

Figure 4.1.6(a) shows the relaxed structure of endohedral doping of Fe-dimer in the sphere structure. The Fe-dimer atoms remain in the center of the sphere with a bond length of 2.407Å, which is close to the experimental Fe-dimer value of bond length is 2.72 Å [102]. Thus, the triplet state has low binding energy and high HOMO-LUMO gaps than the singlet state calculation, which is -4.590 eV/atom and 1.566 eV for triplet state and -4.505 eV/atom and 0.842 eV for singlet state.

Sphere–Nb_2 is the most stable structure by hold the lowest binding energy. The binding energy(E_b), is -4.726 eV/atom in singlet states calculation, Table 4.1.3, lower than 0.022 eV/atom than the spin-triplet state. Nb-dimer inside the cage beaver almost the same Ta-dimer. After relaxation, the Nb-dimer breaks its bond, moves in the opposite direction, and bonds with Si and C on the cage surface. The Nb-dimer bond length increases after relaxation are 2.86 Å in a spin-singlet state calculation and 3.22 Å in a spin-triplet state.

The endohedral doping structure of the Hf-dimer has a low value of binding energy, which is -4.627eV/atom for singlet state and -4.699 eV/atom for triplet state calculations. Moreover, the Hf-dimer has behaver interestingly inside the cage which dimer bond is brook down, and each atom attracted to hexagon face of the cage by bonded with carbon atoms located in that hexagon face.

Sphere-Ta_2 is the following structure. The sphere–Ta_2 showed higher stability in triplet state; 0.005 eV/atom lower than the single state calculation. HOMO-LUMO value of the stable structure is 1.025eV for spin-up and 0.867 eV for spin-down, as shown in Table 4.1.3. Ta-dimer was found to interact with the cage's surface rather than interacting with each other; Ta-dimer breaks its bond but moves in the opposite direction. Each Ta atom bonded with Si and C atoms of the cage surface. The Ta-dimer bond length increases after relaxation, which is 2.897 Å in singlet state calculation and 3.643 Å in triplet state calculation.

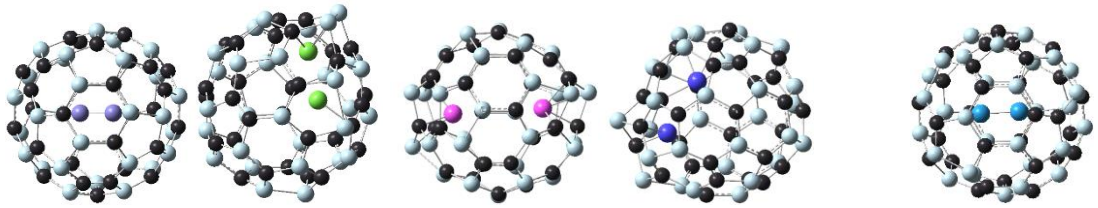

(a) sphere-Fe_2 (b) sphere-Nb_2 (c) sphere-Hf_2 (d) sphere-Ta_2 (e) sphere-W_2

Figure 4.1.6: shows the relaxed structures of endohedral doping of transition metal M_2 inside the sphere, where M= Fe, Nb. Hf, Ta, and W.

The triplet state in W-dimer doping has a 0.005 eV/atom lower binding energy than the singlet state in terms of stability. Furthermore, the triplet state has a spin-up HOMO-LUMO gap of 0.938 eV and a significantly higher 2.568 Debye of diploe moment. The W-dimer remains in the center of the cage with a 2.183Å bond length. In the center of the sphere structure, this W-dimer, where the bond length is longer by 0.074Å than the free W-dimer bond length.

Table 4.1.3: show the calculation of the binding energy (E_b) (eV/atom), HOMO-LUMO gaps (Eg (eV)), dipole moment and atomic charge of M_2, and atomic spin density f M_2 for Sphere- M_a where M= Nb, Ta, Hf, W, and Fe.

Sphere-M_2	Eb(eV/atom)	HOMO-LUMO gaps (eV)	atomic charge of M_2 atoms	dipole moment (Debye)	Multiplicity
Sphere-Fe_2	-4.505	0.842	0.7102	0.093 0.487	Singlet state
Sphere-Fe_2	-4.590	1.566 0.682	1.2701	0.034 0.610	Triplet state
sphere-Nb_2	-4.726	1.253	4.1815	0.275795 0.167629	Singlet state
sphere-Nb_2	-4.704	1.062 1.152	1.5152	0.254327 0.451862	Triplet state
sphere-Hf_2	-4.695	0.876	0.7795	0.987 0.724	Singlet state
sphere-Hf_2	-4.699	0.892 0.974	1.7355	0.967 0.745	Triplet state
sphere-Ta_2	-4.703	0.639	5.823	0.568 0.361	Singlet state
sphere-Ta_2	-4.708	1.025 0.867	3.2827	0.425149 0.255301	Triplet state
sphere-W_2	-4.635	0.837	0.657	-0.015 0.580	Singlet state
sphere-W_2	-4.630	0.938 1.266	2.568	0.435 0.581	Triplet state

4.1.2 Magnetic Moments Properties.

4.1.2-1 Endohedral Doping of Transition Metal Atoms at C_{60}:

In this section, we are investigating the magnetic properties of endohedral doping of transition metal atoms. Figure 4.1.9 shows the magnetic moment where the blue line represents the magnetic moment for free atom and the orang line represent the magnetic moments of doped atoms of transition metal atoms at C_{60} fullerene. So, we will start our result with Fe@C_{60} fullerene. Where the Fe atom is one of the ferromagnetic metals [103], in our result, the Fe atom has an amount magnetic moment of 1.94 μ_B which is similar to the magnetic moment of a free Fe atom in triplet state, as shown in figure 4.1.9. From figure 4.1.7-(a), the charge density is mostly around the sphere's center where the Fe atom is located. These facts suggest that the Fe at the center of the C_{60} fullerene behaves almost like a free Fe atom. Also, Molecular orbital (MO) of HOMO (the highest occupied molecular orbital) calculation shows that the Fe atom is not interacting with the cage, as shown in figure 4.1.7-(a). As a result, the Fe atom in the sphere's center will be protected from outside influence. The second structure that we are investigating is the Nb@C_{60} fullerene. Within the fullerene, the Nb atom acquired a value of a magnetic moment of $4\mu_B$. While as a free atom, its magnetic moment is 3 μ_B as shown in figure 4.1.9. Moreover, the Nb atom interacts with cage atoms, as shown in figure 4.1.8. As a result, the cage atoms share $1\mu_B$ with the Nb. The following structure of our study will be Hf@C_{60} fullerene. The Hf atom is not very magnetically interesting compared to others M@C_{60} in this study by having $1.065\mu_B$ as shown in figure 4.1.9.

Table 4.1.4: shows the magnetic moment for free (single atom and dimer atoms) also a single atom @ C_{60}, C_{70}, $Si_{30}C_{30}$, $Si_{35}C_{35}$ and Dimer-atoms @ $Si_{30}C_{30}$). The multiplicity (Mu)

Atoms	Magnetic moment (for atom)	Magnetic moment (for Dimer)	Magnetic moment (for atom @C_{60})	Magnetic moment (for single atom @$Si_{30}C_{30}$)	Magnetic moment (for Dimer-atoms @ $Si_{35}C_{35}$)	Multiplicity
Fe	2.0	1.0 1.0	1.94	4.00	3.886 -1.195	Triplet
Nb	3.0	1.0 1.0	4.0	1.255	-0.355 1.221	Quartet for a single atom Triplet for dimer
Hf	2.0	1.0 1.0	1.065	1.836	0.666 0.430	Triplet
Ta	3.0 Quartet state)	1.0 1.0	3.0 Quartet state)	-2.966 (Doublet state)	0.851 0.186	Triplet for dimer
W	2.0	1.0 1.0	2.0	5.586	2.819 -1.834	Triplet

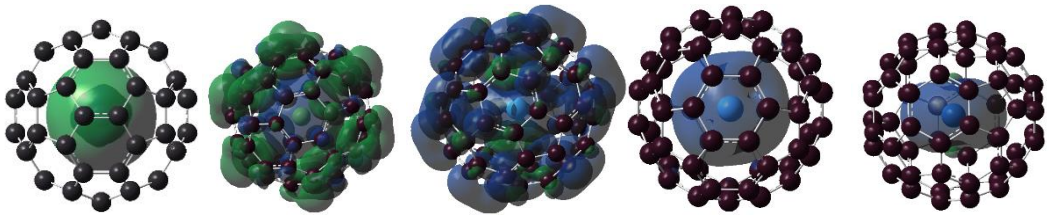

(a) Fe@C_{60} (b) Nb@C_{60} (c) Hf @ C_{60} (d) Ta@C_{60} (e) W@C_{60}

Figure 4.1.7: showed the total electronic charge density calculation of C_{60} fullerene and M@C60 fullerene; where M= Nb at figure (b), Fe at (c), Ta at (d), Hf at (e), and W at (f)

Ta@C_{60} fullerene is the following structure that we study. Where the Ta atom at the center of the sphere holds a magnetic moment of $3.025\ \mu_B$, as shown in figure 4.1.9, whereas the total magnetic moment of a free Ta atom is $3\mu_B$. The Ta atom almost behaves as a free Ta atom in the center of fullerene without interacting with the cage, as shown in figure 4.1.8-(d). As a result, the Ta atom in the sphere's center is protected from outside influence. The last endohedral structure is W@C_{60} fullerene. Indeed, the W atom has been showing more interesting to be magnetically, figure 4.1.8-(e), by holding all magnetic which is $2m_B$ in triplet state calculation out of a total magnetic moment of $2m_B$. Whereas the total magnetic moment of a free W atom is $2\mu_B$in the triplet state, table 4, the W doping atom behaves like a free W atom in the center of C_{60} fullerene.

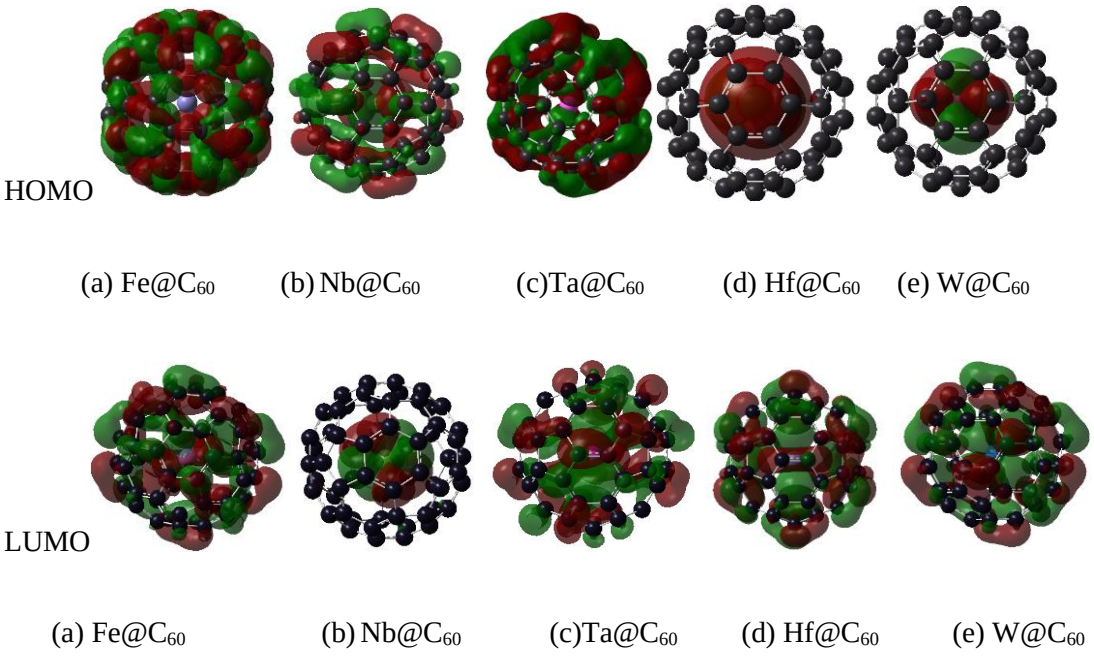

Figure4.1.8: showed the molecular orbital (MO) of HOMO (the highest occupied molecular orbital), lowest unoccupied molecular orbital (LUMO) snapshot of C_{60} M@C_{60} fullerene; where M= (Fe, Nb, Hf, Ta, and W)

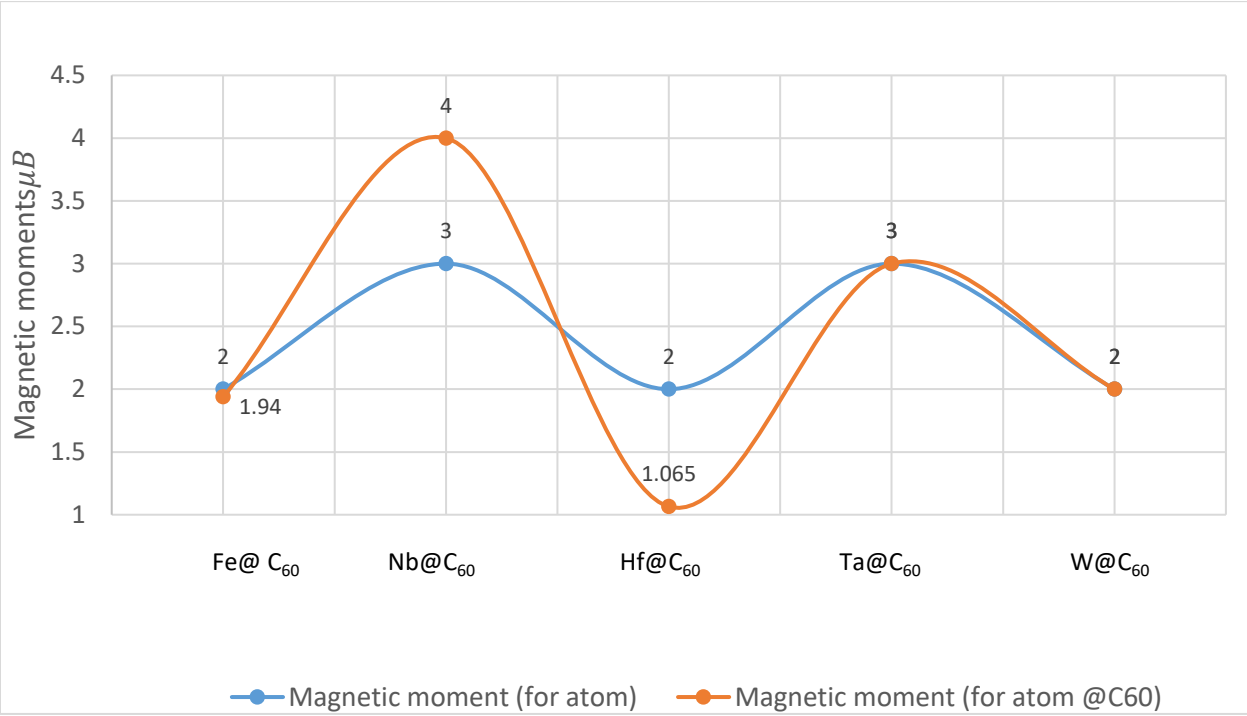

Figure 4.1.9 this is the magnetic moment figure where the blue line represents the magnetic moment. For free atom and the orang line represent the magnetic moments of doped atoms of transition metal atoms at C_{60} fullerene.

4.1.2-2 Endohedral Doping of Transition Metal Atoms at $Si_{30}C_{30}$:

4.1.2-2 -A Single Atom Doping:

This section will show the magnetic properties of Endohedral doping of Transition Metal Atoms in $Si_{30}C_{30}$, a sphere structure with 78 S-C bonds. We start with the first structure sphere-Fe. The Fe atom in the center of the sphere structure retains a high value of the magnetic moment of 4.00 μ_B.Whereas a free Fe atom's spin multiplicity is in a triplet state. So, here also, the cage surface shared magnetic moment with the doped atom Fe.

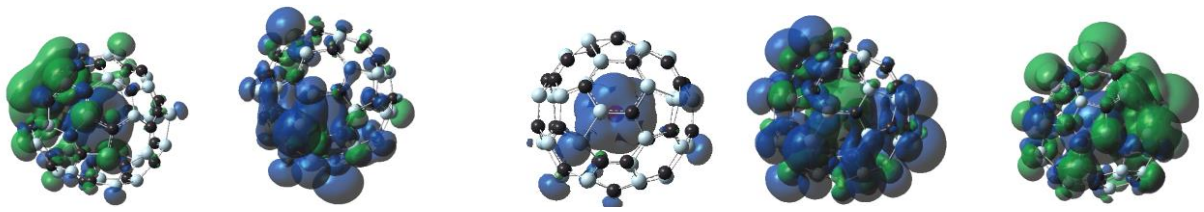

(a) sphere-Fe (b) sphere-Nb (c) sphere-Hf (d) sphere-Ta (e) sphere-W

Figure 4.1.10: showed the total electronic charge density distribution of endohedral doping of transition metals M inside the sphere, Where M= Fe, Nb, Hf, Ta, and W; (a) sphere- Fe. (b) sphere- Nb. (c) sphere- Hf. (d) sphere- Ta. (e) sphere- W

The next structure of our study in this section is sphere-Nb. The magnetic moment of the Nb atom in doublet state is -0.750μ_B out of total magnetic moments, 1μ_B .On the other hand, in the quartets state calculation, the Nb atom had a spin magnetic moment is 1.26 μ_B out of a total magnetic moment of 2 μ_B for a free Nb atom. From the spin density plot in figure 4.1.10-(b). Nb atom shared its magnetic moment with one side of the $Si_{30}C_{30}$ sphere that has a Si-Si bond.

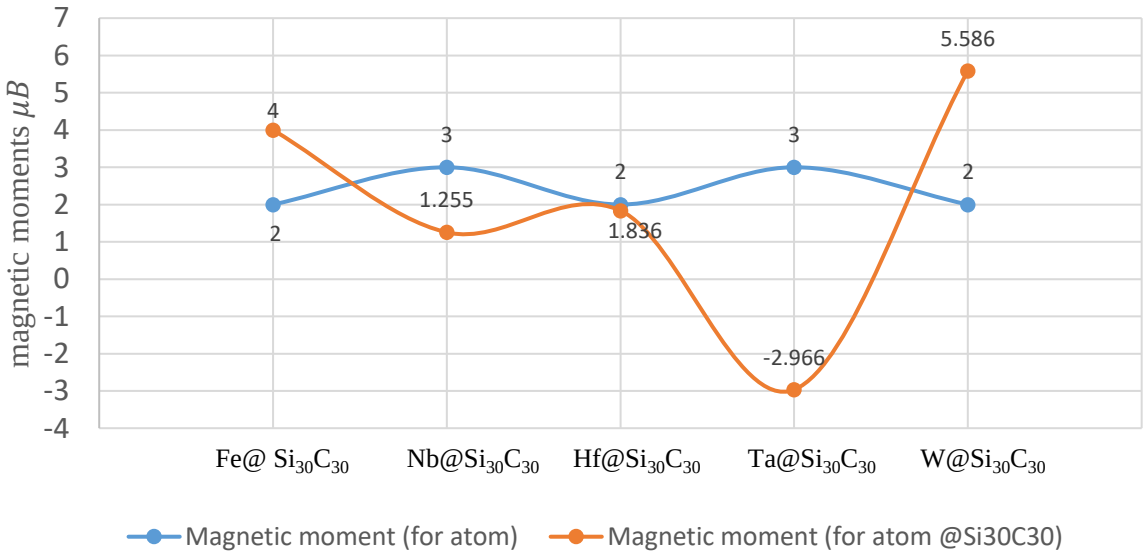

Figure 4.1.11 this is the magnetic moment figure where the blue line represents the magnetic moment. For free atom and the orang line represent the magnetic moments of doped atoms of transition metal atoms at $Si_{30}C_{30}$ fullerene.

The other structure of our study is sphere-Hf. the Hf atom lost a part of its magnetic moment to the cage surface, and the magnetic moment retained by the Hf atom was 1.83 μ_B compared to its free atomic magnetic moment of 2 μ_B, The spin density plot is shown in figure 4.1.10-(c) revealed the magnetic moment distribution over the doped Hf and the sphere cage. The following structure is sphere-Ta. Notably, the Ta atom remains in the center of the cage with a spin magnetic moment of -2.96 μ_B at doublet spin calculation out of its atomic spin magnetic moment state of 1 $\mu_B$as shown in figure 4.1.10(d). The last structure of endohedral doping is sphere-W, where, interestingly, W atoms is found to have a magnetic moment of 5.856 μ_B (see figure 4.1.11). Whereas the total magnetic moment for a free W atom is 2 μ_B, as shown in Table 4. Due to unsaturated Si-C bonds, there is an interaction between surface atoms and doping atom W. As a result, the C_{60} fullerene cage share 3.856 μ_B with W atom gives. The W atom. However, the HOMO of molecular orbital shows the interaction between the doping atom and the structure cage

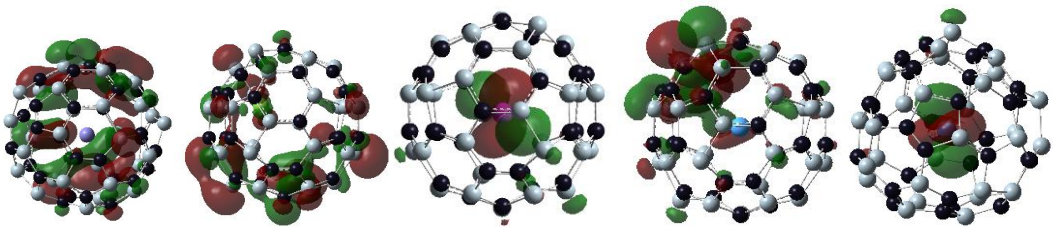

HOMO

(a) sphere-Fe (b) sphere-Nb (c) sphere-Hf (d) sphere-Ta (e) sphere-W

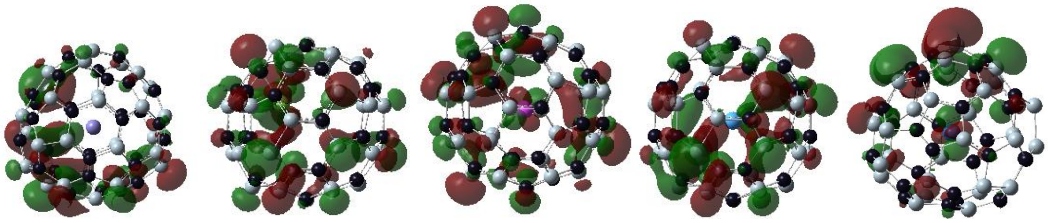

LUMO

(a) sphere-Fe (b) sphere-Nb (c) sphere-Hf (d) sphere-Ta (e) sphere-W

Figure 4.1.12: shows the molecular orbitals (MO) of HOMO, the highest occupied molecular orbital, lowest unoccupied molecular orbital (LUMO) for sphere-M structure; M= Fe, Nb, Hf, Ta, and W.

The result mentions that the Fe atom has 4.00 μ_B where the HOMO-LUMO orbital figures did not show the contribution with the cage of structure. The Alpha energy eigenvalue is -0.19082 eV at HOMO, and -0.15501 eV at LUMO, and the HOMO-LUMO gap is 0.974 eV. Moreover, the Beta energy eigenvalue is-0.1692 eV at HOMO and -0.13120 eV for LUMO, and the HOMO-LUMO gap is 1.034 eV. So, we calculate HOMO-n and LUMO+n to see at what level of energy the Fe atom starts to contribute with the cage; n=4. The contribution between the Fe atom and the cage show at HOMO-4 as shown in Figure 4.1.13.

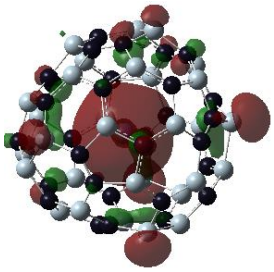

HOMO-Alpha

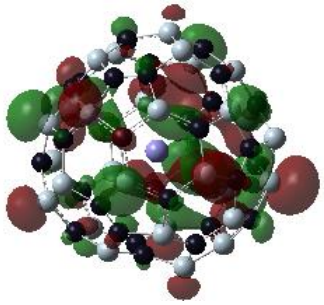

LUMO-Alpha

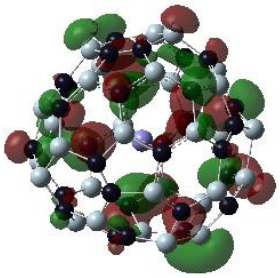

HOMO-Beta

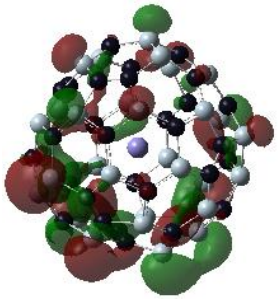

LUMO-Alpha

Figure 4.1.13 showed the HOMO-4 and LUMO+4 for sphere-Fe

4.1.2-2 -B. Dimer-Atom Doping:

While the atoms of 4d and 5d transition metals are not magnetic in bulk, small groups of these atoms, such as dimers, can be magnetic [104]. For example, Ta_2 has a magnetic moment of $4\mu_B$ [102]. The same group of transition metal atoms W, Fe, Ta, Nb, and Hf are chosen here to form

dimers. The first structure of our study in this section is sphere- Fe_2. In the sphere-Fe_2 structure, the triplet state calculation shows the high value of spin magnate moment on one Fe atom 3.886 μ_B and the second one holds -1.195μ_B, as shown in Table 4, out of a total magnetic moment of 2μ_B. This mean sphere-Fe_2 has the value of net magnetic moment is 2.961μ_B. The next structure is the sphere–Nb_2. It showed in triplet state where one atom of the Nb-dimer possesses a high spin magnetic moment of 1.22μ_B, and the other atom hold -0.355 out of all magnetic moments of 2μ_B. This mean Nb_2 has a net magnetic moment of 0.866μ_B.

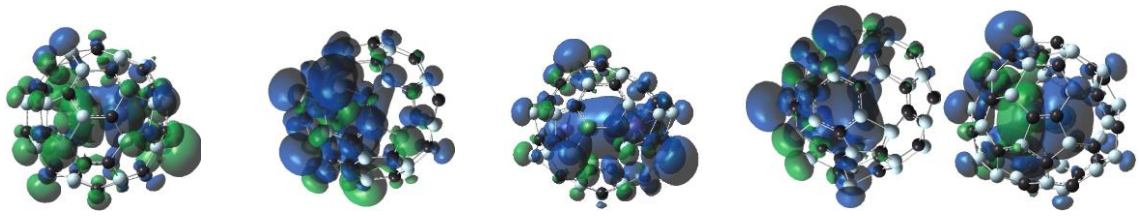

(a) sphere-Fe_2 (b) sphere-Nb_2 (c) sphere-Hf_2 (d) sphere-Ta_2 (e) sphere-W_2

Figure 4.1.14: showed the total electronic charge density distribution of endohedral doping of transition metals M_a inside the sphere, where M= Fe, Nb, Hf, Ta, and W and a= 2.

The following structure is sphere-Ta_2. As a free dimer, Ta_2 has a high value of a magnetic moment, 2μ_B. However, Ta_2 has shown not interesting to be magnetically with the value of 1.037μ_B out of the total magnetic moment of dimer 2μ_B. Where 0.963 μ_B is shared with cage atoms. For sphere-Hf_2 structure, the Hf-dimer in triplet state showed less attractive in the magnetic moment. the magnetic moment value of Hf-dimer is 1.096 μ_B.From the molecular orbitals (MO) of HOMO, the highest occupied molecular orbital, as shown in figure 4.1.14, we see that all dimer doping of transition metal atoms interacts with the cage surface.

The last structure is sphere-W_2. The sphere-W_2 configuration is found to retain a large spin magnetic 3 μ_B moments out of a maximum magnetic moment of W-dimer 2 μ_B, the first W atom holds 2.819 μ_B and the second W atom holds -1.834 μ_B.This mean the W-dimer has a net magnetic moment of 0.985 μ_B.

HOMO

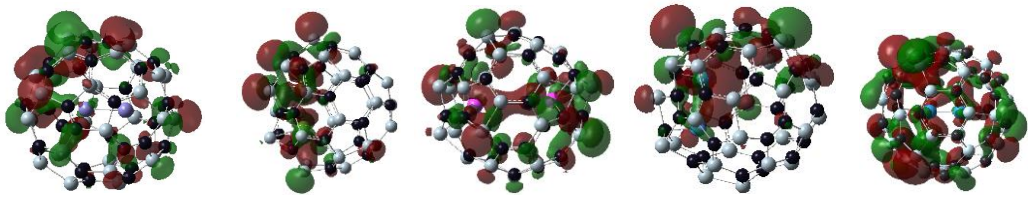

(a) sphere-Fe_2 (b) sphere-Nb_2 (c) sphere-Hf_2 (d) sphere-Ta_2 (e) sphere-W_2

LUMO

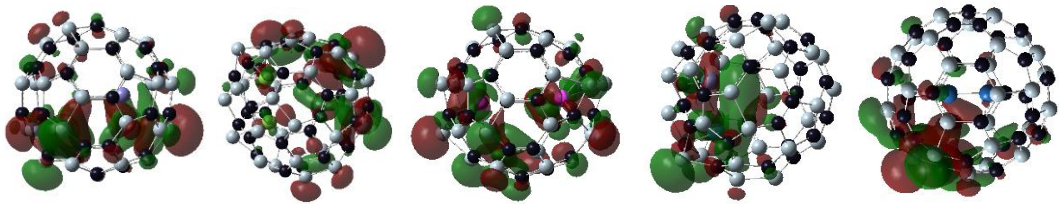

(a) sphere-Fe_2 (b) sphere-Nb_2 (c) sphere-Hf_2 (d) sphere-Ta_2 (e) sphere-W_2

Figure 4.1.15: shows the molecular orbitals (MO) of HOMO, the highest occupied molecular orbital for sphere-M_2 structure; M= Fe, Nb, Hf, Ta, and W.

4.1.3. Endohedral Doping of Transition Metal on C_{70} Fullerene

The second most common fullerene, C_{70} fullerene, and its derivatives have increased interest in a variety of areas, ranging from medicines to materials research. This is because of the binding energy per atom of C_{70} fullerene[57], which is bigger than C_{60}. In addition, carbon fullerene possesses a strong covalent is one of its most interesting characteristics. As a result, fullerene's carbon is saturated, and the cage surface has no unpaired electrons. This indicated that if we add

an atom to the center of fullerene, the cage surface will retain magnetic moments value to the doping atoms. For endohedral doping, transition metal atoms are used because of their valence level structure, which may have a variety of spin configurations. Therefore, our study uses transition metal atoms (Nb, Fe, Hf, Ta, and W) as doping atoms in C_{70} fullerene for electronic and magnetic properties. Figure 4.1.16 shows the relaxed structures for C_{70} endohedral doping atoms of transition metal atoms (Nb, Fe, Hf, Ta, and W). In addition, as atomic sizes getting bigger the stability decreases for C_{70} endohedral doping atoms of transition metal atoms as shown in figure 4.1.17.we

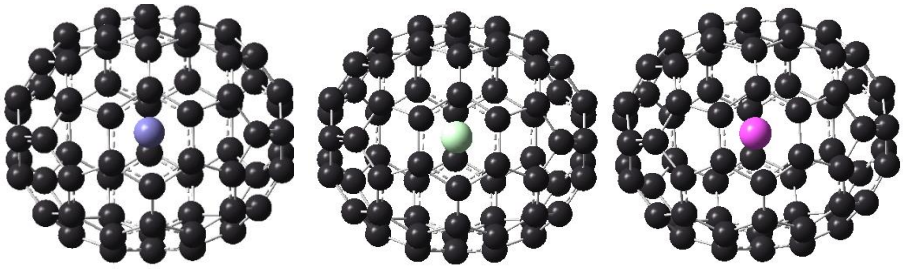

Fe@ C_{70} fullerene Nb @ C_{70} fullerene Hf @ C_{70} fullerene

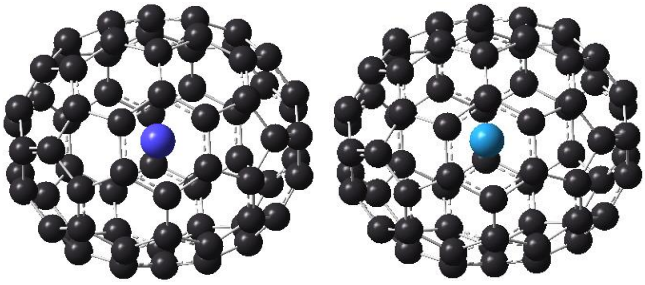

Ta@C_{70} fullerene W@C_{70} fullerene

Figure 4.1.16: shows the relaxed structures for C_{70} fullerene and its endohedral doping of transition metals atom (Nb, Fe, Hf, Ta, and W)

The Fe@C_{70} fullerene is the first structure of C70 endohedral doping. It has a high value of binding energy by 0.101 eV/atom than C_{70} fullerene. On the other hand, the triplet state of Fe@C_{70} fullerene shows a significant value of spin-up HOMO-LUMO gap 2.690 eV. This value of the

HOMO-LUMO gap is 0.007 eV higher than the one in C_{70} fullerene. Also, there is a small change in the double bond length of the structure as the z-axis diameter compared to C_{70} fullerene. Their value is 1.398 Å for the smallest double bond and 7.135 Å for the z-axis diameter

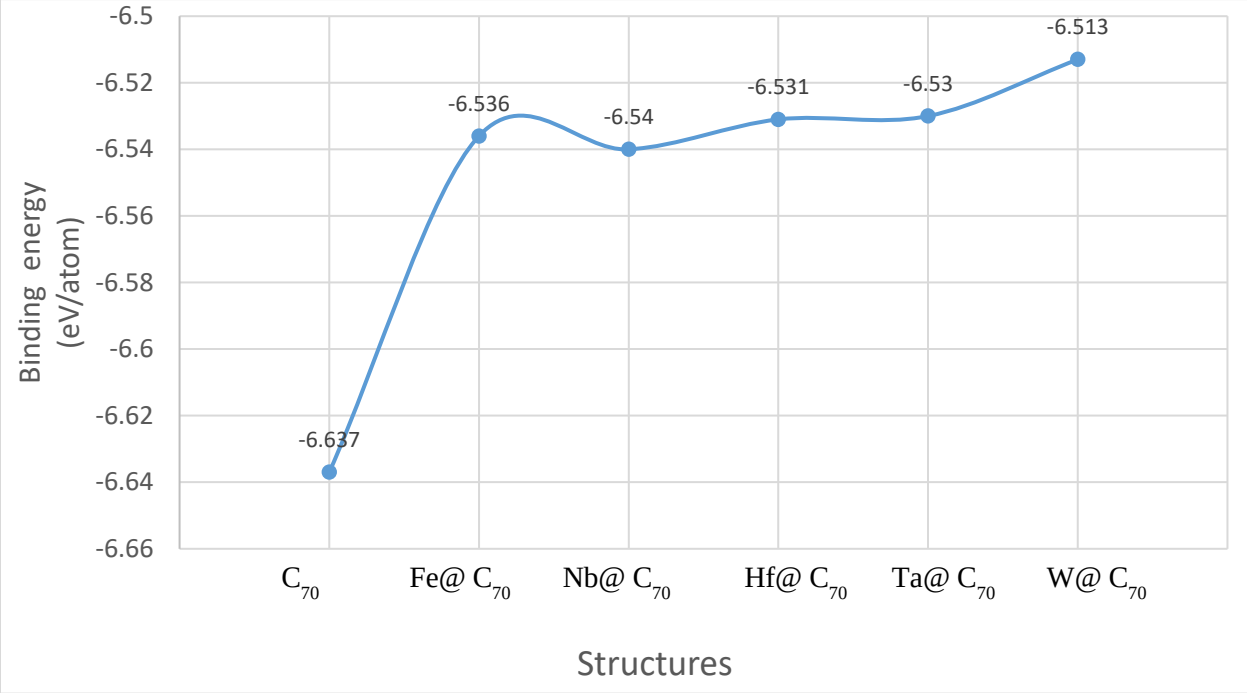

Figure 4.1.17 shows the binding energy for C_{70} fullerene and its endohedrally doped of transition metal atoms

The second stable structure of endohedral doping atoms is Nb@C_{70} fullerene, figure 4.1.16, with interesting electronic properties results. Moreover, it is the most stable structure among other transition metals in this paper, with a value of binding energy -6.540 eV/atom. Also, the spin-up HOMO-LUMO gap of Nb@C_{70} fullerene is 1.705 eV which is a smaller 0.978 eV than C_{70} fullerene. Also, compared to C_{70} fullerene, the structure's double C=C, single C-C, and dimeters have been increased. The values are 1.399Å for the slightest double bond, 1.450 Å for the smallest single bond, and 7.359 Å for diameter in the z-axis.

. The following structure of endohedral doping is Hf@C_{70} fullerene. For electronic properties, there is an increase of the smallest C-C double bond, which is 0.004Å longer than the smallest C-C double bond of C_{70} fullerene. Also, Hf@C_{70} fullerene has a small value of HOMO-LUMO gap by 0.983 eV for spin-up among other endohedral structures.

Table 4.1.5: The calculation of binding energy (E_b) (eV/atom), HOMO-LUMO gap (E_g (eV)), and multiplicity (Mu). Diameter (D), (Å) single and double bonds (Å) (B_s and B_d).

M@c70	Eb(eV/atom)	HOMO-LUMO gaps(eV)	Smallest double bonds (Å)	Average double bonds(Å)	Smallest single bond(Å)	Average single bond(Å)	Diameter (z-axis) (Å)	Diameter (x-axis) (Å)	Multiplicity
C_{70}	-6.637	2.683	1.397	1.421	1.458	1.458	7.132	8.335	Singlet
Fe@ C_{70}	-6.536	2.690 1.148	1.398	1.429	1.458	1.462	7.135	8.335	Triplet
Nb @ C_{70}	-6.540	1.705 0.761	1.399	1.416	1.450	1.459	7.359	8.335	Quartet
Hf @ C_{70}	-6.531	0.983 1.597	1.401	1.421	1.458	1.462	7.133	8.335	Triplet
Ta @ C_{70}	-6.530	1.574 1.329	1.399	1.425	1.458	1.459	7.143	8.328	Quartet
W @ C_{70}	-6.513	2.023 1.631	1.398	1.424	1.458	1.460	7.371	8.330	Triplet

The following structures are Ta@C_{70} fullerene and W@C_{70} fullerene. For stability, The Ta@C_{70} fullerene is slightly more stable by the value of binding energy 0.0177 eV/atom than the W@C_{70} fullerene. In the Ta@C_{70} fullerene, there is a slight change on double C=C bonds 0.002 Å higher than the double C=C bond on C_{70} fullerene. However, the W@C_{70} fullerene has just 0.001 Å higher than the double C=C bond on C_{70} fullerene. For diameters, booth the z-axis diameter is and x-axis

diameters of Ta@C_{70} and W@C_{70} fullerenes are longer than $C_{70}$the which are 7.143 Å and 7.371 Å for z-axis and 8.328 and 8.330 for the x-axis.

4.1.4. Endohedral Doping of Transition Metal on $Si_{35}C_{35}$ Fullerene

Endohedral fullerene has flexible and controllable electronic, optical, and magnetic characteristics, which are connected with the nature of the enclosed species. The endohedral doping of C_{70}@fullerenes is a wide class of fullerene derivatives[97][35]. So, replacing 35 C-atoms with 35 Si-atoms, $Si_{35}C_{35}$ segregated fullerene is made with a maximum number of Si-C bonds, 92 bonds, and minimum Si-Si and C-C bonds, 7 bonds. Our result shows that how the strong Si-C bond is because the more Si-C bonds in the structure, the ellipsoid shape we will get, as shown in figure 3.1.1(e). As a result, The $Si_{35}C_{35}$ fullerene is wider than C_{70} fullerene by 2.477 Å in x-axis (major axis) and 2.002 Å in z-axis (minor axis). Where the $Si_{35}C_{35}$ average diameters are 10.812 Å for x-axis and 9.134 Å for z-axis. Also, the average bonds of Si-Si, C-C, and Si-C are 2.318Å, 1.416Å, and 1.845Å. Moreover, $Si_{35}C_{35}$ fullerene has a value of binding energy and HOMO-LUMO gaps are -4.592eV/atom and 1.813 eV. Where also, endohedral doping of $Si_{35}C_{35}$ fullerene is a class of fullerene derivatives.

The $Si_{35}C_{35}$ fullerene has a larger inner space due to wider diameters. This encourages us to investigate endohedral doping of the transition metal atoms (Nb, Fe, Hf, Ta, and W). Figure 4.1.18 shows the relaxed structures for Si_{35} C_{35} fullerene and its endohedral doping of transition metals atoms (Nb, Fe, Hf, Ta, and W). In addition, as atomic sizes getting bigger the stability increases for $Si_{35}C_3$ endohedral doping atoms of transition metal atoms as shown in figure 4.1.19. The first structure is Fe@ $Si_{35}C_{35}$. The triplet spin state calculation is more stable than the singlet state calculations, with binding energies of -4.710 eV/atom and -4. 670 eV/atom, respectively. The HOMO-LUMO gap in triplet state is 1.871 eV which is 0.058 eV large than $Si_{35}C_{35}$. Also, the C-

C average bonds length increased to 1.446 Å compared to $Si_{35}C_{35}$ C-C average bonds. On the other hand, the diameters, Si-Si, and Si-C average bonds decrease. Their values are 10.674 for the x-axis and 8.892 for the z-axis, 2.276 for Si-Si, and 1.832 for C-C.

(a) Fe@$Si_{35}C_{35}$ fullerene (b) Nb@$Si_{35}C_{35}$ fullerene (c) Hf@$Si_{35}C_{35}$ fullerene

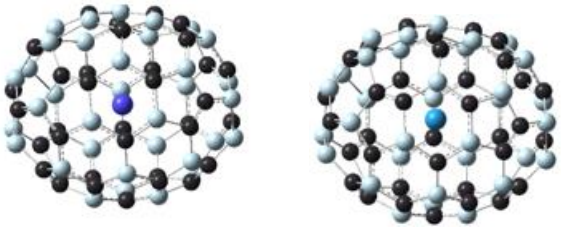

(d) Ta@$Si_{35}C_{35}$ fullerene (e) W@$Si_{35}C_{35}$ fullerene

Figure 4.1.18: shows the relaxed structures for Si_{35} C_{35} fullerene and its endohedral doping of transition metals atoms (Fe, Nb, Hf, Ta, and W)

The second structure of endohedral doping is Nb@ $Si_{35}C_{35}$. This structure is the most stable structure by holding the lowest value of binding energy is -4.713 eV/atom, and the spin-up of HOMO-LUMO gap is 1.668 eV. On the other hand, the structure diameter decreases compare to $Si_{35}C_{35}$ as well as Si-Si and Si-C bonds, which are 10.640 Å for the x-axis, 8.895 Å for the z-axis, 2.281 Å for Si-Si average bond, and 1.821 Å for Si-C bonds. However, the C-C bond length increased with a value of 1.447 Å. This means there are no more C=C double bonds on the relaxed Nb@ $Si_{35}C_{35}$ structure.

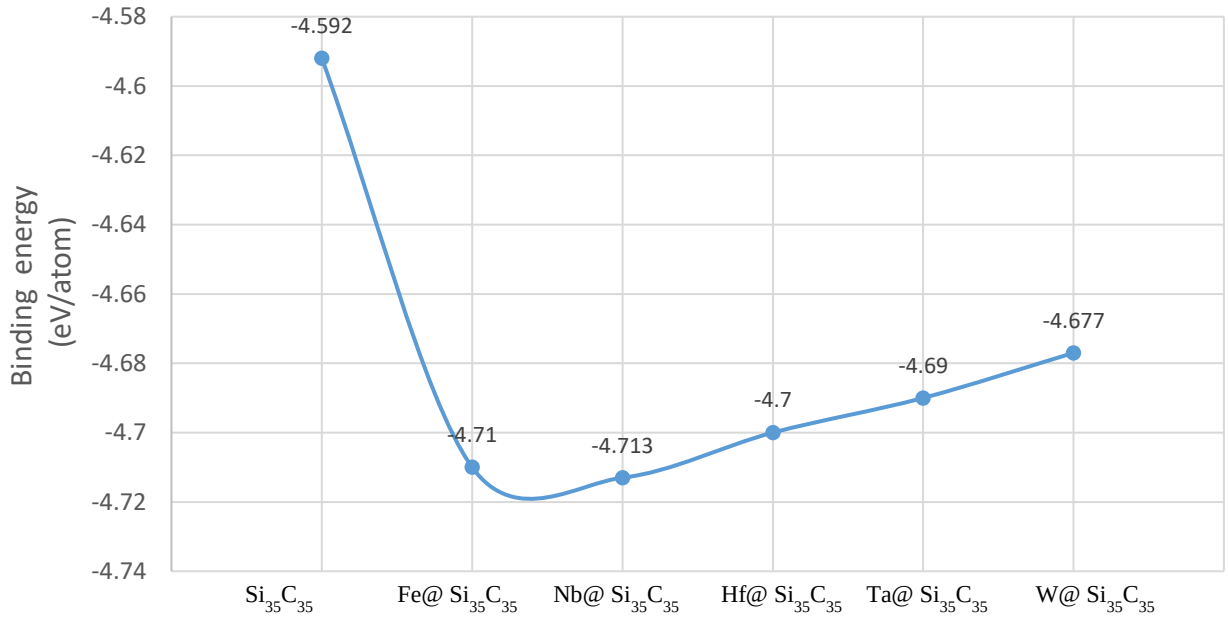

Figure 4.1.19 shows the binding energy for $Si_{35}C_{35}$ endohedral doping atoms of transition metal atoms.

The following structure is Hf@ $Si_{35}C_{35}$. Table 2 shows that the triplet spin state calculation of Hf@ $Si_{35}C_{35}$fullerenes is more stable than the singlet state calculations, with binding energies of -4.700 eV/atom for triplet state, -4.687 eV/atom for singlet state, respectively. As a result, the HOMO-LUMO gap of spin-up is 0.985 eV for the triplet state, which is 0.196 eV higher than the singlet HOMO-LUMO gap value. Furthermore, we can see here the same trend as Hf@ $Si_{35}C_{35}$ and Hf@ $Si_{35}C_{35}$ for increasing the average bond length of the C-C bond by a value of 1.447 Å in singlet 1.445 Å in the triplet state, as shown in Table 4.1.6. The diameters are 10.638 Å for the x-axis and 8.893 Å for the z-axis in the triplet state calculation.

Table 4.1.6: The calculation of binding energy (E_b) (eV/atom), HOMO-LUMO gap (E_g(eV)), Multiplicity (Mu).

M@$Si_{35}C_{35}$	Eb(eV/atom)	HOMO-LUMO gaps(eV)	Average D(x-axis) (Å)	Average D(z-axis) (Å)	Average C-C Bonds (Å)	Average Si-Si Bonds (Å)	Average Si-C Bonds (Å)	Multiplicity
$Si_{35}C_{35}$	-4.592	1.813	10.812	9.134	1.416	2.318	1.845	singlet
Fe@$Si_{35}C_{35}$	-4.670	1.541	10.674	8.900	1.446	2.276	1.823	singlet
Fe@$Si_{35}C_{35}$	-4.710	1.871 1.044	10.674	8.892	1.446	2.276	1.823	triplet
Nb@$Si_{35}C_{35}$-	-4.713	1.668 1.214	10.640	8.895	1.447	2.281	1.821	quartet
Hf@$Si_{35}C_{35}$	-4.687	0.789	10.678	8.878	1.447	2.277	1.825	singlet
Hf@$Si_{35}C_{35}$	-4.700	0.985 1.743	10.638	8.893	1.445	2.274	1.823	triplet
Ta@$Si_{35}C_{35}$	-4.690	1.714 1.469	10.775	8.936	1.447	2.273	1.813	Double
Ta@$Si_{35}C_{35}$	-4.687	1.870 1.850	10.656	8.895	1.446	2.281	1.833	quartet
W@$Si_{35}C_{35}$	-4.677	1.862	10.657	8.893	1.446	2.276	1.804	singlet
W@$Si_{35}C_{35}$	-4.667	1.706 1.864	10.775	8.893	1.446	2.278	1.810	triplet

The doublet state of Ta@$Si_{35}C_{35}$ has the lower binding energy is -4690 eV/atom, where the singlet state has a -4.690 eV/atom value of binding energy. However, the spin-up of the HOMO-LUMO gap of the quartet state is higher than the doublet, which is 1.870 eV. Also, the diameter is 10.774 Å for the x-axis and 8.895 Å for the z-axis, where the average of Si-Si and Si-C are 2.273 Å and 1.813 Å. Thus, the final structure is W@$Si_{35}C_{35}$ which the singlet state is more stable than the triplet state by value of -4.677eV/atom. The diameter of the triplet state is 10.775 Å for the x-

axis, which is 0.118 Å longer than the singlet and the same value as singlet 8.893 Å for the z-axis. On the other hand, the singlet state calculation has a lower average value of Si-Si and Si-C than the triplet state with 2.276 Å and 1.804 Å.

The HOMO-LUMO gaps values for endohedral doping of transition metal atoms (Nb, Fe, Hf, Ta, and W) oscillate between 0.789 and 1.870 eV. Where a low value of 0.789 eV for the singlet spin state calculation of $Hf@Si_{35}C_{35}$ fullerenes and a higher value of 1.870 eV for the quartet spin state calculation of $Ta@Si_{35}C_{35}$ fullerenes. In addition, all endohedral doping shows that there are no double C=C bonds in their structure. Notify, figure 4.1.20 shows that the higher Si-Si and Si-C bonds, the lower energy will get.

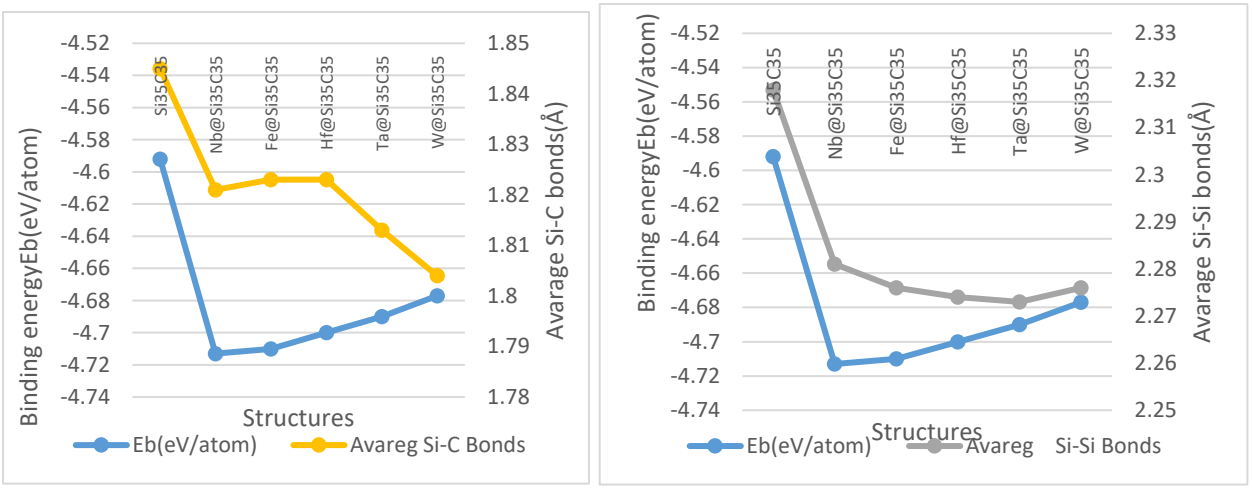

(a) (b)

Figure 4.1.20: shows the binding energy VS average Si-C bond in figure (a) and binding energy VS average Si-Si bond in figure (b).

4.1.5. Magnetic Properties of Endohedral Doping:

4.1.5-1. Endohedral Doping of C_{70}Fullerene:

This section will study the magnetic properties of endohedral doping of transition metal atoms

(Fe, Nb, Hf, Ta, and W)

Figure-4.1.21 shows the magnetic moment structures of M@ C_{70} fullerene, where M= Fe, Nb, Hf, Ta, and W. The first structure is Fe@ C_{70} fullerene. Here, the Fe atom is not interacting with the cage, as shown in figure 4.1.23. Instead, the magnetic moment's graph, figure 4.1.21-(a), shows that the cage surface atoms retain the magnetic moment to the doping atom. It holds almost all magnetic moments of the system is $2.03\mu_B$, while as a free atom, its magnetic moment is 2 μ_B as shown in figure 4.1.22. As a result, the Fe atom is behaver as a free electron in the center of the cage. So, the Fe could be protected from outside influence.

The Nb@C_{70} is the second structure of our study in this section. Magnetically, the Nb atom, in quartet state shows a high value of magnetic moment is $4.008\mu_B$ even though Nb at a distance of 3.7Å and 4 Å in the x-axis and z-axis of the cage. According to that, we can say the Nb atom is interacting with the cage surface atoms (carbon). Moreover, the HOMO (the highest occupied molecular orbital) molecular orbital (MO) shows the interaction between the cage surface atoms and doping Nb atom. As a result, the cage atoms share their magnetic moment with the Nb atom.

The following structure of our study in this section is Hf@C_{70} fullerene. The MO-HOMO graph of Hf@C_{70} fullerene shows the interaction between the Hf atom and the cage surface, as shown in figure 4.1.23-(c). As a result, the Hf atom shares its magnetic moment with the fullerene surface atoms. The cage of fullerene retains 1.684 $\mu_B$of magnetic moments to the Hf atom and keep $0.316\mu_B$.

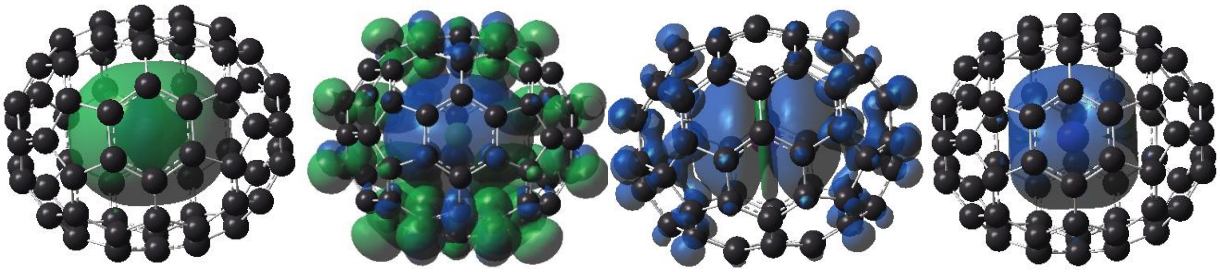

(a) Fe@C_{70} fullerene (b) Nb@C_{70} fullerene (c) Hf@C_{70} fullerene (d) Ta@ C_{70} fullerene

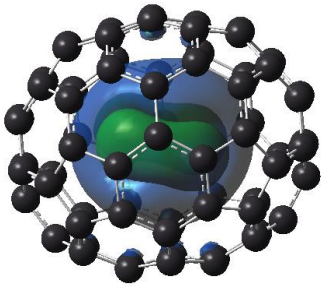

(e) W@C_{70} fullerene

Figure 4.1.21: showed the total electronic charge density (magnetic moment) structures of M@ C_{70} fullerene, where M= Nb, Hf, 0Fe, Ta, and W. The green cooler represents the negative value of magnetic moments, and the blue cooler represents the positive value of magnetic moments.

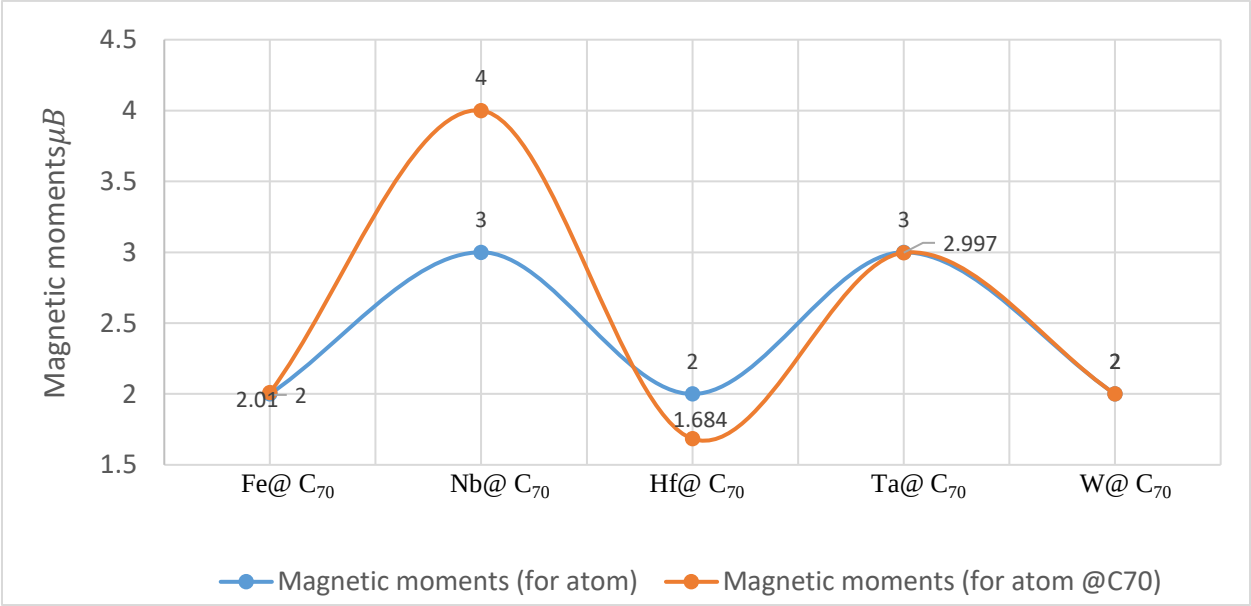

Figure 4.1.22. This is the magnetic moment figure where the blue line represents the magnetic moment for free atom and the orang line represent the magnetic moments of doped atoms of transition metal atoms at C_{70} fullerene. Where 1 represent doublet state, 2 represent triplet state, and 3 represent quartet state and so on.

The last two structures of endohedral doping of transition metals @ C_{70} fullerene are Ta@C_{70} fullerene and W@C_{70} fullerene. Figures 4.1.21- (d) and (e) show how the doping atom hold all spin magnetic moment of their systems. So, Ta and W atoms show more interesting to be magnetically by holding almost all magnetic moments $2.99\mu_B$ and $2.004\mu_B$ out of total magnetic moments, $3.00\mu_B \; and \; 2.00\mu_B$. While as free atoms Ta and W, their magnetic moment are 3 μ_B and $2.00\mu_B$. In addition, Figures 1.1.23- (d) and (e) of MO-HOMO show the Ta and W keep in the center of the cage without interacting with their cage surface.

HOMO

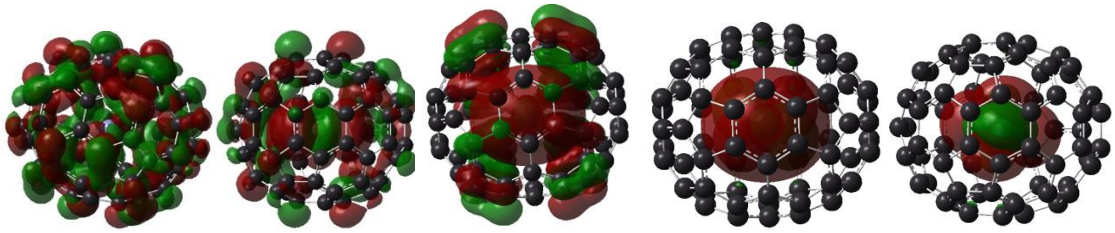

(a) Fe@ C_{70} (b) Nb@C_{70} (c) Hf@C_{70} (d) Ta@ C_{70} (e)W@C_{70}

LUMO

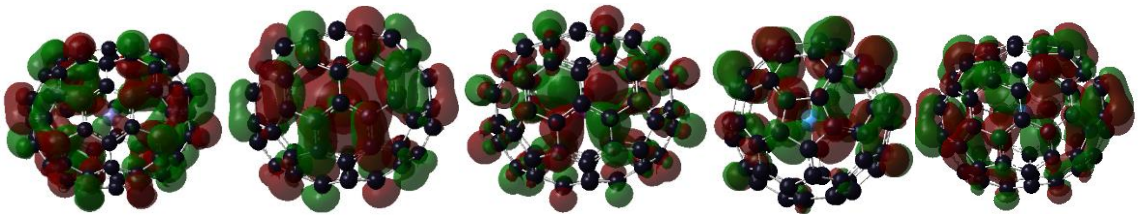

(a) Fe@ C_{70} (b) Nb@C_{70} (c) Hf@C_{70} (d) Ta@ C_{70} (e)W@C_{70}

Figure 4.1.23: shows the molecular orbitals (MO) of HOMO, the highest occupied molecular orbital, lowest unoccupied molecular orbital (LUMO) for M@C_{70} fullerene structure; M= Fe, Nb, Hf, Ta, and W.

4.1.6. Endohedral Doping of $Si_{35}C_{35}$Fullerene:

In the $Si_{35}C_{35}$ Fullerene, there is the maximum number of the Si-C bond, which is 92 bonds. Due to long Si-C bonds compare to C-C bonds, our structure will be larger than C_{70} fullerene. It is expected that if we add an atom in the center of $Si_{35}C_{35}$ Fullerene, the doping atom will be far enough from the cage surface. As a result, the doping atom will act as a free atom without interacting with the cage. So, the cage could retain the magnetic moment to its doping atom. Based on that, we start our investigation by adding transition metal atoms (Nb, Fe, Hf Ta, and W) in the center of $Si_{35}C_{35}$ Fullerene. Figure 4.1.24 shows the spin magnetic moment for endohedral doping of transition metal atoms in the center of $Si_{35}C_{35}$ Fullerene.

The first structure of the study in this section is Fe@$Si_{35}C_{35}$. While as a free Hf atom, its magnetic moment is $2\mu_B$, the doping Fe atom has a value of magnetic moment $2.03\mu_B$. In addition, figure 4.1.24-(a) shows no interaction between the Fe atom and the cage surface, where the MO-HOMO shows only on the cage atoms. As a result, the cage surface retains the magnetic moment to the Fe atom, and the Fe could be protected from outside influence. The following endohedral doping structure is Nb@ $Si_{35}C_{35}$. The Nb atom has shown to be more interesting by holding all magnetic moments 2.99 μ_B out of the total magnetic moment of the system, $3\mu_B$. Another structure of endodermal doping is Hf@ $Si_{35}C_{35}$ Fullerene. The spin magnetic moment of the Hf atom is 1.95 μ_B of the triplet state. However, the surface of the Hf@$Si_{35}C_{35}$ fullerenes share 0.05 μ_B with the Hf doping atom. While as a free Hf atom, its magnetic moment is 2 μ_B , as shown in figure 4.1.24.

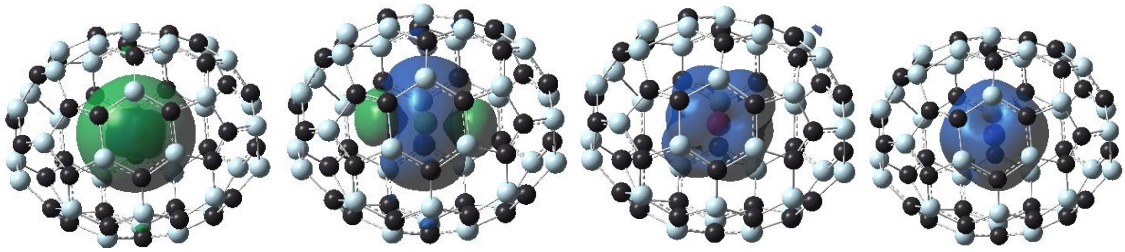

(a) Fe@$Si_{35}C_{35}$ (b) Nb@$Si_{35}C_{35}$ (c) Hf@$Si_{35}C_{35}$ (d) Ta@$Si_{35}C_{35}$

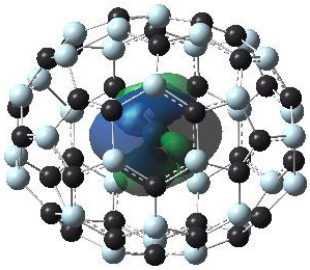

(e) W@$Si_{35}C_{35}$

Figure 4.1.24: showed the total electronic charge density (magnetic moment) structures of M@$Si_{35}C_{35}$ fullerene, where M= Fe, Nb, Hf, Ta, and W. The green cooler represents the negative value of magnetic moments, and the blue cooler represents the positive value of magnetic moments.

The following structure is Ta@$Si_{35}C_{35}$. The spin magnetic moment of the Ta atom at the $Si_{35}C_{35}$ –Ta fullerene is 1 μ_B for doublet spin state calculation and 3μ_B for quartet spin state calculation respectively. The Ta atom remains in the center of the cage after relaxation. It holds all magnetic moments for 2doublet spin state calculations because it is more stable than the quartet state. While as a free Ta atom, its magnetic moment is 1 μ_B as shown in figure 4.1.25.

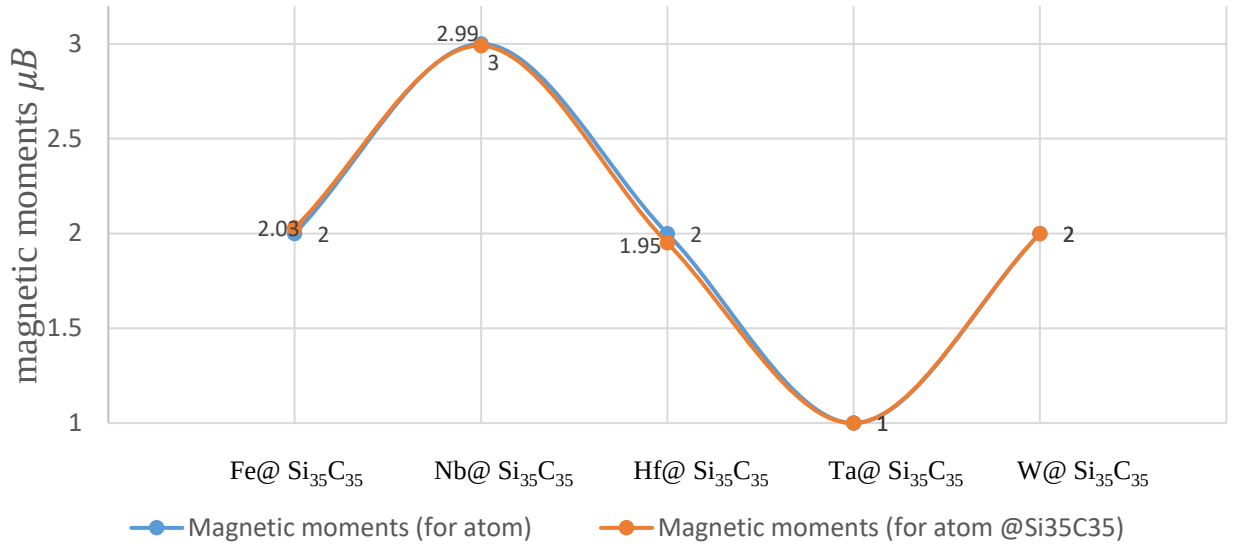

Figure 4.1.25. This is the magnetic moment figure where the blue line represents the magnetic moment for free atom and the orang line represent the magnetic moments of doped atoms of transition metal atoms at $Si_{35}C_{35}$ fullerene. Where 1 represent doublet state, 2 represent triplet state, and 3 represent quartet state.

W@$Si_{35}C_{35}$ Fullerene is the last structure of transition metal atoms in this study. In the previous study[58][32], W-atom shows more interestingly magnetically by holding a high magnetic moment value. So, the endohedral doping atom, W-atom, in $Si_{35}C_{35}$ –W fullerene holds all magnetic values. The figure of the spin magnetic moment, figure 4.1.24-(e), hold on to the W atom where the value of the magnetic moment of the system is $2\mu_B$ out of the total magnetic moment, $2\ \mu_B$. While as a free W atom, its magnetic moment is $2\mu_B$, as shown in figure 4.1.25. This means there is no interaction between the W and the cage surface, which is clear to see in the MO-HOMO figure 4.1.26 (e). Thus, we can say that the W-atom can be fully protected from outside influence in this case.

HOMO

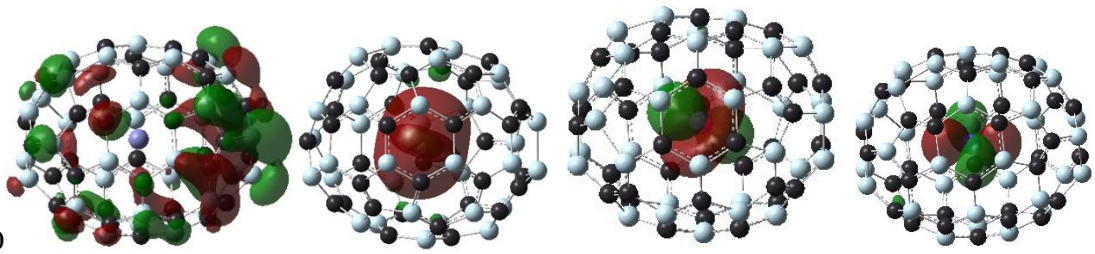

(a) $Fe@Si_{35}C_{35}$ (b) $Nb@Si_{35}C_{35}$ (c) $Hf@Si_{35}C_{35}$ (d) $Ta@Si_{35}C_{35}$

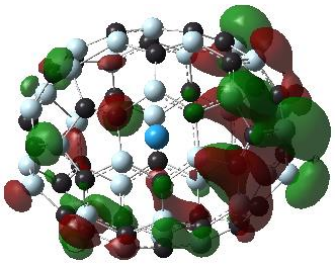

(e)$W@Si_{35}C_{35}$

LUMO

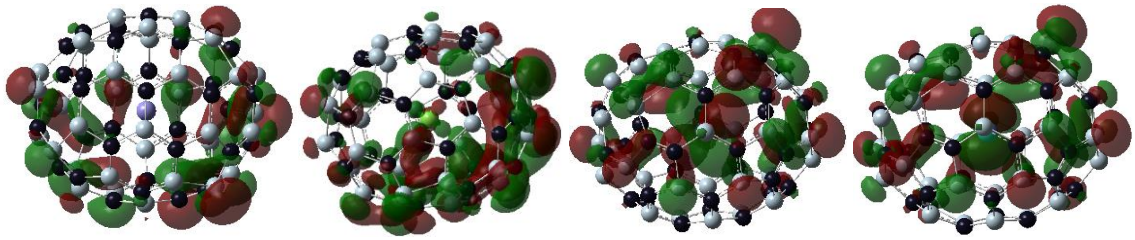

(a) $Fe@Si_{35}C_{35}$ (b) $Nb@Si_{35}C_{35}$ (c) $Hf@Si_{35}C_{35}$ (d) $Ta@Si_{35}C_{35}$

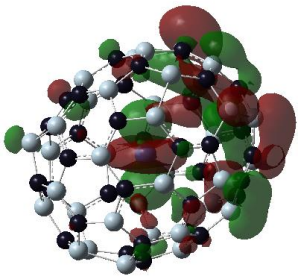

(e)$W@Si_{35}C_{35}$

Figure 4.1.26: shows the molecular orbitals (MO) of HOMO, the highest occupied molecular orbital, lowest unoccupied molecular orbital (LUMO) for $M@Si_{35}C_{35}$ fullerene structure; M= Fe, Nb, Hf, Ta, and W.

Chapter 5

5.1 Endohedral Doping of Rare-Erath Atoms

Rare-earth elements are active metals between metal cations and transition metals[105]. Where their outer valance electron is given as $4f^{0-12}$ $5d^{0-1}$ $6s^2$[106]. In addition, rare-earth atoms can be used in many applications, for example, nickel-metal hydride batteries, plasma displays, fiber optics, lasers, and medical imaging[107]. In addition, the rare-earth atom has been studied its electronic and magnetic properties as doping atoms in C_{60} and C_{70} fullerenes[108][109][70][110][35][73][45].

The following sections will show the electronic and magnetic properties of endohedral doping C_{60}, C_{70}, $Si_{30}C_{30}$, and Si_{35} C_{35} fullerenes of rare-earth atoms (R= La, Ce, Pr, and Nd)).

5.1.1 Computational Method

To analyze the C_{60}, C_{70}, $Si_{30}C_{30}$, and $Si_{35}C_{35}$ endohedral fullerenes of rare-earth atoms (R= La, Ce, Pr, and Nd), we used the density functional theory (DFT), with B3LYP hybrid functional as applied in the Gaussian 09 set of code. The atomic wave functions 6-311G** base set for Si and C atom.

For rare-earth atoms bases set, we calculate the ionization potential (IP) and electron affinity (AE) for rare-earth atoms (R=La, Ce, Pr, and Nd) by using different basis sets. The only one that gets a close value to the experimental IP and EA is the ANO-RCC-VDZP base set. So ANO-RCC-VDZP base set has been used for rare-earth atoms (R=La, Ce, Pr, and Nd). The binding energy in a unit of (eV/atom), the high occupied molecular orbital (HOMO), the lowest occupied orbital (LUMO) in (eV) of unite.

For calculating the binding energy of endohedral doping, we have to follow the following

equations

$$E_b(\mathrm{C}_n\mathrm{R}) = \frac{E(\mathrm{C}_{60}\mathrm{R}) - 60E(\mathrm{C}) - dE(\mathrm{R})}{n+d} \qquad (5.1.1)$$

Equations (5.1.1) represent the equation of binding energy, where $\mathrm{E}(\mathrm{C}_n R)$ is the total energy of relaxed structure and $E(\mathrm{C})\ and\ E(\mathrm{R})$ is the total atomic energy of carbon and doping of rare-earth atoms (R=La, Ce, Pr, and Nd), where n+d= 61 or 71.

For the binding energy of endohedral doping Si_mC_n fullerenes can be calculated by the following equation,

$$E_b(\mathrm{Si}_m\mathrm{C}_n\mathrm{R}) = \frac{E(\mathrm{Si}_n\mathrm{C}_n R) - nE(\mathrm{Si}) - mE(\mathrm{C}) - dE(R)}{m+n+d} \qquad (5.1.2)$$

Equations (5.1.2) represent the equation of binding energy of $\mathrm{Si}_m\mathrm{C}_n\mathrm{R}$ fullerenes. Also, $E(\mathrm{C}), E(Si), E(R)$ and $E(\mathrm{Si}_m\mathrm{C}_n\mathrm{R})$ are total atomic energies of the C, Si, and rare-earth atoms (R=La, Ce, Pr, and Nd) and total energy of relaxed $E(\mathrm{Si}_m\mathrm{C}_n\mathrm{R})$ fullerene. Where m= n= 30 or 35 atoms, and m+n+d= 61, or 71 atoms.

5.1.2 Electronic Properties of Endohedral Doping

5.1.2-A. C_{60} Fullerene

Table 5.1.1 shows lower binding energy for endohedral doping atoms than C_{60} fullerene. So, doping rare-earth atoms at C_{60} helps to decrease the binding energy compared to doping atoms that have been discussed in chapter 4. This means the binding energy increases by doping (Nb, Fe, Hf, Ta, and W) and decreases by doping (La, Ce, Pr, and Nd) at C_{60} fullerene.

In this section, we will show the electronic properties of endohedral doping rare-earth atoms at C_{60} fullerene. As atomic sizes getting bigger for endohedrally doping of rare-earth atoms the

stability increases as shown in figure 5.1.2. The first structure is La@C_{60}. La atom has zero electrons in its f orbital, which is not heavier than another atom (Pr, Ce, and Nd). La@C_{60} has the highest value of binding energy is -6.993 eV/atom. Also, it has a spin-down HOMO-LUMO gap of 2.582 eV. Moreover, it has a 7.078 Å diameter and shortest C-C double bonds of 1.392 Å.

The following structure is Ce@C_{60}, Ce has one electron in 4f orbital also has one electron in 5d orbital, is the second stable structure by has value of binding energy -7.316 eV/atom. On the other hand, the spin-up HOMO-LUMO gaps decrease to 1.185eV compared to C_{60} once as well as bonds length. The diameter of Ce@C_{60} is 0.089Å shorter than the calculated C_{60} diameter and 0.62 Å longer than the experimental C_{60} diameter.

Table 5.1.1: The calculation of binding energy (E_b) (eV/atom), HOMO-LUMO gap (E_g(eV)), diameter (D), shortest single, and double bonds (Å) (b_s and b_d). Average single and double bonds (Å) (bs and bd).

R@C_{60}	E_b (eV/atom)	HOMO-LUMO gaps(eV)	Shortest single bond (Å)	Average Single bonds(Å)	Shortest double bond(Å)	Average Double bond(Å)	Diameter (Å)	Magnetic moments	$M_{ultiplicity}$
C_{60}	-6.601	2.878	1.458	1.458	1.394	1.394	7.149	-------	Singlet
La @C_{60}	-6.993	0.850 2.582	1.437	1.444	1.392	1.392	7.078	2.014	Quartet
Ce@C_{60}	-7.316	1.185 0.833	1.446	1.456	1.392	1.395	7.062	2.989	Triplet
Pr@C_{60}	7.434	2.556	1.445	1.456	1.393	1.396	7.095	3.995	Quartet
Nd@C_{60}	-7.262	2.460 0.840	1.431	1.437	1.393	1.396	7.084	2.997	Triplet

The following structure is Pr@C_{60}. This structure is the most stable structure in our study by having lowest value of binding energy -7.434 eV/atom. Moreover, it shows a big spin-up HOMO-LUMO gap of 2.556 eV. On the other hand, the diameter and C-C bonds length has been decreasing due to heavy doping atoms in the core of the structure

The last structure of the electronic properties study is Nd@$C_{60,}$ as shown in Figure 5.1.1-(d). Nd@C_{60} is the second stable structure by having a -7.262 eV/atom value of binding energy. This value of binding energy is still lower than the calculated binding energy of the C_{60} structure by -0.661 eV/atom. Also, the spin-up HOMO-LUMO gap is 2.460 eV. On the other hand, Nd@C_{60} has the shortest single C-C bond upon other endohedrals doping of rare-earth atoms.

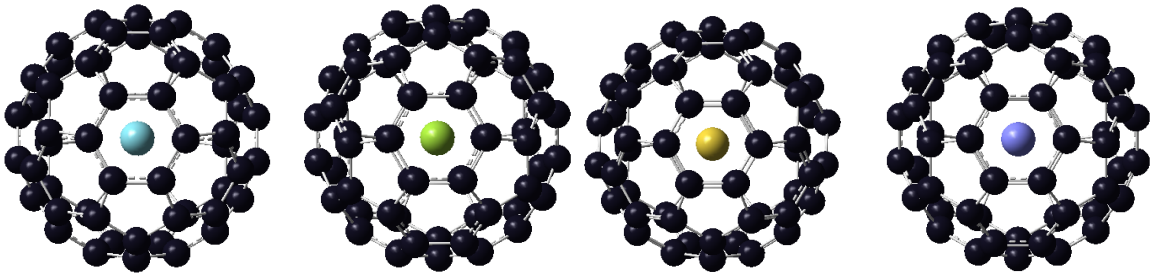

(a) La@C_{60} fullerene (b) Ce@C_{60} fullerene (c) Pr@C_{60} fullerene (d) Nd@C_{60} fullerene

Figure 5.1.1: shows the relaxed structures of endohedral doping of rare-earth atoms (R= La, Ce, Pr, and Nd)

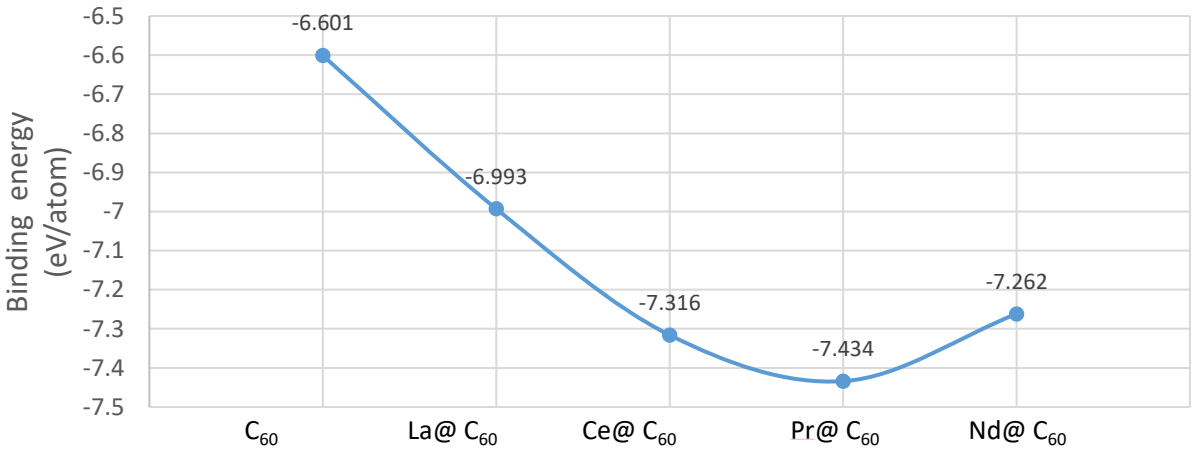

Figure 5.1.2 shows the binding energy (eV/atom) for C_{60} endohedral doping atoms of rare-earth atoms.

5.1.2-B. C_{70} Fullerene

Doping La, Ce, Pr, and Nd atoms in the center of C_{70} help to stabilize the structures as atomic sizes getting bigger, as shown in figure 5.1.4. In addition, La, Ce, Pr, and Nd have the same trend in pulling the cage to the doping atoms by decreasing the diameters. The Nd@C_{70} is the most stable structure by having a lower value of binding energy -7.255 eV/atom, which is lower 0.618 eV/atom than the C_{70} value. Also, it has the second shortest single C-C bonds and second higher spin-up HOMO-LUMO gap of endohedral doping structures 1.447 Å and 2.160 eV. The La@C_{70} is less stable by having -6.991 eV/atom, among other endohedral structures. For spin up HOMO-LUMO gap, it has 1.313 eV and 1.836 eV lower than Nd@C_{70} and C_{70} values. Moreover, it is 0.181 Å longer in z-axis diameter than C_{70}.

Table 5.1.2: The calculation of binding energy (E_b)(eV/atom), HOMO-LUMO gap (E_g(eV)), diameters(D), shortest single, and double bonds (Å). Average single and double bonds (Å).

R@C_{70}	E_b (eV/atom)	HOMO - LUMO gaps (eV)	Shortest Single bonds (Å)	Average Single bonds(Å)	Shortest double bonds(Å)	Average double bonds (Å)	Diameter (Å) x-axis	Diameter (Å) z-axis	EXP-Diameter	$M_{ultiplicity}$
C_{70}	-6.637	2.683	1.458	1.458	1.397	1.421	8.335	7.134	7.906 [56][57]	Singlet
La @C_{70}	-6.991	0.847 2.567	1.450	1.461	1.401	1.420	8.318	7.313		Quartet
Ce@C_{70}	-7.304	1.324 0.902	1.449	1.463	1.387	1.391	8.215	6.990		Triplet
Pr@C_{70}	7.367	2.584 0.664	1.433	1.447	1.384	1.392	8.208	7.081		Quartet
Nd@C_{70}	-7.255	2.160 0.770	1.447	1.457	1.389	1.392	8.294	7.085		Triplet

The Pr@ C_{70} is the second stubble structure by the value of binding energy -7.367, and the spin-up HOMO-LUMO gap is 2.584eV. This spin-up HOMO-LUMO is the highest gap upon our endohedral doping of rare-earth atoms. In addition, the Pr@C_{70} structure has the smallest C-C single, double bonds, and diameters on the x-axis which are 1.433 Å, 1.384 Å, and 8.208 Å. The Ce@C_{70} has the shortest diameters as same as double bonds, as shown in Table 5.1.2. Where its value of binding energy and spin-up HOMO-LUMO gap is -7.304 eV/atom and 1.324 eV, note, La, Ce, Pr, and Nd have some significant changes in electron properties compared to C_{70} fullerene: (i) make the structures more stabilized. (ii) Decreases diameters and bonds lengths of structures.

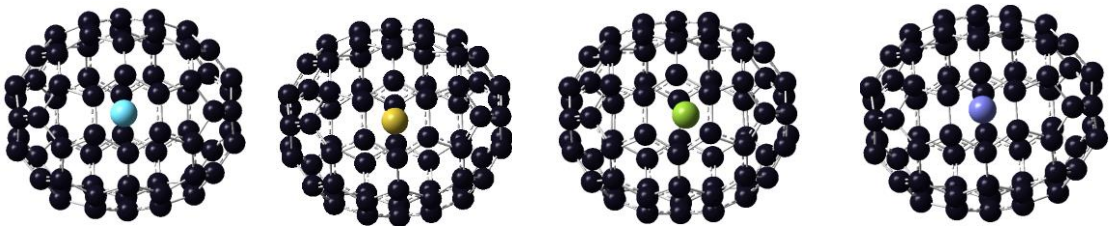

(a) La@C_{70} fullerene (b) Ce@C_{70} fullerene (c) Pr@C_{70} fullerene (d) Nd@C_{70} fullerene

Figure 5.1.3: shows the relaxed structures of C_{70} endohedral doping of rare-earth atoms (R= La, Ce, Pr, and Nd)

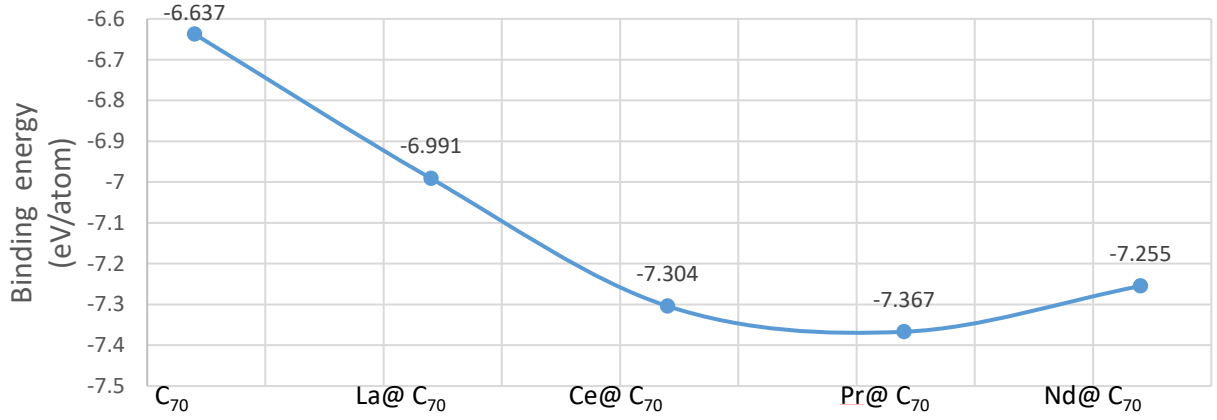

Figure 5.1.4 shows the binding energy (eV/atom) for C_{70} endohedral doping atoms of rare-earth atoms

5.1.2-C. $Si_{30}C_{30}$ Fullerene (Sphere Structure)

Endohedral doping of La atom in the icosahedral Si20 stabilized the structure. It is the perfect silicon cage, similar to the C_{60} fullerene, and the biggest that can be stabilized by a rare-earth R atom[111][112]. The electronic and magnetic properties of endohedral doping of rare-earth atoms (La, Ce, Pr, and Nd) are going to be investigated for the first time in the center of $Si_{30}C_{30}$ fullerene (sphere structure). Note, here $Si_{30}C_{30}$ is the sphere structure that has 78 Si-C bonds, and it is discussed in Chapter 3. Table 5.1.3 shows the values of binding energy (eV/atom), HOMO-LUMO gaps (eV), an average of C-C, Si-Si, and Si-C bonds length, and diameters (Å). Figure 5.1.5 shows the relaxed structure of endohedral doping of rare-earth atoms. In addition, the stability increases at $Si_{30}C_{30}$ endohedrals doped of rare-earth atoms as shown in figure 5.1.6. The La@ $Si_{30}C_{30}$ is the first structure of our investigation, as shown in figure 5.1.5-(a). This structure has the highest value of binding energy, which is 0.524 eV/atom higher than the Nd@Si30C30 value. In addition, the La@ $Si_{30}C_{30}$0 structure has longer diameters by 0.228 Å than most stable structures and 0.051 shorter than Si30C30 (sphere) diameters.

The Ce@$Si_{30}C_{30}$ structure is the next endohedral structure, as shown in figure 5.1.5. Where the Ce@$Si_{30}C_{30}$ structure has a lower value of spin-up HOMO-LUMO gap and shortest average Si-Si, Si-C, and diameters which are 0.800eV, 2.252 Å, 1.792 Å, and 8.608 Å, as shown in Table 5.1.3. The triplet state is a stable structure because it has a lower binding energy -5.543 eV/atom. The Ce atom is bonded with Si atom in hexagon face which the Ce-Si bond length is around 3 Å.

Table 5.1.3: The calculation of binding energy (E_b) (eV/atom), HOMO-LUMO gap (E_g (eV)), and diameter (D), average of C-C, Si-Si, Si-C bonds length, and Diameter Å. For R@$Si_{30}C_{30}$

R@$Si_{30}C_{30}$	E_b(eV/atom)	HOMO-LUMO gaps (eV)	Average C-C bonds(Å)	Average Si-Si bonds(Å)	Average Si-C bonds(Å)	Average Diameters (Å)	Multiplicity
$Si_{30}C_{30}$ (sphere)	-4.712	1.524	1.40	2.26	1.750	8.94	Singlet
La@$Si_{30}C_{30}$	-5.248	1.336 1.933	1.423	2.286	1.816	8.889	Quartet
Ce @$Si_{30}C_{30}$	-5.543	0.800 1.035	1.432	2.252	1.792	8.608	Triplet
Pr @$Si_{30}C_{30}$	-5.673	1.210 0.781	1.417	2.302	1.797	8.685	Quartet
Nd @$Si_{30}C_{30}$	5.775	1.132 0.928	1.408	2.292	1.795	8.661	Triplet

Following structure is Pr@ $Si_{30}C_{30,}$ as shown in figure 5.1.5-(b). The quartet spin state calculation shows the lower value of binding energy which is -5.673 eV/atom, and the HOMO-LUMO gap is 1.210 eV for spin-up. The Pr atom is still inside the cage without any bond with the cage. In addition, the Pr@ $Si_{30}C_{30}$ has a value of average Si-Si bonds length is 2.302 Å, which is a longer value of Si-Si bond length among other structures in this section.

The last structure is Nd@ $Si_{30}C_{30}$ of our investigation. The triplet spin state calculation shows the lowest value of binding energy is -5.775 eV/atom. The structure has the smallest value of average C-C double bonds and average diameters, which are 1.408 Å and 8.66 Å. In addition, the spin-up HOMO-LUMO gaps value is 1.132 eV.

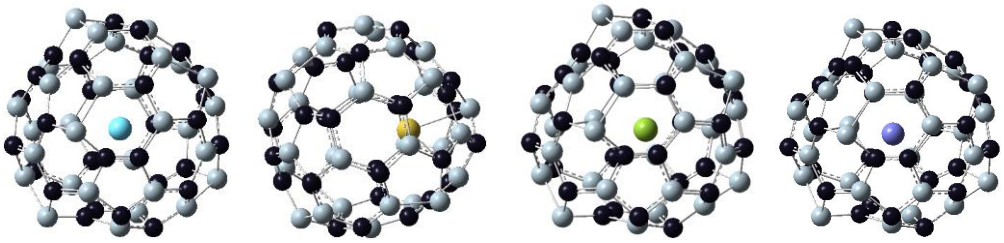

(a) La@$Si_{30}C_{30}$ (b) Ce@$Si_{30}C_{30}$ (c) Pr@$Si_{30}C_{30}$ (d) Nd@$Si_{30}C_{30}$

Figure 5.1.5: shows the relaxed structures R@ $Si_{30}C_{30}$ fullerene structure; R= La, Ce, Pr, and Nd.

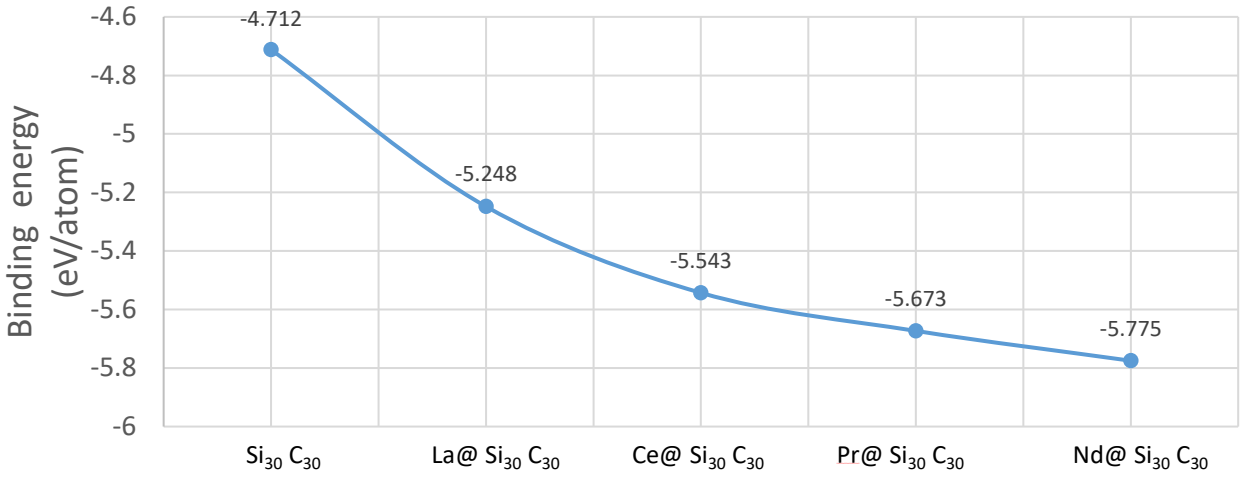

Figure 5.1.6 shows the binding energy (eV/atom) for Si_{30} C_{30} endohedral doping atoms of rare-earth atoms

5.1.2-D. $Si_{35}C_{35}$ Fullerene

It is mentioned in the previous section, adding rare-earth atoms in the $Si_{30}C_3$ fullerene helps the stability as same as $Si_{35}C_{35}$ Fullerene as shown in figure 5.1.8. The rare-earth doping it makes C_{60} more stable in the other hands in the $Si_{35}C_{35}$ doping is making the structure more stable. Where rare-earth atoms doping make the SiC fullerene more stable than transition metal atoms doping. Upon relaxation, all rare-earth atoms remain almost in the center, as shown in figure 5.1.7. In addition, Table 5.1.5 shows the binding energy, HOMO-LUMO gaps, diameters, and C-C, Si-Si, and Si-C average bonds length.

The first structure of endohedral doping is the La@Si35C35 structure. It is a less stable structure by having a high value of binding energy -5.248 eV/atom. On the other hand, La remains almost in the center of fullerene with an average distance to the cage 3.541 Å. In addition, the La@$Si_{35}C_{35}$ has the longer diameters which are 10.653 Å on the z-axis and 8.713 Å on the x-axis compared to other endohedral doping structures in this section. Moreover, it has a longer average Si-C bonds length and lowest spin-up HOMO-LUMO gap of 1.851Å and 0.981eV.

The Ce@ $Si_{35}C_{35}$ structure is the following structure, as shown in figure 5.1.7. It has a value of binding energy -5.441 eV/atom; also, it has the longest diameter on the x-axis which is 10.898 Å. Moreover, there is no double C-C bond length as same as La@$Si_{35}C_{35}$ structure. It has a value of spin-up HOMO-LUMO gap of 1.025 Å

Table 5.1.4: Shows the calculation of binding energy (E_b) (eV/atom), HOMO-LUMO gap (E_g(eV)), diameter (D), average of C-C, Si-Si, and Si-C bonds length. Diameter Å for R@$Si_{35}C_{35}$ structure.

R@ $Si_{35}C_{35}$	Eb(eV/ atom)	HOMO -LUMO gaps (eV)	Average C-C bonds(Å)	Smallest Si-Si bonds(Å)	Average Si-C bonds(Å)	Diameter (z-axis)	Diameter (x-axis)	Mu
$Si_{35}C_{35}$	-4.592	1.813	1.416	2.318	1.845	9.134	10.812	singlet
La@ $Si_{35}C_{35}$	-5.248	0.981 1.742	1.438	2.287	1.851	8.713	10.653	Quartet
Ce @ $Si_{35}C_{35}$	-5.441	1.025 0.705	1.441	2.267	1.813	8.657	10.672	Triplet
Pr@ $Si_{35}C_{35}$	-5.574	1.571 1.324	1.456	2.272	1.784	8.640	10.693	Quartet
Nd @ $Si_{35}C_{35}$	-5.841	1.144 1.159	1.408	2.334	1.792	8.652	10.758	Triplet

The Pr@ $Si_{35}C_{35}$ structure has a high value of spin-up HOMO-LUMO gap among other structures. Also, there are no C-C double bonds by the value of average C-C single bond 1.456 Å, and on the other hand, it has the shortest average Si-C bond length of 1.784 Å. The Pr@ $Si_{35}C_{35}$

structure is the second stable structure by having -5.574 eV/atom of binding energy. Where Table 5.1.5 shows that the triplet state of the Nd@$Si_{35}C_{35}$ structure is the most stable by having the lowest value of binding energy is -5.841 eV/atom. Moreover, The Nd atom moves a little bit from the center of fullerene with an average distance from the cage 3.309 Å. The diameters of Nd@ $Si_{35}C_{35}$ are 8.652 on the z-axis and 10.758 on the x-axis, which is shorter than $Si_{35}C_{35}$ diameters. The HOMO-LUMO gaps are 1.144 eV for spin-up and 1.159 eV for spin-down.

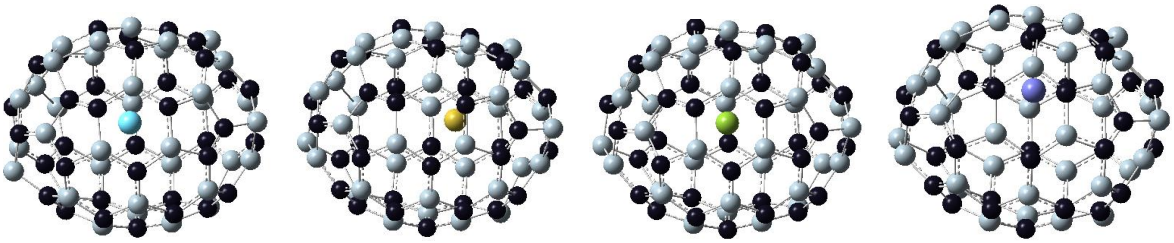

(a) La@$Si_{35}C_{35}$ (b) Ce@$Si_{35}C_{35}$ (c) Pr@$Si_{35}C_{35}$ (d) Nd@$Si_{35}C_{35}$

Figure 5.1.7: shows the relaxed structures R@ $Si_{35}C_{35}$ fullerene structure; R= La, Ce, Pr, and Nd.

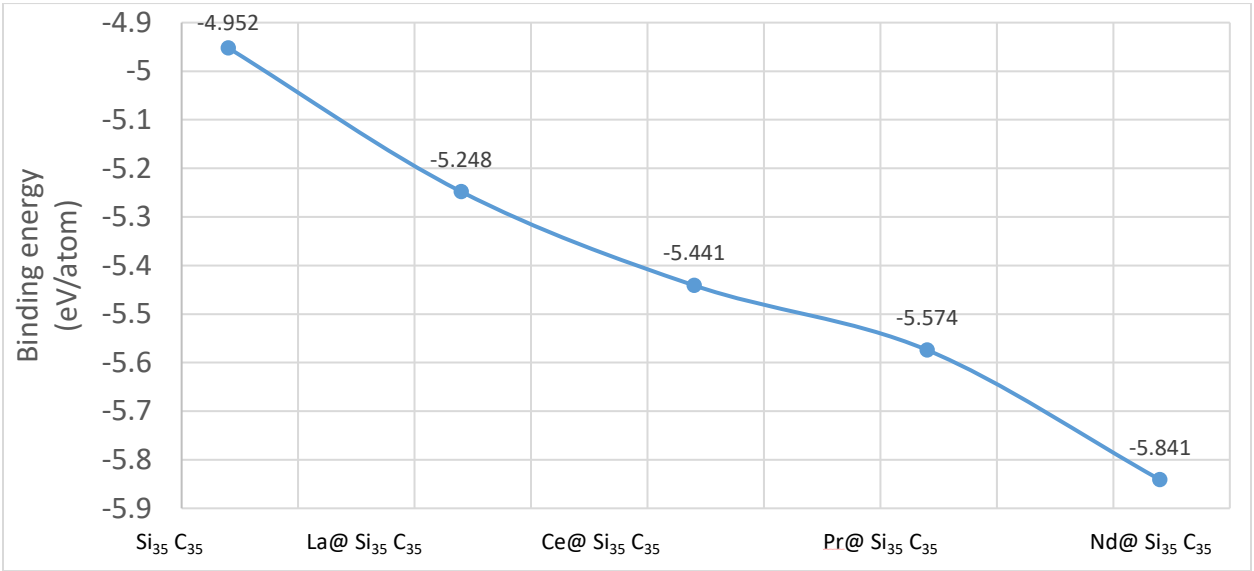

Figure 5.1.8 shows the binding energy (eV/atom) for Si_{35} C_{35} endohedral doping atoms of rare-earth atoms

5.1.3. Magnetic Properties of Endohedral Doping

5.1.3-A C_{60} and C_{70} Fullerenes

The rare-earth atoms have good magnetic and electronic properties[113][114][105]. For example, the magnetic properties of the Nd rare-earth atom are very valuable. Magnetic fields are created when unpaired electrons spin in the same way. Because of the Nd orbital electron structure, the rare-earth atoms may store huge quantities of magnetic energy[115][116]. Table 5.1.5 shows the magnetic moment values for single atoms of rare-earth atoms and endohedral doping of transition metal atoms at C_{60}, C_{70}, $Si_{35}C_{35}$, and $Si_{35}C_{35}$ structures. Also, figures 5.1.9 to 5.1.12 show the spin magnetic density and HOMO, and LUMO orbital of endohedral doping atoms structures.

The first doping atom in this section is La. It has similar magnetic properties in the center of C_{60} and C_{70} fullerene, where the La magnetic moments of the quartet state in C_{60} are $2.014\mu_B$ and $2.015\mu_B$ In C_{70} fullerene. Where the La start loses some magnetic moments, almost $1\mu_B$, and share them with the cage of C_{60} and C_{70} fullerene as shown in figures Figure 5.1.9 and Figure 5.1.10.

The figure 5.1.10 shows the interaction between the Ce atom and the cage. As a result of interacting between the cage and Ce atom, the cage surface atoms retain almost $1\mu_B$ to the Ce atom. Moreover, Ce beaver similar in the C_{70} cage by holding the magnetic moment $2.992\mu_B$ as shown in figures figure 5.1.9 and figure 5.1.10.

The figure 5.1.9 and figure 5.1.10 of Pr@C_{60} structures show the interaction between the Pr and cage surface. As a result, the C_{60} and C_{70} cage retain 1.995 and $1.997\mu_B$ to the Pr atom. On the other hand, the doping Nd atom has almost the same magnetic moment in the C_{60} and C_{70} fullerene, which are 2.997 and $2.996\mu_B$. This means Nd atom has the same behaver in C_{60} and C_{70}, while Nd free atom has $2\mu_B$ of magnetic moment at triplet state. We can conclusion that the rare-earth atoms

behave similar in the center on C_{60} and C_{70} fullerenes by holding almost the same amount of magnetic moments shown in Table 5.1.5.

Table 5.1.5: Shows the magnetic moment for single atoms of rare-earth atoms and endohedral doping of transition metal atoms at C_{60}, C_{70}, $Si_{35}C_{35}$, and $Si_{35}C_{35}$ structures.

Atoms	Magnetic moments (for atom)	Magnetic moments (for single atom @ C_{60})	Magnetic moments (for atom @C_{70})	Magnetic moments (for single atom @$Si_{30}C_{30}$)	Magnetic moments (for single atom @$Si_{35}C_{35}$)	Multiplicity
La	3.0	2.014	2.015	1.920	2.294	Quartet
Ce	2.0	2.989	2.992	1.647	2.992	Triplet
Pr	3.0	3.995	3.997	3.982	3.99	Quartet
Nd	2.0	2.997	2.996	2.983	4.980	Triplet

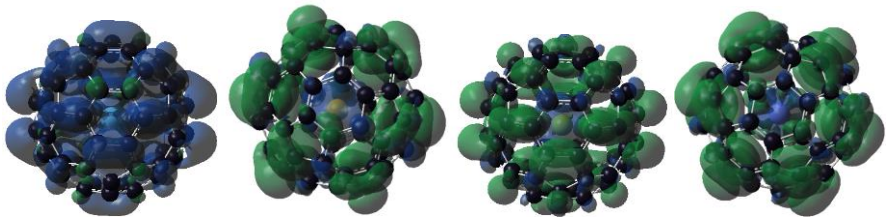

(a) La@C_{60} (b) Ce@C_{60} (c) Pr@C_{60} (d) Nd@C_{60}

Figure 5.1.9: showed the magnetic moment structures of R@ C_{60} fullerene, where R= La, Ce, Pr, and Nd. The green cooler represents the negative value of magnetic moments, and the blue cooler represents the positive value of magnetic moments.

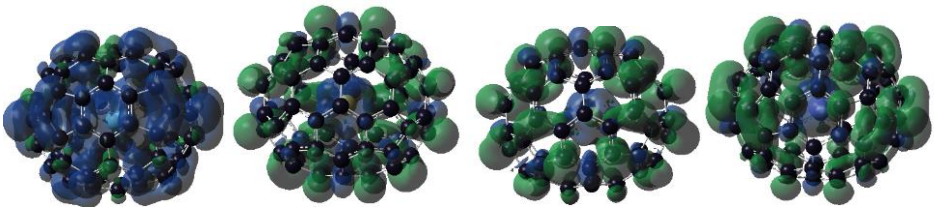

(a) La@C_{70} (b) Ce@C_{70} (c) Pr@C_{70} (d) Nd@C_{70}

Figure 5.1.10: showed the magnetic moment structures of R@ C_{70} fullerene, where R= La, Ce, Pr, and Nd. The green cooler represents the negative value of magnetic moments, and the blue cooler represents the positive value of magnetic moments.

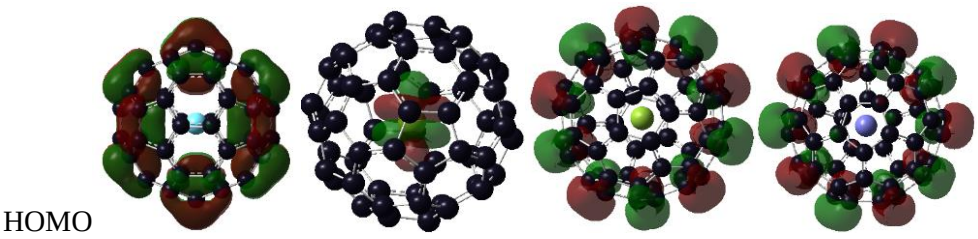

HOMO

(a) La@C_{60}. (b) Ce@C_{60} (c) Pr@C_{60} (d) Nd@C_{60}

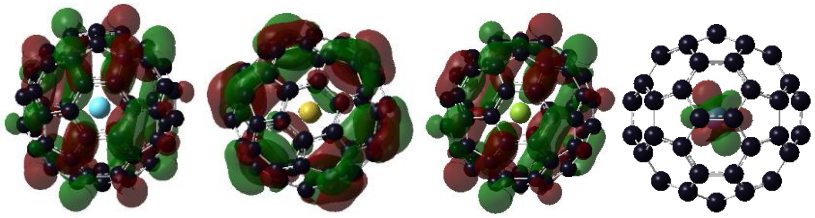

LUMO

(a) La@C_{60}. (b) Ce@C_{60} (c) Pr@C_{60} (d) Nd@C_{60}

Figure 5.1.11: shows the molecular orbitals (MO) of HOMO, the highest occupied molecular orbital, and LUMO lowest unoccupied molecular orbital for R@C_{60} fullerene, where R= La, Ce, Pr, and Nd.

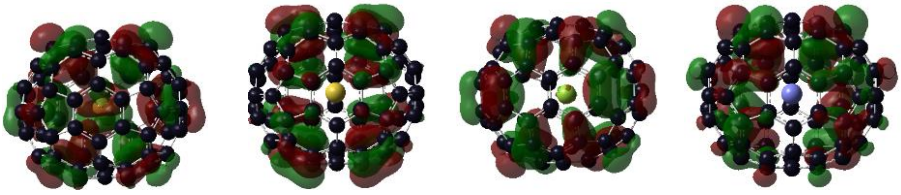

HOMO

(a) La@C_{70}. (b) Ce@C_{70} (c) Pr@C_{70} (d) Nd@C_{70}

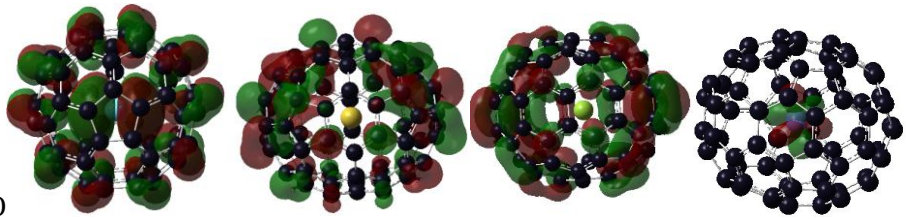

LUMO

(a) La@C_{70}. (b) Ce@C_{70} (c) Pr@C_{70} (d) Nd@C_{70}

Figure 5.1.12: shows the molecular orbitals (MO) of HOMO, the highest occupied molecular orbital and LUMO lowest unoccupied molecular orbital, for R@C_{70} fullerene, where R= La, Ce, Pr, and Nd.

5.1.3-B $Si_{30}C_{30}$ and $Si_{35}C_{35}$ Fullerenes

Figures 5.1.15 and 5.1.18 show the spin magnetic moment of $Si_{30}C_{30}$ and $Si_{35}C_{35}$ endohedral doping of rare-earth atoms (R=La, Ce, Pr, and Nd). Also, figures 5.1.16 and 5.1.19 show the

HOMO orbital of $Si_{30}C_{30}$ and $Si_{35}C_{35}$ endohedral doping of rare-earth atoms (R= La, Ce, Pr, and Nd). The La atom in the center of $Si_{30}C_{30}$ has a value of $1.920\mu_B$ of magnetic moments where it shares $1.08\mu_B$ with cage. In addition, The HOMO orbital of $La@Si_{30}C_{30\ shows}$ La HOMO orbital atom is overlapping with the Si atom of the cage surface, and there is a Si-C bi bond. For $La@Si_{35}C_{35,}$ magnetic moment is 2.294 μ_B while free La magnetic moment is $3\mu_B$ for triplet state. The next doping atom is Ce, where it behaves similarly in C_{70} and $Si_{35}C_{35}$ because the Ce atom has the same value of magnetic moments of $2.992\mu_B$. On the other hand, the Ce atom at $Si_{30}C_{30}$ shares its magnetic moment with the cage surface because it is bonded with the cage atom.

The rare-earth atoms in the center of $Si_{30}C_{30}$ and $Si_{35}C_{35}$ have shown interestingly to be magnetical. In the triplet state, the Nd has $2.983\mu_B$ at $Si_{30}C_{30}$ structure while free Nd atom has $2\mu_B$ in the triplet state. On the other hand, the Nd atom holds $4.9795\mu_B$ $Si_{35}C_{35,}$ which means the cage retains $2.979\mu_B$ to the Nb atom. Also, the Pr atom has an interesting value of magnetic moment where there is $0.009\mu_B$ between the magnetic moment of Pr in $Si_{30}C_{30}$ and $Si_{35}C_{35}$ structures. The Ce atom share $0.353\mu_B$ with the $Si_{30}C_{30}$ cage, and on the other hand, the $Si_{35}C_{35}$ cage retains $0.992\mu_B$.

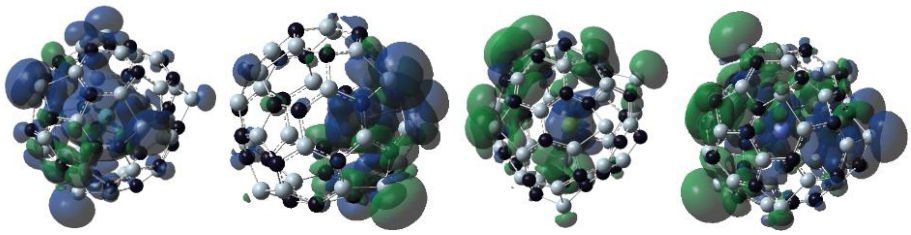

(a) $La@Si_{30}C_{30}$ (b) $Ce@Si_{30}C_{30}$ (c) $Pr@Si_{30}C_{30}$ (d) $Nd@Si_{30}C_{30}$

Figure 5.1.15: showed the magnetic moment structures of $R@Si_{30}C_{30}$ fullerene, where R= Nd, Pr, Ce, and La. The green cooler represents the negative value of magnetic moments, and the blue cooler represents the positive value of magnetic moments.

HOMO

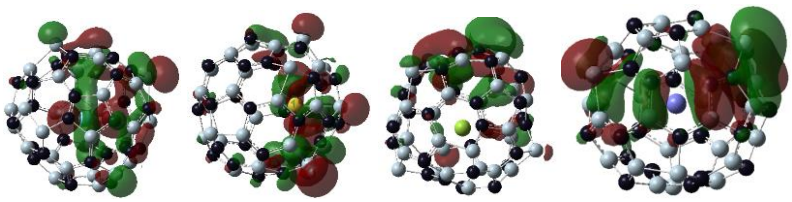

(a) La@$Si_{30}C_{30}$ (b) Ce@$Si_{30}C_{30}$ (c) Pr@$Si_{30}C_{30}$ (d) Nd@$Si_{30}C_{30}$

LUMO

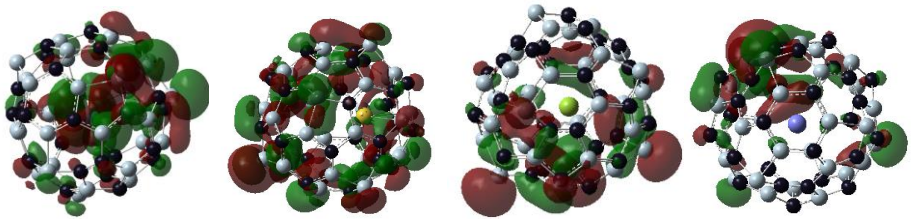

(a) La@$Si_{30}C_{30}$ (b) Ce@$Si_{30}C_{30}$ (c) Pr@$Si_{30}C_{30}$ (d) Nd@$Si_{30}C_{30}$

Figure 5.1.16: shows the molecular orbitals (MO) of HOMO, the highest occupied molecular orbital, LUMO lowest unoccupied molecular orbital for R@$Si_{30}C_{30}$ fullerene structure; R= La, Ce, Pr, and Nd

There are no HOMO and LUMO on Pr and Nd atoms as shown in figure 5.1.16. So, we calculate the HOMO-n and LUMO-n; n=1- 4 to see the energy level the doping atoms start contributing to the cage . The Pr@$Si_{30}C_{30}$ energy eigenvalue for Alpha HOMO is -5.097eV, and for Alpha, LUMO is -3.886 eV and HOMO-LUMO gap 1.211 eV. the energy eigenvalue for Beta HOMO is -4.719 eV and Beta LUMO is -3.938 eV; HOMO-LUMO gap is 0.782 eV. where the Alpha HOMO is lower energy than beta HOMO by 3.755 eV. The first contribution between the Pr atom and the cage shows at HOMO-4, as shown in figure 5.1.17. In addition the energy eigenvalue for Alpha HOMO is -5.266eV, which is lower than Beta HOMO, and Alpha LUMO is -4.133 eV, so the HOMO-LUMO gap is 1.133 eV. The beta HOMO is -5.065eV and Beta LUMO is -4.147 eV the energy difference between them is 0.928 eV. Up to HOMO-4, there is HOMO on the doping Nd atom as shown in figure 5.1.17.

The Alpha HOMO energy is lower than the beta HOMO energy at Pr@$Si_{30}C_{30}$ structure.

Alpha HOMO energy is -5.238 eV, and Alpha LUMO energy is -3667 eV ; the HOMO-LUMO ga is 1.571 eV . where the first home shows on the Pr atom at HOMO-4. On the other hand, the HOMO shows on the Nd at HOMO-2, as shown in figure 5.1.14 . Their energy eigenvalue of Alpha HOMO is -5.379 eV and Alpha LUMO is -4.235 eV and Beta=-4.717 eV and Beta LUMO is -3.557 eV.

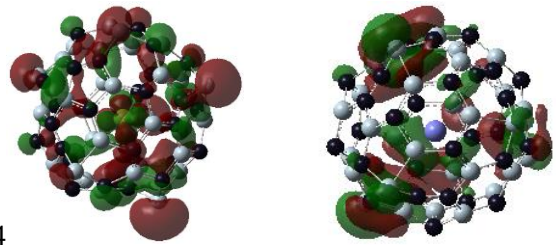

HOMO-4

$Pr@Si_{30}C_{30}$ $Nd@Si_{30}C_{30}$

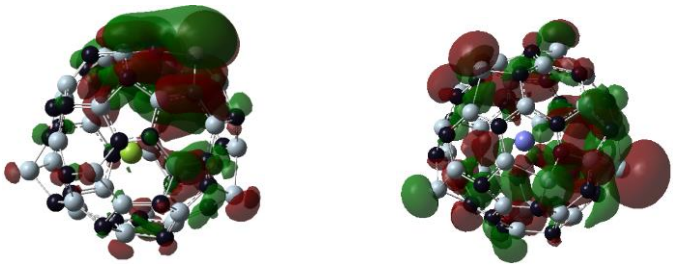

LUMO+3 LUMO+2

$Pr@Si_{30}C_{30}$ $Nd@Si_{30}C_{30}$

Figure 5.1.17: shows the molecular orbitals (MO) of HOMO-4, the highest occupied molecular orbital, LUMO+2 and LUMO+3 lowest unoccupied molecular orbital for $R@Si_{30}C_{30}$ fullerene structure; R= La, Ce, Pr, and Nd

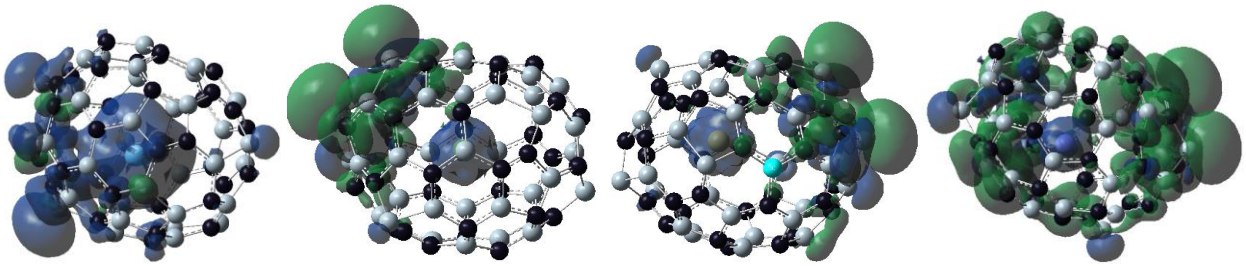

(a) $La@Si_{35}C_{35}$ (b) $Ce@Si_{35}C_{35}$ (c) $Pr@Si_{35}C_{35}$ (d) $Nd@Si_{35}C_{35}$

Figure 5.1.18: showed the magnetic moment structures of $R@Si_{35}C_{35}$ fullerene, where R= La, Ce, Pr, and Nd. The green cooler represents the negative value of magnetic moments, and the blue cooler represents the positive value of magnetic moments.

HOMO

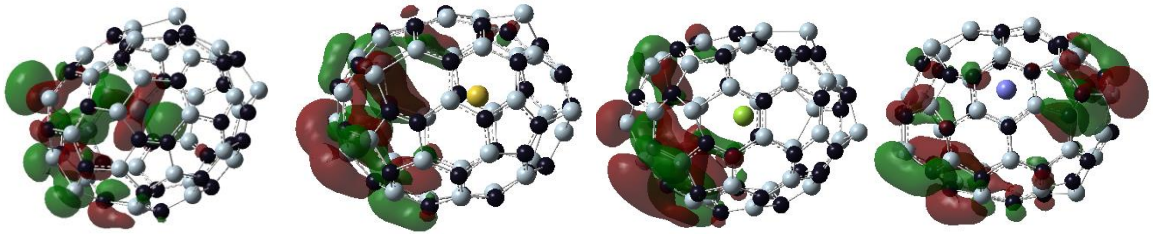

(a) $La@Si_{35}C_{35}$ (b) $Ce@Si_{35}C_{35}$ (c) $Pr@Si_{35}C_{35}$ (d) $Nd@Si_{35}C_{35}$

LUMO

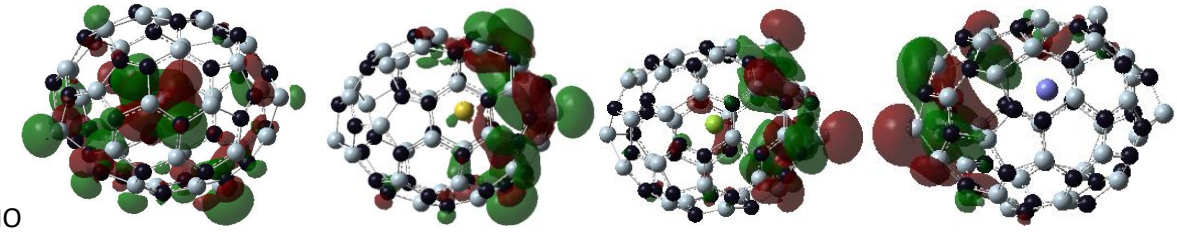

(a) $La@Si_{35}C_{35}$ (b) $Ce@Si_{35}C_{35}$ (c) $Pr@Si_{35}C_{35}$ (d) $Nd@Si_{35}C_{35}$

Figure 5.1.19: shows the molecular orbitals (MO) of HOMO, the highest occupied molecular orbital for $R@Si_{35}C_{35}$ fullerene structure; R= La, Ce, Pr, and Nd.

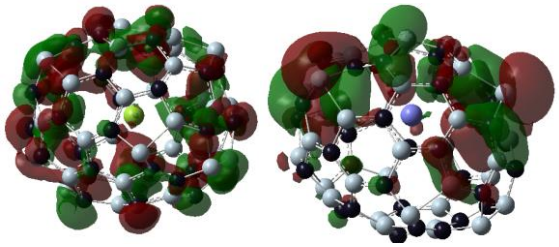

HOMO-4 HOMO-2

$Pr@Si_{35}C_{35}$ $Nd@Si_{35}C_{35}$

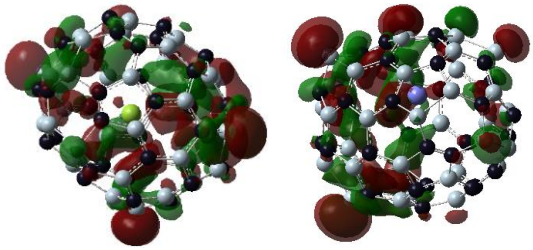

LUMO+3 LUMO+4

$Pr@Si_{35}C_{35}$ $Nd@Si_{35}C_{35}$

Figure 5.1.20: shows the molecular orbitals (MO) of HOMO-2 and HOMO-4, the highest occupied molecular orbital, LUMO+3 andLUMO+4 lowest unoccupied molecular orbital for $R@Si_{30}C_{30}$ fullerene structure; R= La, Ce, Pr, and Nd

Chapter 6

6.1 Ab Initial Molecular Dynamic (AIMD) Simulation

The first step of our simulation is to start our study with the C_{30}-bowl structure because it is the most stable $Si_{30}C_{30}$ isomer fullerenes. First, to relax the initial structure of the C_{30}-bowl structure, we start the calculation with regular DFT calculation. After that, we evaluated the temperature effects on the C_{30}-bowl structure starting at 50K. The simulation was run for 1ps; molecular dynamic simulations were carried out canonical ensemble (NVT) using the Nose-Hoover thermostat process. The result shows that the C_{30}-bowl structure is thermodynamically the most stable at $0K$ but not dynamically stable at high temperatures. Note, increasing the number of C-C bonds increases the stability and helps to be thermodynamically stable. After that, we start simulating the sphere structure start at 50K up to 500K after regular DFT calculation. Sphere structure is thermodynamically stable at $0K$ and dynamically stable up to very high temperatures. Increasing the number of Si-C bonds in the structure helps stability dynamically at high temperatures. Sphere structure was calculated up to 2400K for 1ps with 100K interval and up to 1500K for 2ps with 50K interval. The structure remains as a sphere without much distortion, as shown in Appendix A.

In the following sections, we will show the endohedral doping atoms of the Si_mC_n fullerene result in detail.

6.1.1 Computational Method.

The theoretical basis of this study was done on the density functional theory (DFT) as performed in the Vienna ab initio simulation program using the projector augmented wave technique (PAW) (VASP)[78][79][80][81]. The computations were calculated using the Perdew-

Burke-Ernzerhog (PBE) [117][117] by Generalized gradient approximation (GGA) functional[118][119]. The electrical self-consistent loop's resolution requirements were chosen to be equivalent to or less than $1*10^{-6}$ eV. The plane-wave basis set has a kinetic energy cut-off of 520 eV. Ab initio molecular dynamics simulations[120][121][117][122] were used to investigate the structural characteristics at non-zero kelvin temperatures, and the Nose-Hoover thermostat process was carried out canonical ensemble (NVT). The lattice parameters of a=b=c=22.651, alpha=beta=gamma=90 degrees, and a temperature interval of 50K between calculations. We utilized a five fs time step for all our AIMD simulations. The computing cost of AIMD is considerably high compared to classical MD. The reason is that it integrates the quantum mechanical characteristics of the particles in a system. As a result, the 5 ps long is limited for our AIMD simulation.

6.1.2. (AIMD) Simulation of Si_mC_n Fullerene

Here we will show the study of endohedral doping atoms of transition metal and rare-earth atoms at Si_mC_n fullerene; m=n=30 or 35 atoms.

6.1.2-A. Tarnation Metal Atoms

- **$Si_{30}C_{30}$ Fullerene**

The molecular dynamics simulation of endohedral doping of transition metal atoms was performed with DFT-VASP, ab initial MD (AIMD). We investigated the composition of spheres-M; M= W, Fe, Ta, Hf, and Nb atoms. First, to relax the initial structure of the endohedral doping of transition metal atoms, we start the calculation with regular DFT calculation. After that, we evaluated the temperature effects on endohedral doping of transition metal atoms structure starting

at 50K. The simulation was run for 5ps using the Nose-Hoover thermostat process; molecular dynamic simulations were carried out canonical ensemble (NVT).

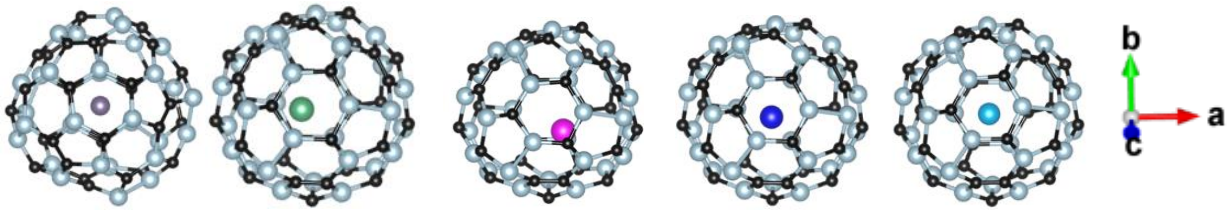

(a) Sphere-Fe (b) sphere-Nb (c) sphere-Hf (d) sphere-Ta (e) sphere-W

Figure 6.1.1: shows a snapshot of VASP simulation at 0K for endohedral doping of transition metal atoms (Fe, Nb, Hf, Ta, and W)

We have 61 atoms in our system, with lattice parameters of a=b=c=22.651Å, alpha=beta=gamma=90 degrees. Figure 6.1.1 shows the simulation of endohedral doping of transition metal atoms W. Fe, Ta, Hf, and Nb of a standard DFT calculation at zero degrees Kelvin. The doping atoms W and Fe remain at the center at 0K. However, the Ta, Nb, and Hf atoms shifted a little from the sphere structure's center to a -a direction, as shown in figure 6.1.1. Then, by using the DFT pair potential, we begin the AIMD (NVT) calculation. It is worth noting that the study's aim is not to predict the endohedral doping fullerene's thermodynamic stability. It is to predict the magnetic properties of endohedral doping atoms at increasing temperatures.

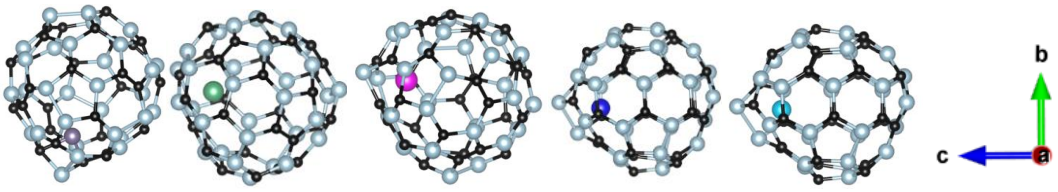

(a) sphere-Fe (b) sphere-Nb (c) sphere-Hf (d) sphere-Ta (e) sphere-W

Figure 6.1.2: shows a snapshot of ab initial MD (AIMD) simulation performed with DFT-VASP at 50K for endohedral doping of transition metal atoms (Fe, Nb, Hf, Ta, and W)

We use Ab Initio Molecular Dynamic (AIMD) Simulation to investigate doping atoms' magnetic properties at the sphere structure. Also, we keep the number of atoms, volume, and temperature is all fixed (NVT). Before starting the simulation, the magnetic moment considers as their multiplicity value at their ground state energy. Figure 6.1.2 shows a snapshot of ab initial MD (AIMD) simulation performed with DFT-VASP at 50K for endohedral doping of transition metal atoms (W. Fe, Ta, Hf, and Nb). The first structure is sphere-W. When the simulation starts, the W atom has $2\mu_B$. During increasing the temperature from 0K to 50K, the W atom moves from the center close to the cage surface and pushes the cage atoms out. As a result, the W atom does not bond with the cage atom. However, the doping atom loses its magnetic moment at 50K, which is $0\mu_B$.

The following structure of our AIMD simulation is sphere-Fe. Here we let the Fe atom hold $2\mu_B$ at start simulation. The Fe atom moves from the center to the cage surface while increasing the temperature. Then, the Fe bonds with carbon atoms of the cage where the Fe possesses $1.691\mu_B$ as shown in figure 6.1.4. The next structure for our study is sphere-Ta. The Ta atom has a value of magnetic moment $3\mu_B$ before starting the simulation. We find the Ta the same trend as the W atom. It moves from the sphere's center to the cage without bonds with the cage, as shown in figure 6.1.2. In addition, the Ta magnetic moment decreases while the temperature increases. The Ta atom has a value of the magnetic moment at 50K of $0.540\mu_B$. This means cage atoms have shared some of the magnetic moments of the system.

The last two structures of our study in AIMD simulation are sphere-Hf and sphere-Nb. Before the simulation, we keep the Hf and Nb atoms holding$2\mu_B$ and $3\mu_B$ values of magnate's moments. After simulation, Hf and Nb atom magnetic moments decrease to $0.016\mu_B$ and $0.653\mu_B$ as shown in figure 6.1.4. This means the magnetic moments of endohedral doping atoms decrease while the temperature increases. Because when the molecular starts oscillation at increasing the system's temperature, the doping atoms lose their ability to stay in the center of the cage. As a result, Hf and Nb atoms have the same trend as W and Ta atoms. They move from the center of the cage without bonds with cage atoms. In addition, while the temperature increases by 50K intervals each calculation, transition metal atoms (Nb, Fe, Hf, and Ta) hold a small value in the magnetic moment. Sphere-M; M=Nb, Fe, Hf, Ta, and W structures are thermodynamically stable at $0K$ and dynamically stable at 300K temperature as there is no distortion in the structures, as shown in figure 6.1.3. Note, endohedral doping of $Si_{30}C_{30}$ can be thermodynamic stable up to 1000K without distortion at 5ps simulation and up to1500K without distortion at 2ps simulation as showing in Appendix A.

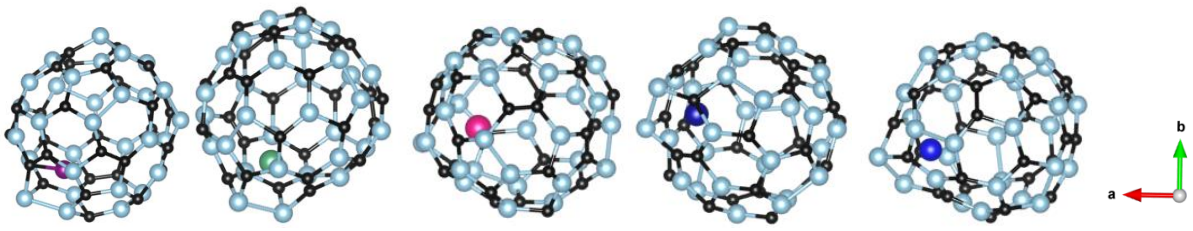

(a) sphere-Fe (b) sphere-Nb (c) sphere-Hf (d) sphere-Ta (e) sphere-W

figure 6.1.3: shows a snapshot of ab initial MD (AIMD) simulation performed with DFT-VASP at 300K for endohedral doping of transition metal atoms (Fe, Nb, Hf, Ta, and W)

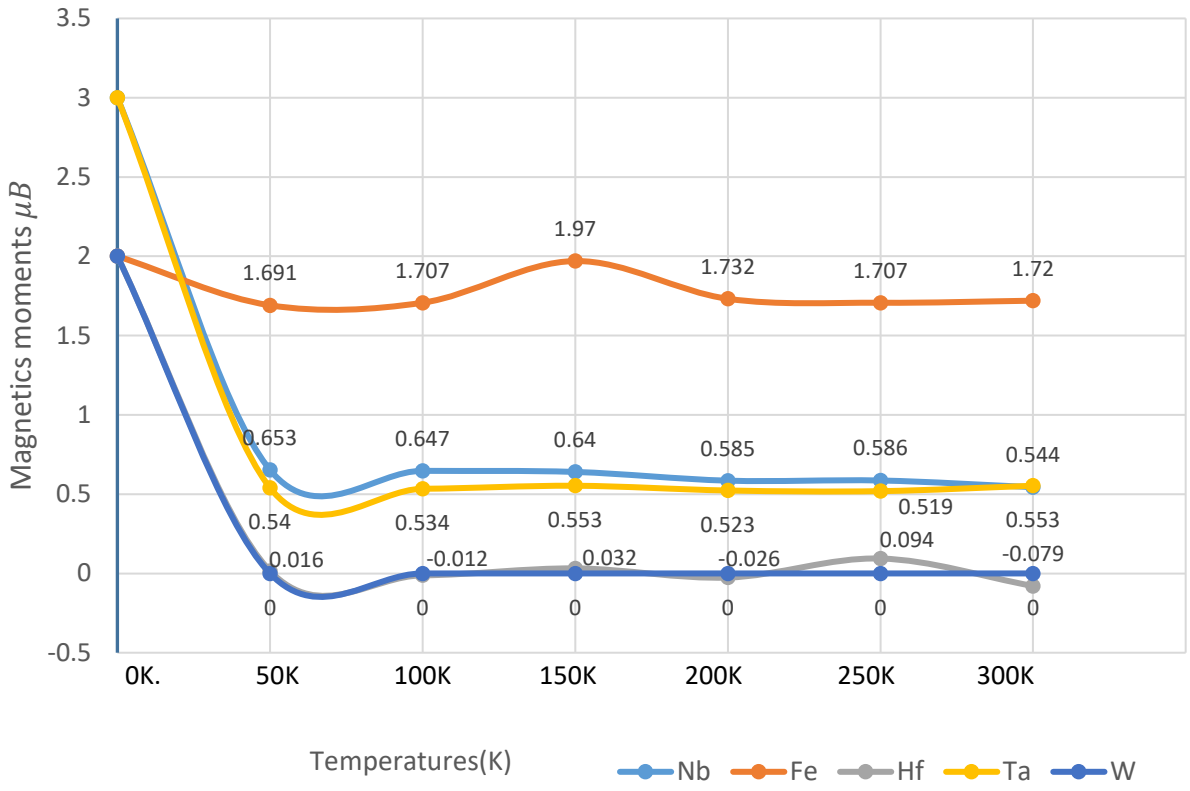

Figure 6.1.4 show the magnetic moment rare-earth doped atoms at $Si_{30}C_{30}$ (sphere-M) fullerene while the temperture is increasing from zero K up to room tempertuers.

➢ $Si_{35}C_{35}$ Fullerene.

Our system has 71 atoms with the lattice constants a=b=c=26.37Å , alpha= gama =beta =90 degrees. It is worth emphasizing that the study's goal is not to determine the thermodynamic stability of endohedral doping structures. The Ab initio molecular dynamic (AIMD) implemented in VASP was used to produce a molecular dynamics simulation of endohedral doping of transition metals atoms. We study at the isomers of $M@Si_{35}C_{35}$, where M=Nb, Fe, Hf, Ta, and W atoms. To begin the calculation, we do a standard DFT simulation to relax the original structure of endohedral doping. Figure 6.1.5 represents the endohedral doping of transition metals atoms implemented in VASP simulation at zero Kelvin. In addition, all doping of transition metals atoms (Nb, Fe, Hf, Ta, and W) are still in the center of $Si_{35}C_{35}$. Then we can start the AIMD-(NVT) computation by

utilizing the DFT pair potential at 50K. We examined the impacts of temperature on endohedral doping of transition metal atoms structures. The simulation was performed for 5ps using the Nose-thermostat method, with a canonical ensemble molecular dynamics system (NVT).

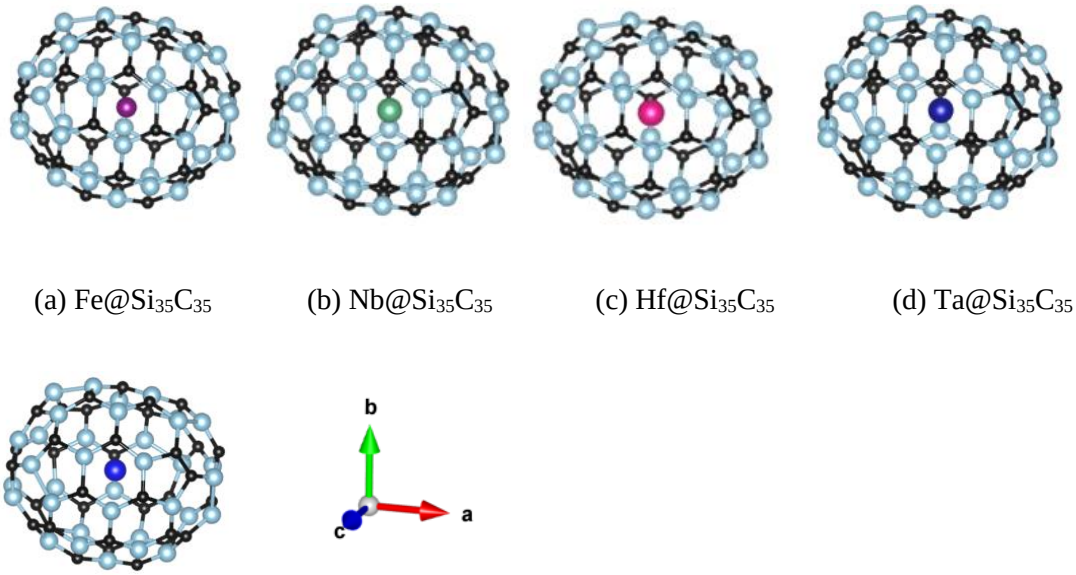

(a) $Fe@Si_{35}C_{35}$ (b) $Nb@Si_{35}C_{35}$ (c) $Hf@Si_{35}C_{35}$ (d) $Ta@Si_{35}C_{35}$

(e) $W@Si_{35}C_{35}$

Figure 6.1.5: shows simulation at 0K for $M@Si_{35}C_{35}$ endohedral doping of transition metal atoms, M= Fe, Nb, Hf, Ta, and W.

Nb@ $Si_{35}C_{35}$ is the first structure of AIMD simulation. The Nb atom starts with magnetic moments around $3\mu_B$, while the temperature increases, the magnetic moment of Nb decreases to $0.738\mu_B$ at 50K. In addition, the Nb atom moves from the center to the close of the fullerene cage. The following structure is $Fe@Si_{35}C_{35}$. Here the Fe starts the simulation with a magnetic moment value of $2\mu_B$. The Fe atom still holds almost all magnetic moments of $1.979\mu_B$ at 50 K. However, the Fe atom is bonded with the cage surface carbon atom, as shown in figure 6.1.6-(a). This means the Fe atom can easily interact without influence.

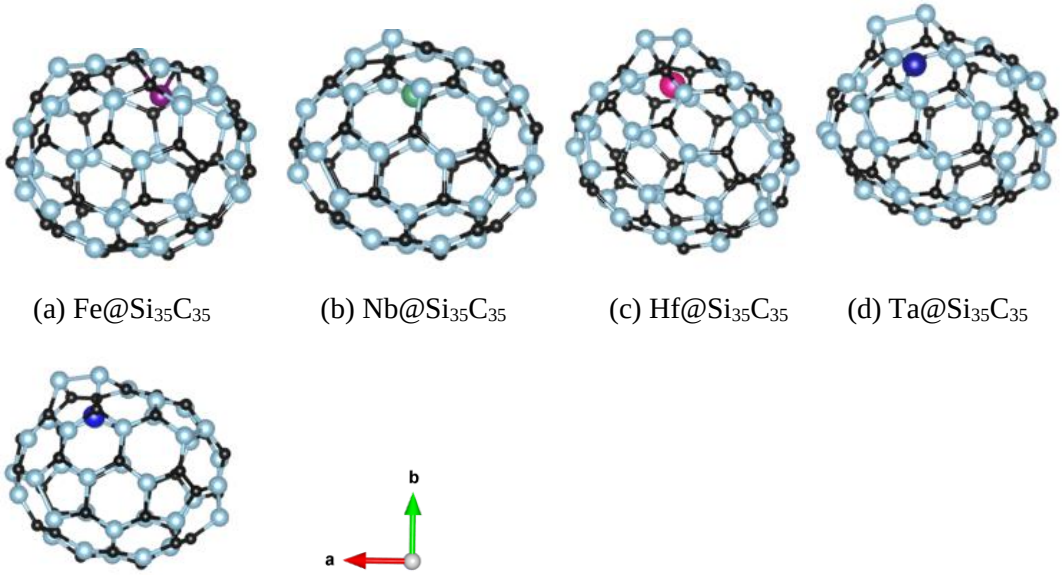

(a) $Fe@Si_{35}C_{35}$ (b) $Nb@Si_{35}C_{35}$ (c) $Hf@Si_{35}C_{35}$ (d) $Ta@Si_{35}C_{35}$

(e) $W@Si_{35}C_{35}$

Figure 6.1.6: shows ab initial MD (AIMD) simulation performed with DFT-VASP at 50K for $M@Si_{35}C_{35}$ endohedral doping of transition metal atoms, M= Fe, Nb, Hf, Ta, and W.

The $Ta@Si_{35}C_{35}$ is the following structure of the AIMD simulation study. The Ta atom has the same trend as the Nb atom. The magnetic moment decreases while the temperature increases. At 50K, the Ta magnetic moment is $0.575\mu_B$, while it was almost $3\mu_B$. The last two structures are $W@Si_{35}C_{35}$ and Hf $@Si_{35}C_{35}$. The W and Gf have the same trend of moving from the center to close to the surface cage. Also, they start the simulation of AIMD with $3\mu_B$. However, they lose their magnetic moment when the temperature is increasing, which is zeroμ_B. Figure 6.1.8 shows the magnetic moments of transition metal atoms at different temperatures of the $Si_{35}C_{35}$ structure. While the temperature is increasing, the doping atoms (Nb and Ta) have small values of magnetic moments compared to Fe atom values. The Fe atom has a good value of magnetic moments while the temperature is increasing. However, the Fe atom bonded with the cage atoms. As a result, the Fe atom can interact without influence. On the other hand, W and He atoms lose their magnetic moment as the temperature increases. Note, the endohedral doping of transition

metal atoms is thermodynamically stable at high temperature, up to 300K according to our simulation, without distortion, as shown in figure 6.1.7.

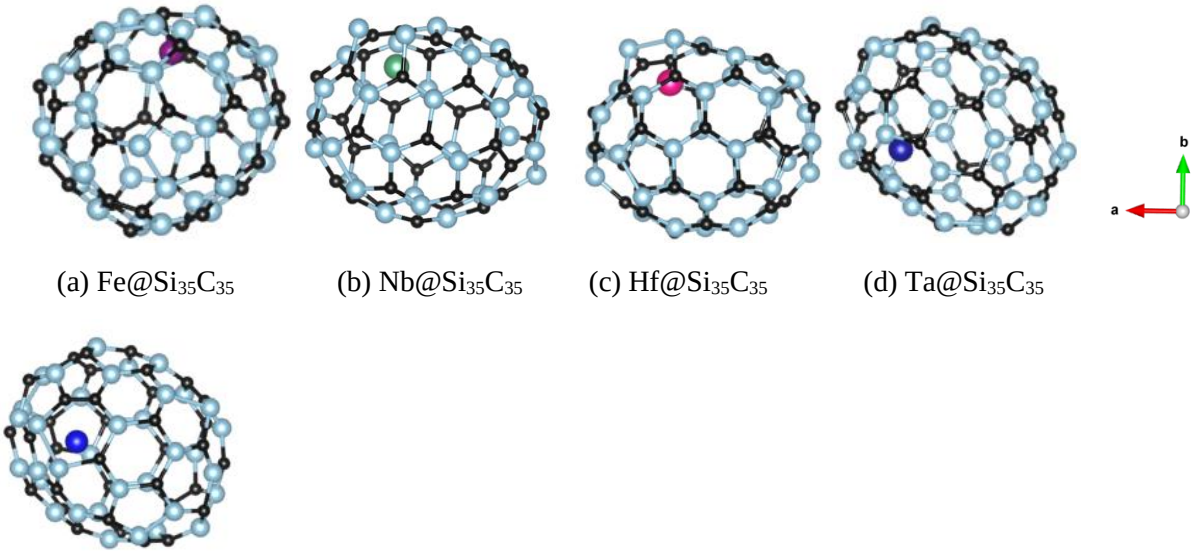

(a) $Fe@Si_{35}C_{35}$ (b) $Nb@Si_{35}C_{35}$ (c) $Hf@Si_{35}C_{35}$ (d) $Ta@Si_{35}C_{35}$

(e) $W@Si_{35}C_{35}$

Figure 6.1.7: shows a snapshot of ab initial MD (AIMD) simulation performed with DFT-VASP at 300K for endohedral doping of transition metal atoms (Fe, Nb, Hf, Ta, and W)

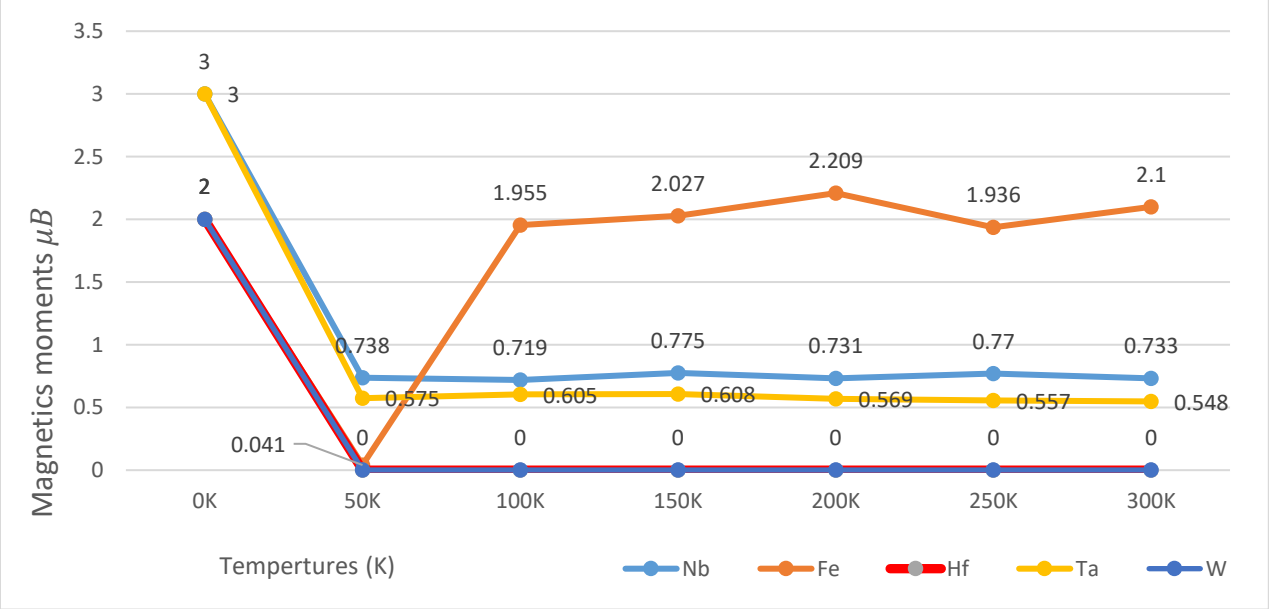

Figure 6.1.8: show the magnetic moment transition metal doped atoms at $Si_{35}C_{35}$ while the temperture is increasing from zero K up to room tempertuers.

6.1.2-B. Rare-Earth Atoms

➢ $Si_{30}C_{30}$ Fullerene

In our system there are 61 atoms, with lattice parameters of a=b=c=22.651Å, alpha=beta=gamma=90 degrees. We start the simulation with regular DFT calculation at 0K. Figure 6.1.9 shows the simulation of endohedral doping of rare-earth atoms (R=Nd, Pr, Ce, and La) at 0K. The figures show that all the doping atoms shifted from the sphere's center without touching the cage. We use Ab Initio Molecular Dynamic (AIMD) Simulation to study the doping atoms' magnetic properties at the sphere structure. Also, we keep the number of atoms, volume, and temperature is all fixed (NVT). The first step before starting the simulation, we considered the magnetic moment values as their multiplicity at their ground state energy.

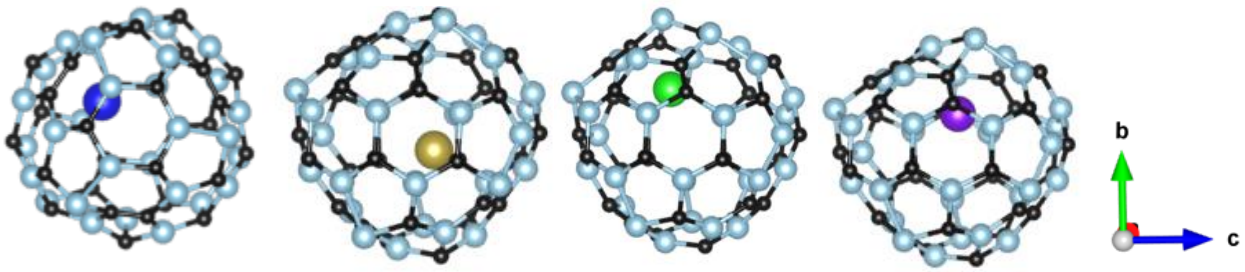

(a) La@$Si_{30}C_{30}$ (b) Ce@$Si_{30}C_{30}$ (c) Pr@$Si_{30}C_{30}$ (d) Nd@$Si_{30}C_{30}$

Figure 6.1.9: shows a snapshot of VASP simulation at 0K for endohedral doping of rare-earth atoms (R=La, Ce, Pr, and Nd)

The Nd@$Si_{30}C_{30}$ is the first structure of our AIMD simulation. The calculation started at 50K with $2\mu_B$ for Nd atom and zero μ_B for Si and C atoms also time step 5ps. After simulation, the Nd magnetic moment is $3.251\mu_B$. The doping atom, Nd, remains inside the cage without bonding with the cage surface, as shown in figure 6.1. 10-(a). The second of rare-earth atoms

is $Pr@Si_{30}C_{30}$. The simulation starts with $3\mu_B$ for Pr atom at 50K. After the simulation, the value of magnetic moment decreases while increasing the temperature to $2.102\mu_B$ as shown in Table 6.1.2.

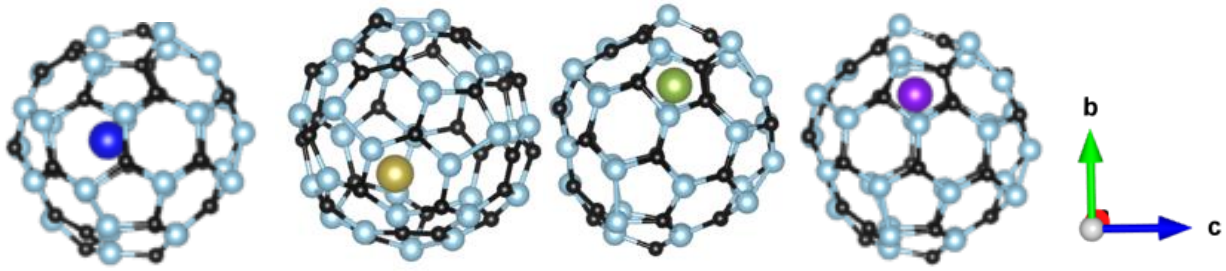

(a) $La@Si_{30}C_{30}$ (b) $Ce@Si_{30}C_{30}$ (c) $Pr@Si_{30}C_{30}$ (d) $Nd@Si_{30}C_{30}$

Figure 6.1.10: shows a snapshot of ab initial MD (AIMD) simulation at 50K for endohedral doping of rare-earth atoms (R=La, Ce, Pr, and Nd)

The following structures are $Ce@Si_{30}C_{30}$ and $La@Si_{30}C_{30}$. The Ce and La have shown no interest in being magnetically while increasing the temperature. Their magnetic moment decreases to 0.337 and $0.019\mu_B$ where they start the simulation at 0K with 2 and $3\mu_B$. So, we just carry out $Nd@Si_{30}C_{30}$ and $Pr@Si_{30}C_{30}$ structures to room temperatures because the Nd and Pr atom keep their magnetic moment while increasing the temperature. At 300K, the Nd has a value of the magnetic moment of 3.289 and $2.016\mu_B$.

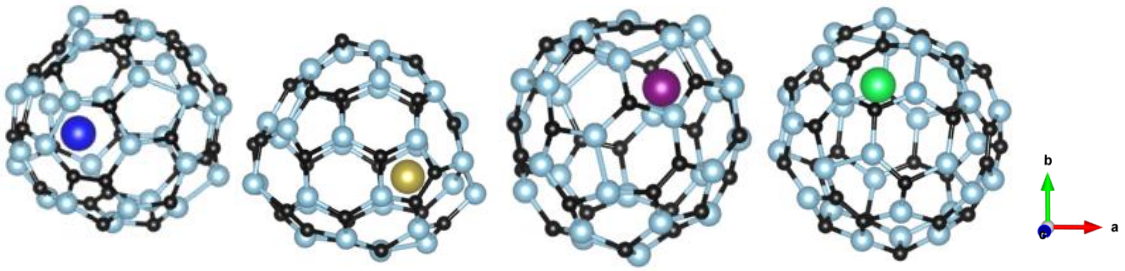

(a) $La@Si_{30}C_{30}$ (b) $Ce@Si_{30}C_{30}$ (c) $Pr@Si_{30}C_{30}$ (d) $Nd@Si_{30}C_{30}$

Figure 6.1.11: shows a snapshot of ab initial MD (AIMD) simulation at 300K for endohedral doping of rare-earth atoms (R=La, Ce, Pr, and Nd)

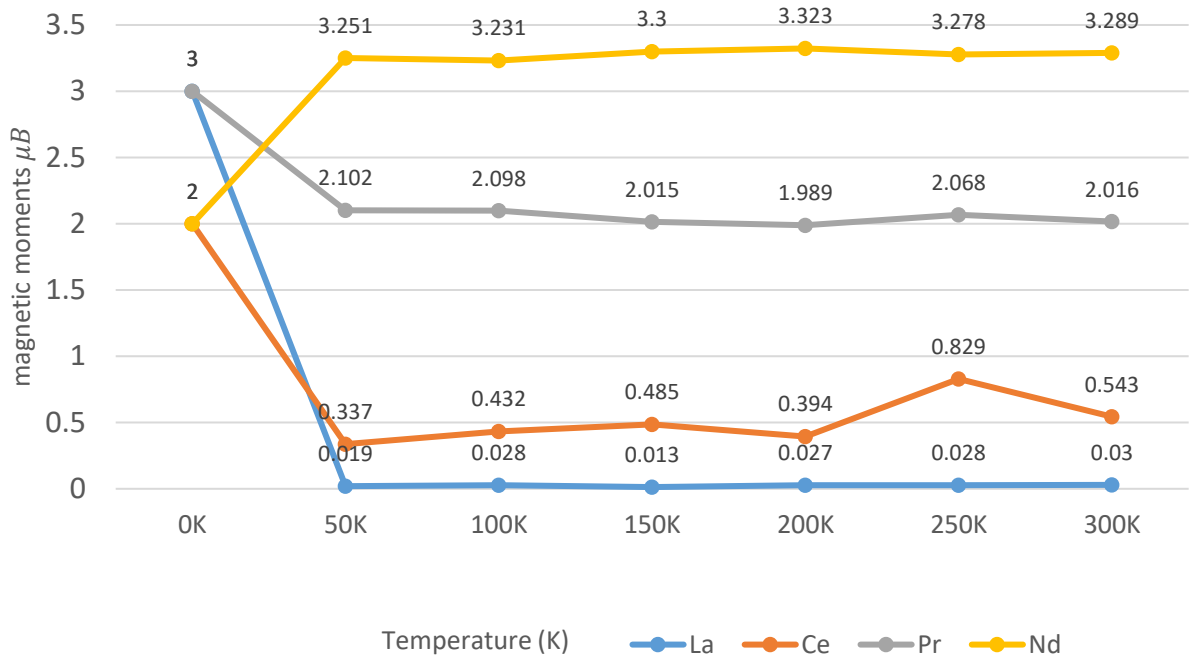

Figure 6.1.12: show the magnetic moment rare-earth doped atoms at $Si_{30}C_{30}$ while the temperture is increasing from zero K up to room tempertuers.

➢ $Si_{35}C_{35}$ Fullerene

There are 71 atoms in our system with the lattice constants a=b=c=26.37Å , alpha= gama =beta =90 degrees. The study's goal is not to determine the thermodynamic stability of endohedral doping structures. We study the R@$Si_{35}C_{35}$ structures, where R=Nd, Pr, Ce, and La atoms. To begin the calculation, we do a standard DFT simulation to relax the original structure of endohedral doping. The doping atoms (Nd, Pr, Ce, and La) remain almost in the center of the $Si_{35}C_{35}$ structures at zero K. Since the temperature increases, they (Nd, Pr, Ce, and La) start moving from the center to the cage without bonds. The magnetic moments of the Pr, Ce, and La atoms decrease at 50K, which are 2.175μ_B, 0.673μ_B, and 0.025μ_B. On the other hand, the only atoms whose magnetic moments have increased at 50 K is Nd which increases by 1.323μ_B while the initial value is 2μ_B. For that reason, we select the Nd@$Si_{35}C_{35}$ structure at room temperature investigation because the

result shows that the Nd atom has a range magnetic moment between 3.25μ_B and 3.36μ_B from 50K to 300K as shown in figure 6.1.16. For computational calculation problem, the Pr@$Si_{35}C_{35}$ has been calculated up to 200K, but it seems to have the same trend of the magnetic moment up to 300K of Pr@C_{60} fullerene.

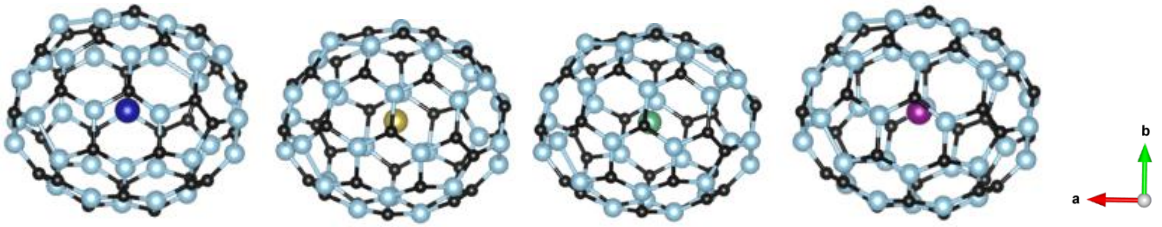

(a) La@$Si_{35}C_{35}$ (b) Ce@$Si_{35}C_{35}$ (c) Pr@$Si_{35}C_{35}$ (d) Nd@$Si_{35}C_{35}$

Figure 6.1.13: shows a snapshot of VASP simulation at 0K for endohedral doping of rare-earth atoms (R=La, Ce, Pr, and Nd)

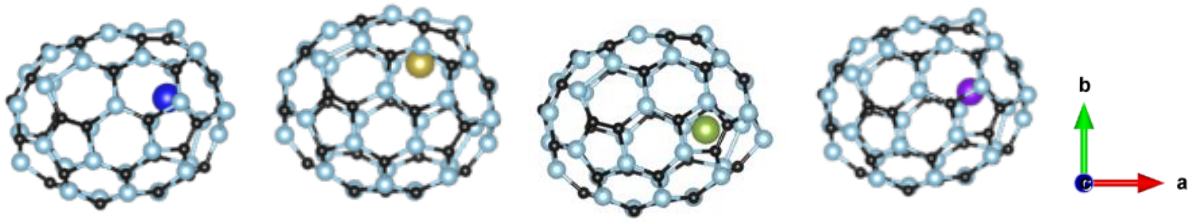

(a) La@$Si_{35}C_{35}$ (b) Ce@$Si_{35}C_{35}$ (c) Pr@$Si_{35}C_{35}$ (d) Nd@$Si_{35}C_{35}$

Figure 6.1.14: shows a snapshot of ab initial MD (AIMD) simulation at 50K for endohedral doping of rare-earth atoms (R=La, Ce, Pr, and Nd)

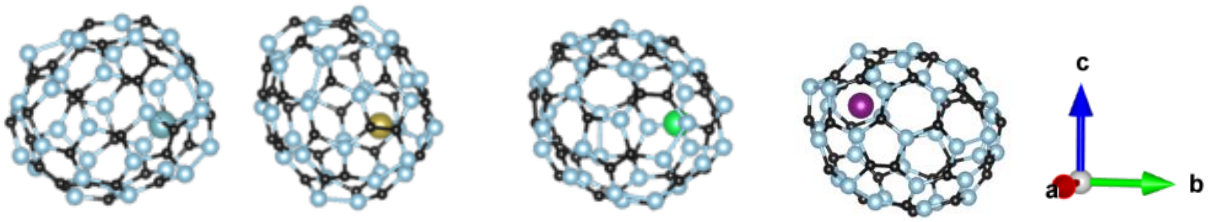

(a) La@$Si_{35}C_{35}$ (b) Ce@$Si_{35}C_{35}$ (c) Pr@$Si_{35}C_{35}$ (d) Nd@$Si_{35}C_{35}$

Figure 6.1.15: shows a snapshot of ab initial MD (AIMD) simulation at 300K for endohedral doping of rare-earth atoms (R= Ta, Ce, and Nd) and up to 200K for Pr@$Si_{35}C_{35}$.

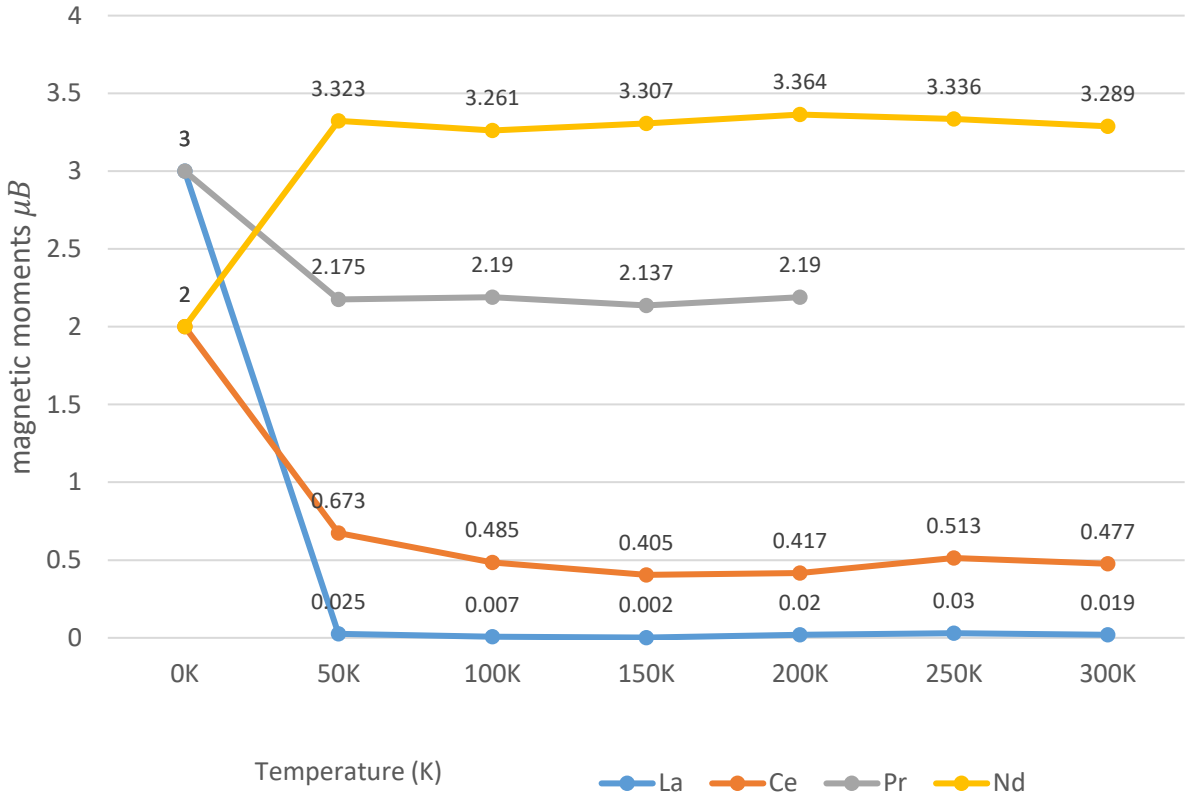

Figure 6.1.16: show the magnetic moment rare-earth doped atoms at $Si_{35}C_{35}$ while the temperture is increasing from zero K up to room tempertuers.

Chapter 7

7.1 Conclusions

Staring from Si_{60} fullerene templet, several configurations of $Si_{30}C_{30}$ clusters were studied. Hydrogen passivation was considered for all three-fold coordinated Si atoms, and the effects of the hydrogenation on the structures have been analyzed. The first noticeable effect of hydrogenation is the change of the stability order for the $Si_{30}C_{30}$ isomers. Second, the position of HOMO shifted significantly with H-passivation from Si to C sites. Third, some hydrogen-bonded to Si were found to break the bond and re-bonded with carbon atoms upon relaxation, even though no carbon atom was bonded with H before relaxing the structures. Fourth, hydrogen passivation has an interesting effect on the endohedral metal dopant, such as stabilizing the structures at higher spin multiplicities while retaining the spin magnetic moment on the dopant metal atom. Especially with hydrogen passivation, this endohedral metal atom with a magnetic moment prefers to stay near at the center of the cage structure, not near the surface of the $Si_{30}C_{30}$ cage. So, inside the hydrogenated $Si_{30}C_{30}$ cage, the spin state of the metal atom can be preserved from the outside chemical perturbations of the cage.

Enhancing the stability of SiC of fullerene structures by surface passivation is not very straightforward. The integrity of the structure and the cohesion between the atoms within the structure upon passivation depend on the local chemical environment on the fullerene surface. Even though all Si atoms in Si_{60} and all the $Si_{30}C_{30}$ considered here have 3-fold coordination, none of the hydrogenated structures could maintain the perfect fullerene sphere as was in $Si_{60}H_{60}$. Again, from the binding energy point of view, Si_{60} is more stable than $Si_{60}H_{60}$ due to the weakening of the Si-Si bond strengths. Among the $Si_{30}C_{30,}$ a few isomers could maintain sufficiently large cage-

type structures. In passivating large cage-type structures, a point to note is that there are all surface atoms and no bulk atoms in the case of cage structures. When bonding mismatch weakens the bonds in the neighborhood surface atoms, distortions or even collapse of the cages is possible. Several of the $Si_{30}C_{30}$ structures showed such behavior in this study. Also, having prior knowledge of the need for passivation for particular atoms for a large cage structure can be a daunting task. In this study, we have found that in several cases, some hydrogen atoms initially bonded with three-fold Si atoms were later moved to carbon atoms due to structural relaxation. The migration of hydrogen atoms from silicon to carbon atoms causes significant distortions in the cage structures; the higher the number of hydrogen atoms moved to the carbon atoms; the higher distortions were found in the $Si_{30}C_{30}$ cages. The near-spherical one is the one where the sp^3 type bonding was distributed almost equally over the structure, even on the carbon part. A symmetrization of the bonding over the structure's surface is needed to maintain a large fullerene-like spherical structure for SiC.

Along with the C_{60} fullerene's electronic properties, endohedral doping some transition metal atoms (Fe, Nb, Hf, Ta, and W) were considered to study their magnetic and electronic properties. The calculations shows that doped Nb and Ta atoms have a high value of spin magnetic moment by $4\mu_B$ and $3\mu_B$, respectively, where the total magnetic moments of doped M@C_{60} structures were $3\mu_B$ and $2\mu_B$. In addition, Fe, Hf, and W atoms show magnetic behavior by holding all spin magnetic moments of the system. We then select a spherical Si_{30}-C_{30} fullerene structure with a high number of Si-C bonds, 78 Si-C bonds, for endohedral doping of metal atoms. Among the dopants, the W and Fe atoms in the center of sphere structures behaves as if they were free W or Fe atom. The lack of interactions between these two atoms with the SiC fullerene cage wall imply that the magnetic moments on these endohedrally doped atoms can be protected from the

outer influences on SiC fullerenes. Moreover, Ta, Hf, and Nb have shown a good value of spin magnetic moment after relaxation. Endohedrals doping of transition metal dimers were considered as well and showed different behavior in the sphere structure compared to the endohedral metal atom doping. The sphere-W_2 structure is more stable by having lower binding energy than the sphere-W structure. On the other hand, the sphere-Fe_2 structure is less stable by having high binding energy than the sphere-Fe structure. Also, W-dimer and Fe-dimer keep their bonds in the sphere structure, which leads them to retain a good value of magnetic moments. In addition, Ta-dimer and Nb-dimer move towards the cage with increased dimer bond length. As a result, Ta-dimer and Nb-dimer share their magnetic moment with the cage surface. The Hf-dimer breaks its bond, and each Hf atom moved to opposite side and bonded with cage atoms.

For larger fullerenes, the $Si_{35}C_{35}$ the average diameters are 10.812 Å for the x-axis and 9.134 Å for the z-axis. However, this diameter decreases when we add transition metal atoms to it. The transition metal atoms in the $Si_{35}C_{35}$ fullerene are far enough from the cage retaining the magnetic moment. Also, our study shows that Nb@C_{70} and Nb@$Si_{35}C_{35}$ are stable structures by having lower binding energy than pristine fullerene. In addition, the Nb atom interacts with the cage surface by holding a high value of magnetic moments of Nb@C_{70}. On the other hand, in the C_{70} and $Si_{35}C_{35}$ fullerenes, the Fe, Ta, and W atoms behave as free atoms by holding almost all magnetic moments of the system.

The endohedral doping of rare-earth atoms (La, Ce, Pr, and Nd) makes the structures of C_{60}, C_{70}, $Si_{30}C_{30}$, and $Si_{35}C_{35}$ fullerene more stable. Adding rare-earth atoms at the center of the fullerene decreases the diameters compared to their original ones. Magnetically, La, Ce, Pr, and Nd have a good value of magnetic moments compared to their free atoms. For example, the Pr has almost $4\mu_B$ in C_{60}, C_{70}, $Si_{30}C_{30}$, and $Si_{35}C_{35}$ fullerene. Also, the Nd atom shows almost $3\mu_B$ in C_{60},

C_{70}, and $Si_{30}C_{30}$ fullerenes and $5\mu_B$ in $Si_{35}C_{35}$ fullerene.

From the DFT calculations, the endohedrally doped atoms, transition metals and rare-earth atoms, remained almost in the center of the sphere structure at 0K. From the ab initio Molecular Dynamics simulations, we found that as the temperature increased, the doping atoms leave the center of the cage and moved to the cage surface, accept Fe atom that bonded with carbon atoms of the structure. On the other hand, the doped atoms lose their magnetic moment while the temperature increases except for Fe, Pr, and Nd atoms. They keep their magnetic moment during temperature up to 300k in $Si_{30}C_{30}$ (sphere) structure.

7.2 Future Work

The dissertation's findings emphasize the magnetic and electronic features of endohedral doping of C and SiC fullerenes. The structures are mostly spherical for $Si_{30}C_{30}$ and $Si_{35}C_{35}$ fullerenes. The endohedral doping atoms (Fe, Nb, Hf, Ta, W, La. Ce, Pr, and Nd) demonstrated that they had a high value of magnetic moment. From the observed trend, doping atoms in larger fullerenes, such as $Si_{40}C_{40}$ can be investigated. In addition, AIMD can be utilized to assess the dynamical stabilities of the hydrogen passivated metal doped fullerene structures of all sizes.

Endohedral doping in spherical $Si_{30}C_{30}$ and $Si_{35}C_{35}$ structure can be employed in spintronic applications and memory devices. Further research might also focus on retaining the doping atoms into the center of spherical $Si_{30}C_{30}$ and $Si_{35}C_{35}$ fullerene while increasing the temperature, and interactions of the doped metal atoms between fullerene dimers.

Appendix A

A. Canonical (NVT) Ensemble Calculation of Endoherally sphere strucutre at 1PS

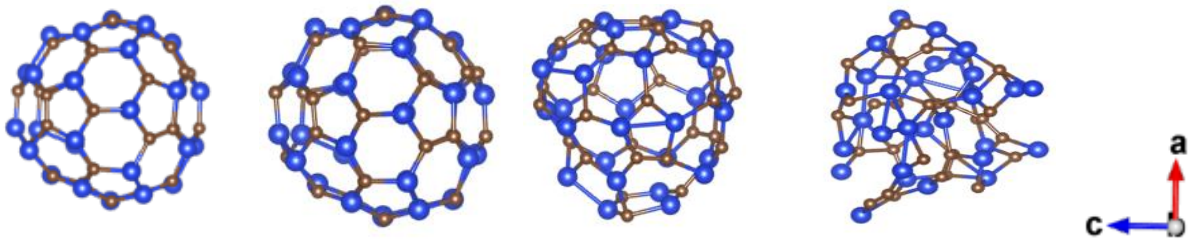

(a) 0K (b) 2400K (c) 2500K (d) 2800K

Figure 1. is the regular DFT calculation at 0K for the figure (a), the Molecular Dynamic simulation starting from 100K, and we are showing here the MD Simulation at 2400K (b), start melting point at 2500K (c), and melting structure at 2800K (d), where the blue atoms are Silicon (Si), and the black atoms are Carbon (C).

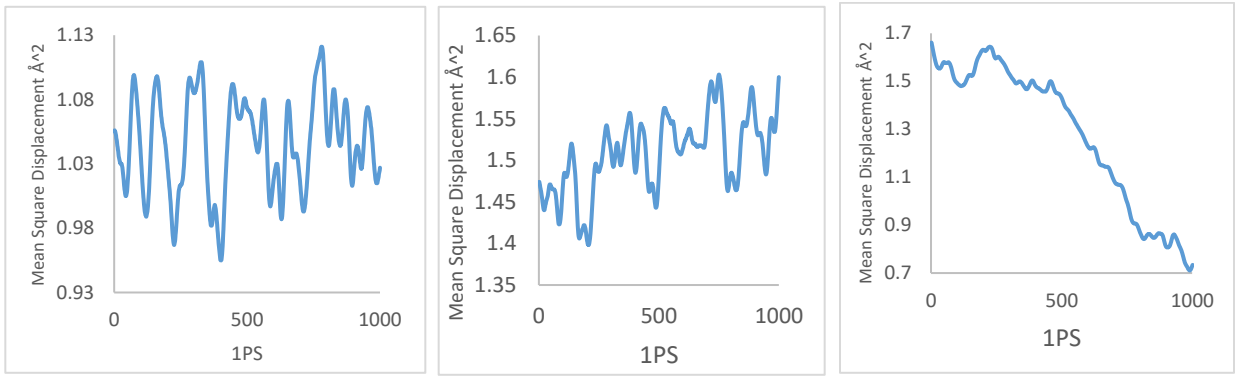

(a) (b) (c)

Figure 2. shows the Mean Square Displacement $Å^2$ (MSDs) up to 1PS long ab intiao MD (AIMD) trajectories of sphere structure. (a) before melting point, which at 2400K, (b)) the start melting point which at 2500K, and (c) melting point which at 2800K.

B. Canonical (NVT) and Microcanonical Ensemble Calculation (NVE) of Endoherally dpoing Transition Metal Atoms at 1PS

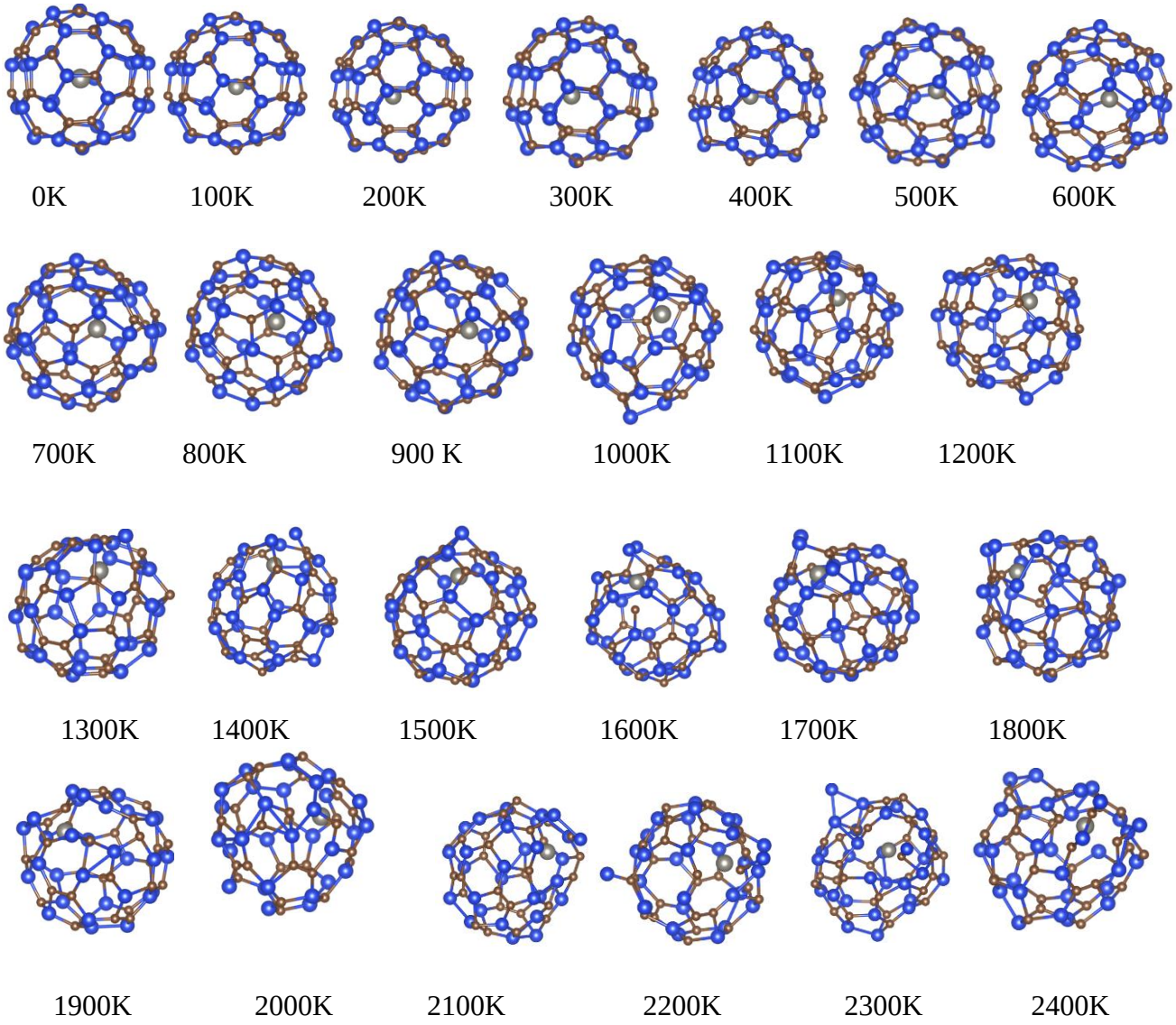

Figure.3: Ab-into MD simulation for W-sphere structure from 0 to at 2200K, at 1PS simulation.

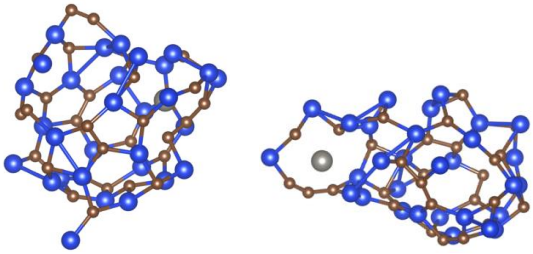

(a) (b)

Figure.4: Ab-into MD simulation for W-sphere structure at 2200K, (a) at 1PS simulation, and (b) at 2PS simulation.

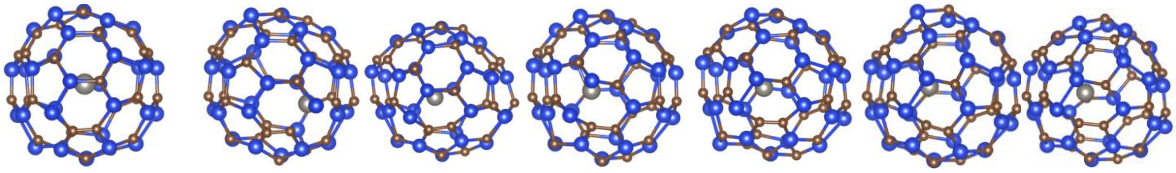

0K 0-100K 100K-200K 200K-300K 300K-400K 400K-500K 500K-600K

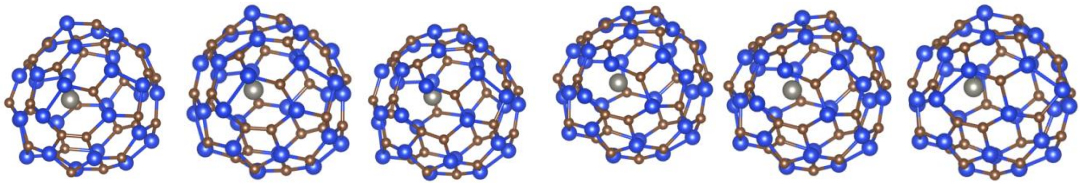

600K-700K 700K-800K 800K-900K 900K-1000K 1000K-1100K 1100K-1200K

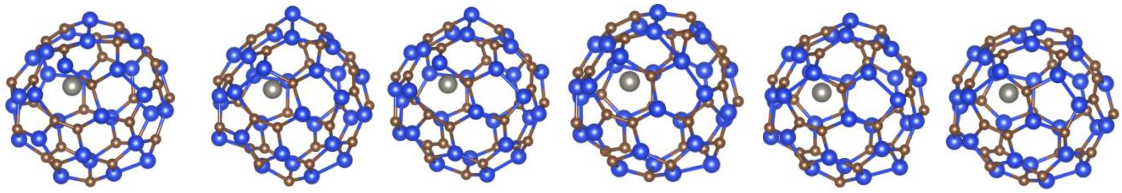

1200K-1300K 1300K-1400K 1400K-1500K 1500K-1600K 1600K-1700K 1700K-1800K

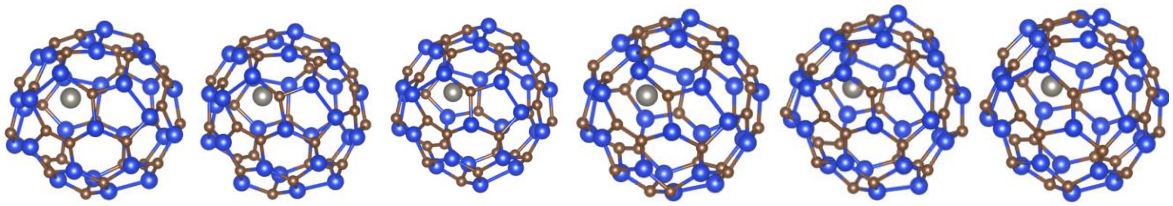

1900K-2000K 2000K-2100K 2100K-2200K 2200K-2300K 2300K-2400K 2400K-2500K

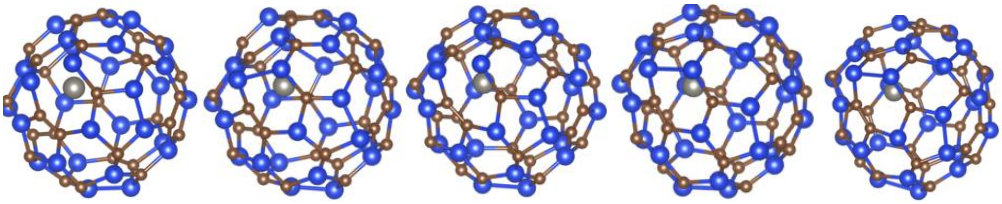

2500K-2600K 2600K-2700K 2700K-2800K 2800K-2900K 2900K-3000K

Figure 5: Ab-into MD simulation for microcanonical ensemble system of W-sphere structure from 0K to 3000K at 1PS simulation

(D). Canonical(NVT) at 2PS:

Fe-sphere

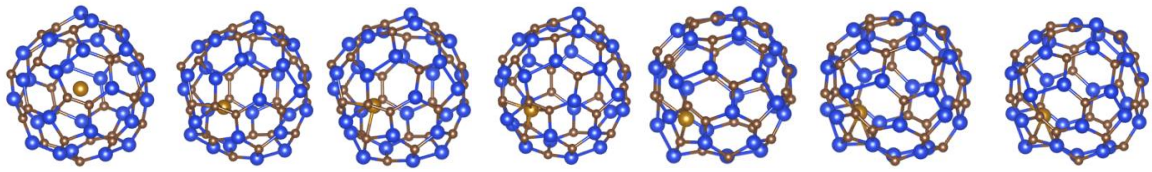

0K 50K 100K 150K 200K 250K 300K

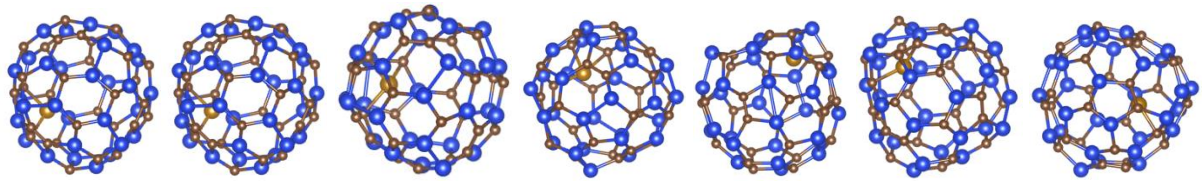

350K 400K 450K 500K 550K 600K 650K

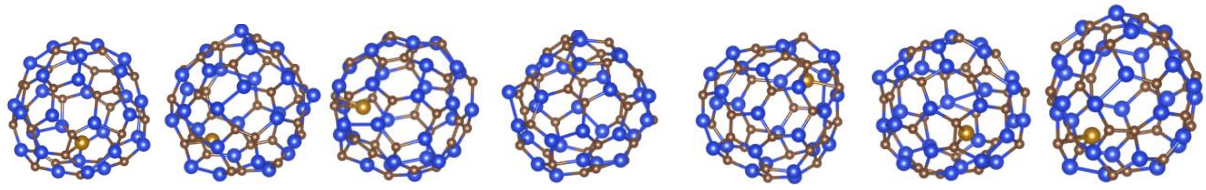

700K 750K 800K 850K 900K 950K 1000K

(a) Hf-shper

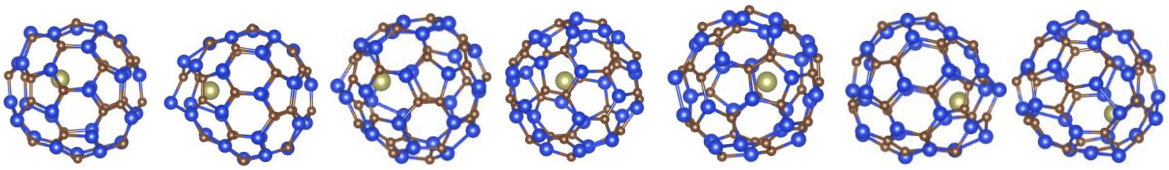

0K 50K 100K 150K 200K 250K 300K

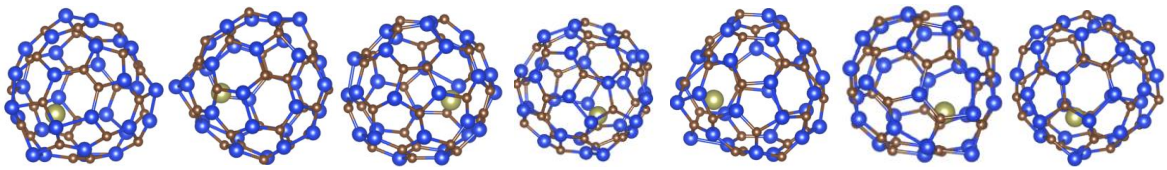

350K 400K 450K 500K 550K 600K 650K

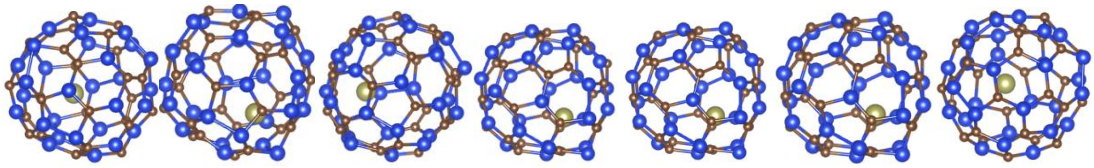

700K 750K 800K 850K 900K 950K 1000K

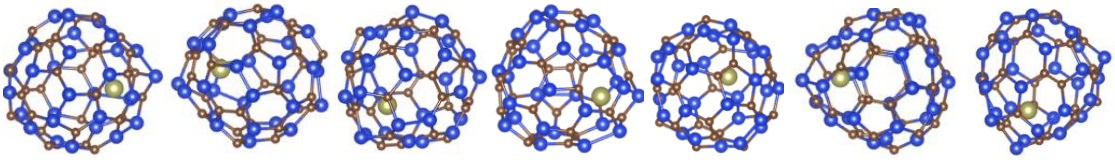

1050K 1100K 1150K 1200K 1250K 1300K 1350K

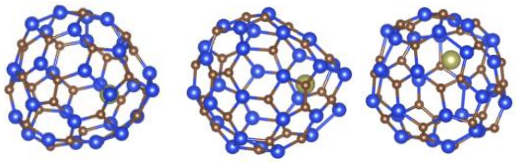

1400K 1450K 1500K

(b) Nb-sphere

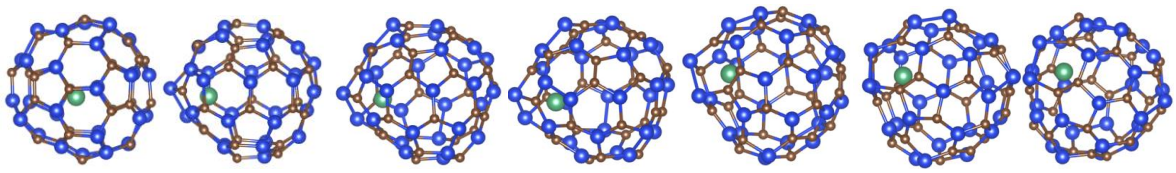

0K 50K 100K 150K 200K 250K 300K

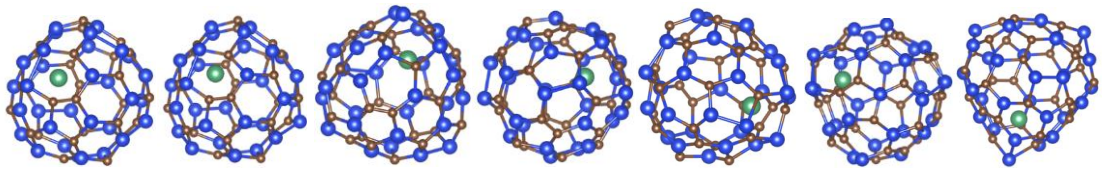

350K 400K 450K 500K 550K 600K 650K

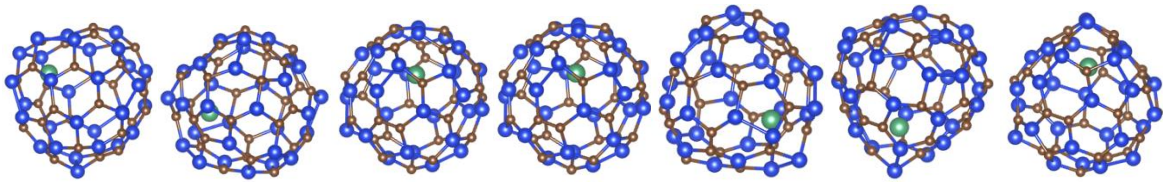

700K 750K 800K 850K 900K 950K 1000K

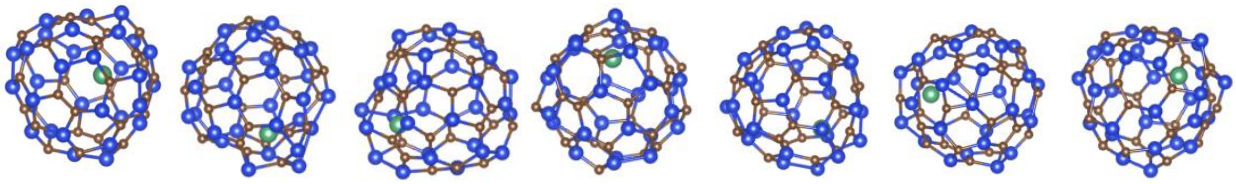

1050K 1100K 1150K 1200K 1250K 1300K 1350K

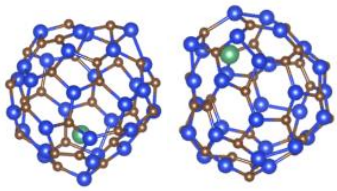

1400K 1450K

(c) Ta-sphere.

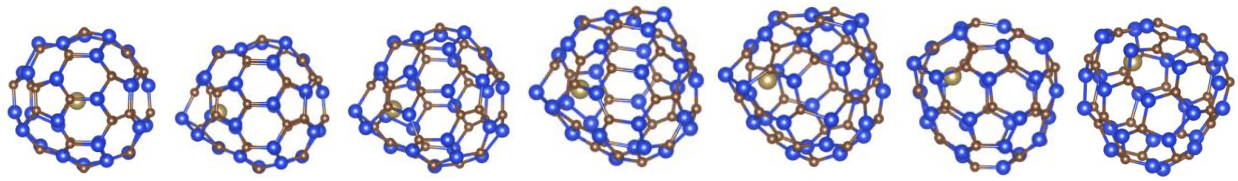

0K 50K 100K 150K 200K 250K 300K

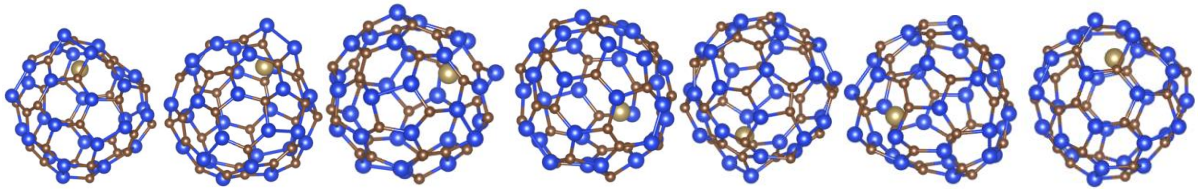

350K 400K 450K 500K 550K 600K 6 50K

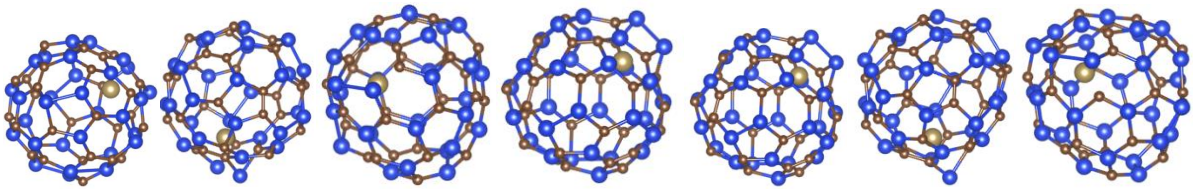

700K 750K 800K 850K 900K 950K 1000K

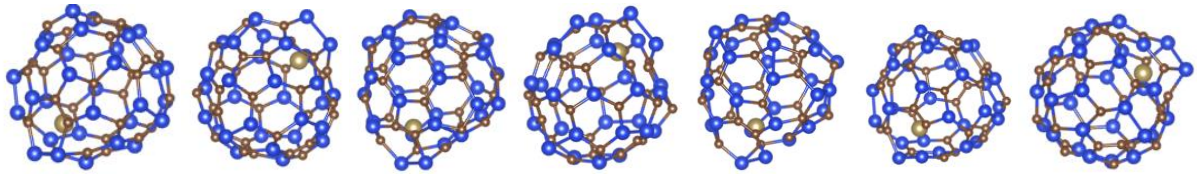

1050 1100K 1150K 1200K 1250K 1300K 1350K

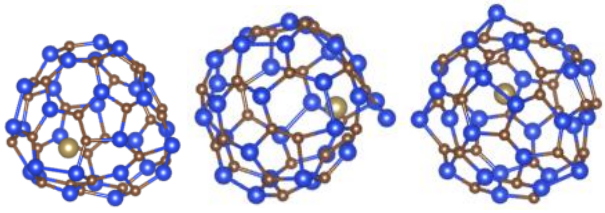

1400K 1450K 1500K

(d) W-sphere

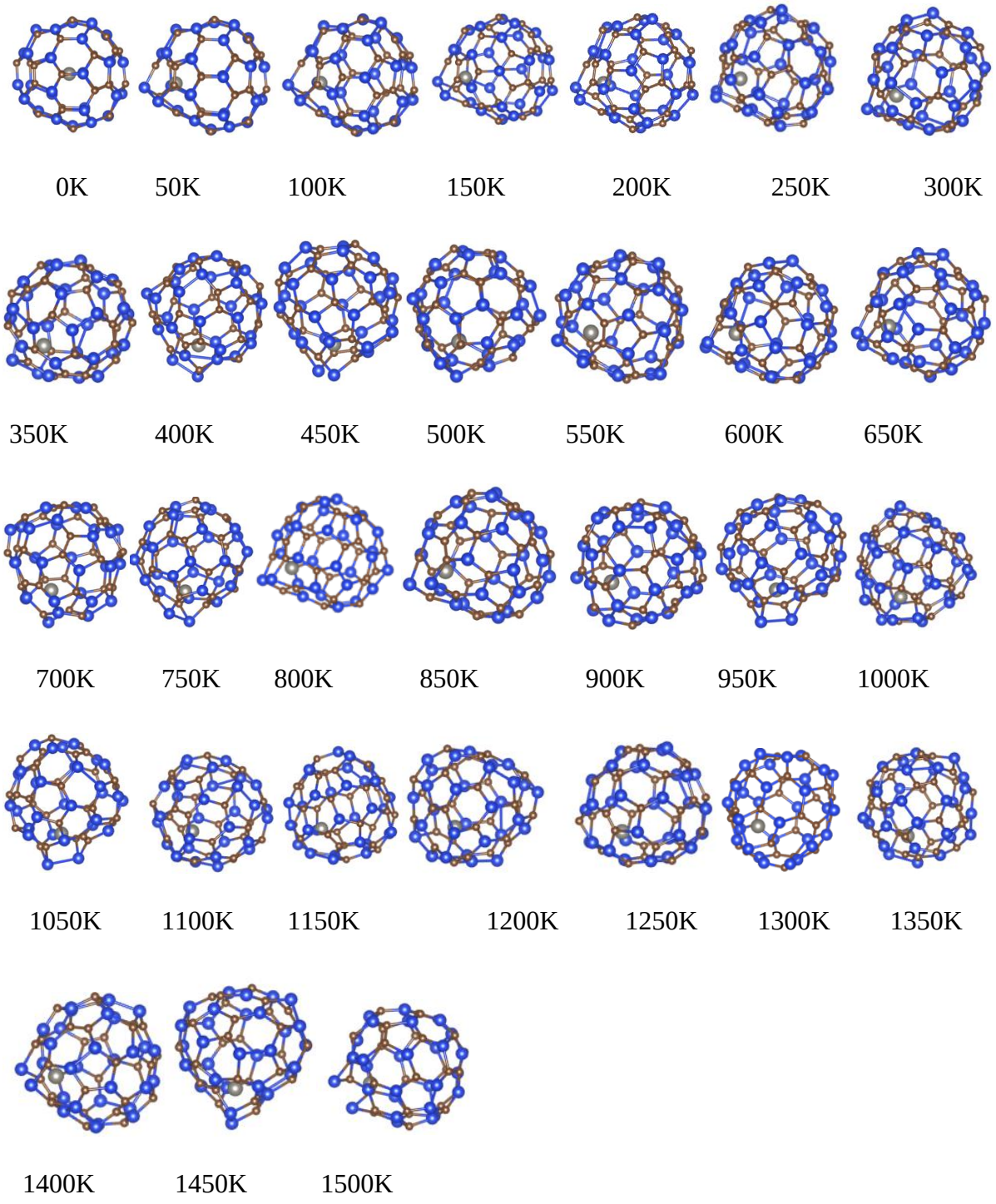

Figure. 6: Snapshots of Ab-into MD simulation for microcanonical ensemble system of X-sphere structure; X=Fe, Hf, Nb, Ta, and W atoms from 0K to 1500K at 2PS simulation and 50K interval.

References:

[1] V. A. Dediu, L. E. Hueso, I. Bergenti, and C. Taliani, "Spin routes in organic semiconductors," *Nature Materials*, vol. 8, no. 9, pp. 707–716, 2009.

[2] S. Mallik *et al.*, "Tuning spinterface properties in iron/fullerene thin films," *Nanotechnology*, vol. 30, no. 43, p. 435705, Oct. 2019.

[3] R. Lin, F. Wang, M. Wohlgenannt, C. He, X. Zhai, and Y. Suzuki, "Organic spin-valves based on fullerene C60," *Synthetic Metals*, vol. 161, no. 7–8, pp. 553–557, Apr. 2011.

[4] R. E. Smalley and B. I. Yakobson, "The future of the fullerenes," *Solid State Communications*, vol. 107, no. 11, pp. 597–606, 1998.

[5] H. B. and M. S. Palmer, "Vaporization of carbon," *chemistry and physics of carbon*, vol. 4, no. 01, pp. 85–135, Dec. 1968.

[6] W. Weltner and R. J. Van Zee, "Carbon Molecules, Ions, and Clusters," *Chemical Reviews*, vol. 89, no. 8, pp. 1713–1747, Dec. 1989.

[7] H. W. Kroto, J. R. Heath, S. C. O'Brien, R. F. Curl, and R. E. Smalley, "C60: Buckminsterfullerene," *Nature*, vol. 318, no. 6042, pp. 162–163, Nov. 1985.

[8] H. W. Kroto, A. W. Allaf, and S. P. Balm, "C60: Buckminsterfullerene," *Chemical Reviews*, vol. 91, no. 6, pp. 1213–1235, 1991.

[9] S. L. Ren *et al.*, "Ellipsometric determination of the optical constants of C60 (Buckminsterfullerene) films," *Applied Physics Letters*, vol. 59, no. 21, pp. 2678–2680, 1991.

[10] T. G. Schmalz, W. A. Seitz, D. J. Klein, and G. E. Hite, “Elemental Carbon Cages,” *Journal of the American Chemical Society*, vol. 110, no. 4, pp. 1113–1127, 1988.

[11] S. Saha and J. Jose, “Endohedral metallofullerenes Recent citations Sensitivity of correlation effects and Shannon entropy in Be@C60 to the nature of confinement potentials,” 2000.

[12] M. Prato, “[60]Fullerene chemistry for materials science applications,” *Journal of Materials Chemistry*, vol. 7, no. 7, pp. 1097–1109, 1997.

[13] T. Da Ros and M. Prato, “Medicinal chemistry with fullerenes and fullerene derivatives,” *Chemical Communications*, no. 8, pp. 663–669, 1999.

[14] S. Pfuetzner, J. Meiss, A. Petrich, M. Riede, and K. Leo, “Improved bulk heterojunction organic solar cells employing C70 fullerenes,” *Applied Physics Letters*, vol. 94, no. 22, 2009.

[15] SEEMA THAKRAL* AND R. M. MEHTA, “F ullerenes : An Introduction and Overview of Their Biological Properties,” *Indian Journal of Pharmaceutical Sciences*, vol. 68, pp. 13–19, 2006.

[16] D. Zhang, P. Tian, X. Chen, J. Lu, and R. Huang, “Pressure-crystallized piezoelectric structures in binary fullerene C70/poly(vinylidene fluoride) based composites,” *Journal of Applied Polymer Science*, vol. 130, no. 3, pp. 1823–1833, Nov. 2013.

[17] C. J. Brabec, S. Gowrisanker, J. J. M. Halls, D. Laird, S. Jia, and S. P. Williams, “Polymer-fullerene bulk-heterojunction solar cells,” *Advanced Materials*, vol. 22, no. 34, pp. 3839–3856, 2010.

[18] M. Hetzer, S. Bayerl, X. Camps, O. Vostrowsky, A. Hirsch, and T. M. Bayerl, “Fullerenes in membranes: Structural and dynamic effects of lipophilic C60 derivatives in phospholipid bilayers,” *Advanced Materials*, vol. 9, no. 11, pp. 913–917, 1997.

[19] A. Hirsch, I. Lamparth, T. Grösser, and H. R. Karfunkel, “Regiochemistry of Multiple Additions to the Fullerene Core: Synthesis of a Tb-Symmetric Hexakisadduct of C60 with Bis(ethoxycarbonyl)methylene,” *Journal of the American Chemical Society*, vol. 116, no. 20, pp. 9385–9386, 1994.

[20] R. B. R. M. Vallant and M. N.-H. M. R. Z. S. C. W. H. G. K. Bonn, “Medicinal applications of fullerenes,” *International Journal of Nanomedicine*, vol. 4, no. 2, pp. 639–649, 2007.

[21] A. Candian, “The Origins of Buckyballs in Space,” *Nature*, vol. 574, no. 7779, pp. 490–491, 2019.

[22] L. Wang, D. Li, and D. Yang, “Fully exohydrogenated Si60 fullerene cage,” *Molecular Simulation*, vol. 32, no. 8, pp. 663–666, 2006.

[23] E. Bainglass, C. L. Mayfield, and M. N. Huda, “Weakening of Si-Si bonding in exohydrogenated Si60 nanoclusters,” *Chemical Physics Letters*, vol. 684, pp. 60–66, 2017.

[24] M. Matsubara and C. Massobrio, “Stable highly doped C60-mSim heterofullerenes: A first principles study of C40Si20, C36Si 24, and C30Si30,” *Journal of Physical Chemistry A*, vol. 109, no. 19, pp. 4415–4418, 2005.

[25] A. Srinivasan, M. N. Huda, and A. K. Ray, “A density functional theoretic study of novel

silicon-carbon fullerene-like nanostructures: Si40C20, Si60C20, Si36C24, and Si60C24," *European Physical Journal D*, vol. 39, no. 2, pp. 227–236, 2006.

[26] A. Srinivasan, M. N. Huda, and A. K. Ray, "Silicon-carbon fullerenelike nanostructures: An ab initio study on the stability of Si60 C2n (n=1,2) clusters," *Physical Review A - Atomic, Molecular, and Optical Physics*, vol. 72, no. 6, pp. 1–10, 2005.

[27] J. L. Li *et al.*, "Polymerization of silicon-doped heterofullerenes: An ab initio study," *Chinese Physics Letters*, vol. 25, no. 1, pp. 246–249, 2008.

[28] M. N. Huda and A. K. Ray, "Novel silicon-carbon fullerene-like cages A class of sp3 − sp2 covalent-ionic hybridized nanosystems," *THE EUROPEAN PHYSICAL JOURNAL D*, vol. 68, pp. 63–68, 2004.

[29] 6 ZHONGFANG CHEN, 1, 2 HAIJUN JIAO, 3, 4 GOTTHARD SEIFERT, 5 ANSELM H. C. HORN and 8 PAUL VON RAGUE´ SCHLEYER1 DENGKE YU, 7 TIM CLARK, 6 WALTER THIEL, "The Structure and Stability of Si60 and Ge60 Cages: A Computational Study ZHONGFANG," *J Comput Chem*, vol. 24, no. 948, p. 953, Dec. 2003.

[30] Q. Sun, Q. Wang, P. Jena, B. K. Rao, and Y. Kawazoe, "Stabilization of Si60 Cage Structure," *Physical Review Letters*, vol. 90, no. 13, p. 4, 2003.

[31] M. N. Huda and A. K. Ray, "Carbon dimer in silicon cage: A class of highly stable silicon carbide clusters," *Physical Review A - Atomic, Molecular, and Optical Physics*, vol. 69, no. 1, pp. 112011–112014, 2004.

[32] H. J. Alathlawi, N. D. Alkhaldi, and M. N. Huda, "Effects of Hydrogen Passivation on

Fullerene-Derived Si30C30 Clusters," *Frontiers in Materials*, vol. 7, no. September, pp. 1–16, Sep. 2020.

[33] M. Matsubara and C. Massobrio, "First principles study of extensive doping of C60 with silicon," *Materials Science and Engineering C*, vol. 26, no. 5–7, pp. 1224–1227, 2006.

[34] R. Scipioni, M. Matsubara, E. Ruiz, C. Massobrio, and M. Boero, "Thermal behavior of Si-doped fullerenes vs their structural stability at T = 0 K: A density functional study," *Chemical Physics Letters*, vol. 510, no. 1–3, pp. 14–17, 2011.

[35] Z. Wang, S. Aoyagi, H. Omachi, R. Kitaura, and H. Shinohara, "Isolation and Structure Determination of a Missing Endohedral Fullerene La@C 70 through In Situ Trifluoromethylation," *Angewandte Chemie*, vol. 128, no. 1, pp. 207–210, Jan. 2016.

[36] H. J. Chandler, M. Stefanou, E. E. B. Campbell, and R. Schaub, "Li@C60 as a multi-state molecular switch," *Nature Communications*, vol. 10, no. 1, p. 2283, Dec. 2019.

[37] A. F. Hebard *et al.*, "Superconductivity at 18 K in potassium-doped C60," *Nature*, vol. 350, no. 6319, pp. 600–601, Apr. 1991.

[38] M. Guo, X. Li, Y. Yao, J. Zhuang, and Q. Meng, "A non-isolated pentagon rule C82 cage stabilized by a stretched Sc3N cluster," no. 39 663, pp. 4150–4153, 2021.

[39] E. S. Stevenson, P. W. Fowler, T. Heine, J. C. Duchamp, G. Rice, T. Glass, K. Harich and H. C. D. Hajdu, R. Bible, "A stable non-classical metallofullerene family," *Nature*, vol. 408, no. November, pp. 427–428, 2000.

[40] H. Tsunoyama *et al.*, "Development of Integrated Dry-Wet Synthesis Method for Metal Encapsulating Silicon Cage Superatoms of M@Si16 (M = Ti and Ta)," *Journal of*

Physical Chemistry C, vol. 121, no. 37, pp. 20507–20516, 2017.

[41] W. de Heer, "The physics of simple metal clusters: experimental aspects and simple models," *Reviews of Modern Physics*, vol. 65, no. 3, pp. 611–676, 1993.

[42] D. M. Guldi, M. Prato, and S. Farmaceutiche, "Excited-State Properties of C 60 Fullerene Derivatives," *Chemical Reviews*, vol. 33, no. 10, pp. 695–703, 2000.

[43] T. Ohtsuki *et al.*, "Insertion of Be Atoms in C60 Fullerene Cages: Be@C60," *Physical Review Letters*, vol. 77, no. 17, pp. 3522–3524, 1996.

[44] S. Mallik, S. Mattauch, M. K. Dalai, T. Brückel, and S. Bedanta, "Effect of magnetic fullerene on magnetization reversal created at the Fe/C60 interface," *Scientific Reports*, vol. 8, no. 1, pp. 1–10, 2018.

[45] F. Bologna, E. J. Mattioli, A. Bottoni, F. Zerbetto, and M. Calvaresi, "Interactions between Endohedral Metallofullerenes and Proteins: The Gd@C60-Lysozyme Model," *ACS Omega*, vol. 3, no. 10, pp. 13782–13789, 2018.

[46] M. Gobbi, "Spintronic devices based on fullerene C 60," 2013.

[47] W. I. F. David *et al.*, "Crystal structure and bonding of ordered C60," *letters to nature*, vol. 353, pp. 147–149, 1991.

[48] R. S. Ruoff, D. S. Tse, R. Malhotra, and D. C. Lorents, "Solubility of C60 in a variety of solvents," *Journal of Physical Chemistry*, vol. 97, no. 13, pp. 3379–3383, 1993.

[49] Y. Yang *et al.*, "Reversible Fullerene Electrochemistry: Correlation with the HOMO-LUMO Energy Difference for C60, C70, C76, C78, and C84," *Journal of the American Chemical Society*, vol. 117, no. 29, pp. 7801–7804, 1995.

[50] X. Zhang and X. D. Li, “Effect of the position of substitution on the electronic properties of nitrophenyl derivatives of fulleropyrrolidines: Fundamental understanding toward raising LUMO energy of fullerene electron-acceptor,” *Chinese Chemical Letters*, vol. 25, no. 4, pp. 501–504, 2014.

[51] S. C. O’brien, J. R. Heath, H. W. Kroto, R. F. Curl, and R. E. Smalley, “A reply to ‘magic numbers in Cn+ and Cn- abundance distribution’ based on experimental observations,” *Chemical Physics Letters*, vol. 132, no. 1, pp. 99–102, 1986.

[52] F. K. Tittel, R. F. Curl, H. W. Kroto, and R. E. Smalley, “Negative Carbon Cluster Ion Beams : NEW EVIDENCE FOR THE SPECIAL NATURE OF C60,” vol. 126, no. 2, pp. 215–217, 1986.

[53] R. H. Xie, L. Jensen, G. W. Bryant, J. Zhao, and V. H. Smith, “Structural, electronic, and magnetic properties of heterofullerene C48B12,” *Chemical Physics Letters*, vol. 375, no. 5–6, pp. 445–451, 2003.

[54] K. Srinivasu, N. K. Jena, and S. K. Ghosh, “Electronic structure, stability and non-linear optical properties of aza-fullerenes C 60-2n N 2n (n=1–12),” *AIP Advances*, vol. 2, no. 4, p. 042111, Dec. 2012.

[55] A. V Nikolaev, T. J. S. Dennis, K. Prassides, and A. K. Soper, “Molecular structure of the C70 fullerene,” vol. 223, no. June, pp. 143–148, 1994.

[56] K. J. Moor, D. C. Valle, C. Li, and J. H. Kim, “Improving the visible light photoactivity of supported fullerene photocatalysts through the use of [C70] fullerene,” *Environmental Science and Technology*, vol. 49, no. 10, pp. 6190–6197, 2015.

[57] Susumu Saito and Atsushi Oshiyama, “Electronic and geometric structures of C7o,” vol. 44, no. 20, pp. 532–535, 1991.

[58] H. Hiura, T. Miyazaki, and T. Kanayama, “Formation of metal-encapsulating Si cage clusters,” *Physical Review Letters*, vol. 86, no. 9, pp. 1733–1736, 2001.

[59] X. F. Duan and L. W. Burggraf, “Theoretical investigation of stabilities and optical properties of Si12C12 clusters,” *Journal of Chemical Physics*, vol. 142, no. 3, 2015.

[60] M. N. Huda and A. K. Ray, “Theoretical study of SiC nanostructures: Current status and a new theoretical approach,” *Journal of Computational and Theoretical Nanoscience*, vol. 9, no. 11. pp. 1881–1905, 2012.

[61] C. L. Mayfield and M. N. Huda, “The effect of hydrogen passivation on Si nanocrystals: Surface and spin states,” *Computational and Theoretical Chemistry*, vol. 1019, no. 1, pp. 125–131, 2013.

[62] B. I. Dunlap, J. L. Ballester, and P. P. Schmidt, “Interactions between C60 and endohedral alkali atoms,” *Journal of Physical Chemistry*, vol. 96, no. 24, pp. 9781–9787, 1992.

[63] V. Bernshtein and I. Oref, “Surface migrations of endohedral Li+ on the inner wall of C60,” *Physical Review A - Atomic, Molecular, and Optical Physics*, vol. 62, no. 3, pp. 033201–033201, 2000.

[64] H. Suzuki *et al.*, “ Rotational dynamics of Li + ions encapsulated in C 60 cages at low temperatures ,” *Physical Chemistry Chemical Physics*, vol. 18, no. 46, pp. 31384–31387, 2016.

[65] E. E. B. Campbell, M. Fanti, I. V. Hertel, Rolf Mitzner, and F. Zerbetto, “The

hyperpolarisability of an endohedral fullerene: Li@C60," *Chemical Physics Letters*, vol. 288, no. 1, pp. 131–137, 1998.

[66] N. Sakamoto, T. Muranaka, T. Akune, M. Baenitz, and K. Lüders, "Magnetic Relaxation in Superconducting Fullerenes Rb3C60 and K2RbC60," in *Advances in Superconductivity XI*, Tokyo: Springer Japan, 1999, pp. 629–632.

[67] A. Nakagawa *et al.*, "Crystalline functionalized endohedral C60 metallofullerides," *Nature Communications*, vol. 9, no. 1, 2018.

[68] Y. Chai *et al.*, "Fullerenes with metals inside," *Journal of Physical Chemistry*, vol. 95, no. 20, pp. 7564–7568, 1991.

[69] R. D. Johnson, M. S. de Vries, J. Salem, D. S. Bethune, and C. S. Yannoni, "Electron paramagnetic resonance studies of lanthanum-containing C82," *Nature*, vol. 355, no. 6357, pp. 239–240, Jan. 1992.

[70] H. Shinohara, H. Sato, Y. Saito, M. Ohkohchi, and Y. Ando, "Mass spectroscopic and ESR characterization of soluble yttrium-containing metallofullerenes YC82 and Y2C82," *Journal of Physical Chemistry*, vol. 96, no. 9, pp. 3571–3573, 1992.

[71] H. Shinohara *et al.*, "Encapsulation of a scandium trimer in C82," *Nature*, vol. 357, no. 6373, pp. 52–54, 1992.

[72] M. Takata *et al.*, "Confirmation by X-ray diffraction of the endohedral nature of the metallofullerene Y@C82," *Nature*, vol. 377, no. 6544, pp. 46–49, 1995.

[73] L. Moro, R. S. Ruoff, C. H. Becker, D. C. Lorents, and R. Malhotra, "Studies of metallofullerene primary soots by laser and thermal desorption mass spectrometry," *The*

Journal of Physical Chemistry, vol. 97, no. 26, pp. 6801–6805, Jul. 1993.

[74] T. Yang, X. Zhao, and S. Nagase, "Quantum chemical insight of the dimetallic sulfide endohedral fullerene Sc2S@C70: Does it possess the conventional D5h cage?," *Chemistry - A European Journal*, vol. 19, no. 8, pp. 2649–2654, Feb. 2013.

[75] M. Saunders, H. A. Jiménez-Vázquez, R. J. Cross, S. Mroczkowski, D. I. Freedberg, and F. A. L. Anet, "Probing the interior of fullerenes by 3He NMR spectroscopy of endohedral 3He@C60 and 3He@C70," *Nature*, vol. 367, no. 6460, pp. 256–258, 1994.

[76] M. Saunders *et al.*, "Incorporation of helium, neon, argon, krypton, and xenon into fullerenes using high pressure," *Journal of the American Chemical Society*, vol. 116, no. 5, pp. 2193–2194, Mar. 1994.

[77] A. D. McLean and G. S. Chandler, "Contracted Gaussian basis sets for molecular calculations. I. Second row atoms, Z=11-18," *The Journal of Chemical Physics*, vol. 72, no. 10, pp. 5639–5648, 1980.

[78] P. Hohenberg and W. Kohn, "Inhomogeneous Electron Gas," *Physical Review*, vol. 136, no. 3B, pp. B864–B871, Nov. 1964.

[79] W. Kohn and L. J. Sham, "Self-Consistent Equations Including Exchange and Correlation Effects," *Physical Review*, vol. 140, no. 4A, pp. A1133–A1138, Nov. 1965.

[80] G. Kresse and D. Joubert, "From ultrasoft pseudopotentials to the projector augmented-wave method," *physical review B*, vol. 59, no. 3, pp. 1758--1775, 1999.

[81] P. E. Blochl, "Projector augmented-wrave method P," *physical review B*, vol. 50, no. 24, pp. 17953–17979, 1994.

[82] D. C. Langreth and M. J. Mehl, “Beyond the local-density approximation in calculations of ground-state electronic properties,” *Physical Review B*, vol. 28, no. 4, pp. 1809–1834, 1983.

[83] P. A. M. Dirac, “Note on Exchange Phenomena in the Thomas Atom,” *Mathematical Proceedings of the Cambridge Philosophical Society*, vol. 26, no. 3, pp. 376–385, 1930.

[84] P. R. Antoniewicz and L. Kleinman, “Kohn-Sham exchange potential exact to first order in ρ(K→)/ρ0,” *Physical Review B*, vol. 31, no. 10, pp. 6779–6781, May 1985.

[85] K. Kim and K. D. Jordan, “Comparison of density functional and MP2 calculations on the water monomer and dimer,” *Journal of Physical Chemistry*, vol. 98, no. 40, pp. 10089–10094, 1994.

[86] P. J. Stephen, F. J. Devlin, C. F. Chabalowski, and M. J. Frisch, “Ab Initio Calculation of Vibrational Absorption,” *The Journal of Physical Chemistry*, vol. 98, no. 45, pp. 11623–11627, 1994.

[87] D. Marx and J. Hutter, *Ab Initio Molecular Dynamics*. Cambridge: Cambridge University Press, 2009.

[88] W. Kohn, A. D. Becke, and R. G. Parr, “Density functional theory of electronic structure,” *Journal of Physical Chemistry*, vol. 100, no. 31, pp. 12974–12980, 1996.

[89] A. D. Becke, “A new mixing of Hartree-Fock and local density-functional theories,” *The Journal of Chemical Physics*, vol. 98, no. 2, pp. 1372–1377, 1993.

[90] S. Chiodo, N. Russo, and E. Sicilia, “LANL2DZ basis sets recontracted in the framework of density functional theory,” *Journal of Chemical Physics*, vol. 125, no. 10, 2006.

[91] T. Takahashi *et al.*, “Pseudo-gap at the Fermi level in K3C60 observed by photoemission and inverse photoemission,” *Physical Review Letters*, vol. 68, no. 8, pp. 1232–1235, 1992.

[92] and P. C. E. Dresselhaus, M. S., G. Dresselhaus, *Science of fullerenes and carbon nanotubes*. 1996.

[93] J. B. V. S. b Anish Goel a,*, Jack B. Howard a,*, “Size analysis of single fullerene molecules by electron microscopy,” *elsevier science direct journals*, vol. 42, pp. 1907–1915, 2004.

[94] A. K. Soper, W. I. F. David, D. S. Sivia, T. J. S. Dennis, J. P. Hare, and K. Prassides, “A pair correlation function study of the structure of C60,” *Journal of Physics: Condensed Matter*, vol. 4, no. 28, pp. 6087–6094, 1992.

[95] B. xing Li, P. lin Cao, and D. lin Que, “Distorted icosahedral cage structure of clusters,” *Physical Review B - Condensed Matter and Materials Physics*, vol. 61, no. 3, pp. 1685–1687, 2000.

[96] M. Menon, “Generalized tight-binding molecular dynamics scheme for heteroatomic systems: Application to SimCn clusters,” *Journal of Chemical Physics*, vol. 114, no. 18, pp. 7731–7735, 2001.

[97] S. Yang, A. A. Popov, and L. Dunsch, “Violating the isolated pentagon rule (IPR): The endohedral non-IPR C 70 cage of Sc3N@C70,” *Angewandte Chemie - International Edition*, vol. 46, no. 8, pp. 1256–1259, 2007.

[98] M. N. Huda and A. K. Ray, “Evolution of SiC nanocluster from carbon fullerene: A density functional theoretic study,” *Chemical Physics Letters*, vol. 457, no. 1–3, pp. 124–

129, 2008.

[99] M. N. Huda, Y. Yan, and M. M. Al-Jassim, “On the existence of Si-C double bonded graphene-like layers,” *Chemical Physics Letters*, vol. 479, no. 4–6, pp. 255–258, 2009.

[100] D. Bravo-Zhivotovskii *et al.*, “The synthesis and isolation of a metal-substituted bis-silene,” *Angewandte Chemie - International Edition*, vol. 47, no. 23, pp. 4343–4345, 2008.

[101] P. De Padova, C. Quaresima, B. Olivieri, P. Perfetti, and G. Le Lay, “Sp2-like hybridization of silicon valence orbitals in silicene nanoribbons,” *Applied Physics Letters*, vol. 98, no. 8, pp. 96–99, 2011.

[102] W. Fa, C. Luo, and J. Dong, “Coexistence of ferroelectricity and ferromagnetism in tantalum clusters,” *Journal of Chemical Physics*, vol. 125, no. 11, 2006.

[103] L. A. Zheng, E. V. Barrera, and R. D. Shull, “Magnetic properties of the Co-C 60 and Fe-C 60 nanocrystalline magnetic thin films,” *Journal of Applied Physics*, vol. 97, no. 9, 2005.

[104] V. S. Stepanyuk and H. Wolfram, “Magnetic dimers of transition-metal atoms on the Ag (001) surface,” *physical review B*, vol. 54, no. 19, pp. 14121--14126, 1996.

[105] L. Fernandez *et al.*, “Influence of 4f filling on electronic and magnetic properties of rare earth-Au surface compounds,” *Nanoscale*, vol. 12, no. 43, pp. 22258–22267, 2020.

[106] G. Frenking and R. Tonner, “Theoretical chemistry: The six-bond bound,” *Nature*, vol. 446, no. 7133. pp. 276–277, 14-Mar-2007.

[107] X. Pang, D. Li, and A. Peng, “Application of rare-earth elements in the agriculture of

china and its environmental behavior in soil," *Journal of Soils and Sediments*, vol. 1, no. 2, pp. 124–129, 2001.

[108] T. Nakane *et al.*, "Origin of the difference between the high and low-Tc phases in the yttrium sesquicarbide system," *Science and Technology of Advanced Materials*, vol. 7, no. SUPPL. 1, pp. S99–S103, 2006.

[109] K. Seema and R. Kumar, "Structure of alkaline-earth and rare-earth metal-doped C60 solids," *Physica Scripta*, vol. 83, no. 2, 2011.

[110] H. S. C. O. B. Q. Zhang, Y. Liu, R. F. Curl, H. W. K. F. K. Tittel, and R. E. Smalley, "Lanthanum Complexes of Spheroidal Carbon Shells," *Journal of the American Chemical Society*, vol. 107, no. 25, pp. 7779–7780, 1985.

[111] A. K. Singh, V. Kumar, and Y. Kawazoe, "Stabilizing the silicon fullerene Si 20 by thorium encapsulation," *Physical Review B - Condensed Matter and Materials Physics*, vol. 71, no. 11, 2005.

[112] V. Kumar, A. K. Singh, and Y. Kawazoe, "Charged and magnetic fullerenes of silicon by metal encapsulation: Predictions from ab initio calculations," *Physical Review B - Condensed Matter and Materials Physics*, vol. 74, no. 12, 2006.

[113] R. Wu, C. Li, A. J. Freeman, and C. L. Fu, "Structural, electronic, and magnetic properties of rare-earth metal surfaces: hcp Gd(0001)," *Physical Review B*, vol. 44, no. 17, pp. 9400–9409, 1991.

[114] M. E. McHenry and D. E. Laughlin, "Magnetic Properties of Metals and Alloys," *Physical Metallurgy: Fifth Edition*, vol. 1, no. July, pp. 1881–2008, 2014.

[115] R. C. Taylor, T. R. McGuire, J. M. D. Coey, and A. Gangulee, “Magnetic properties of amorphous neodymium-transition-metal films,” *Journal of Applied Physics*, vol. 49, no. 5, pp. 2885–2893, May 1978.

[116] İ. Şabikoğlu *et al.*, “The effect of neodymium substitution on the structural and magnetic properties of nickel ferrite,” *Progress in Natural Science: Materials International*, vol. 25, no. 3, pp. 215–221, Jun. 2015.

[117] G. Kresse and J. Furthmüller, “Efficiency of ab-initio total energy calculations for metals and semiconductors using a plane-wave basis set,” *Computational Materials Science*, vol. 6, no. 1, pp. 15–50, 1996.

[118] and M. E. John P. Perdew, Kieron Burke, “Generalized Gradient Approximation Made Simple,” *Physical Review Letters*, vol. 77, no. 18, pp. 3865–3868, 1996.

[119] J. P. Perdew, K. Burke, and Y. Wang, “Generalized gradient approximation for the exchange-correlation hole of a many-electron system,” *physical review B*, vol. 54, no. 23, pp. 16533--16539, 1996.

[120] D. Wei and D. R. Salahub, “Hydrated proton clusters: Ab initio molecular dynamics simulation and simulated annealing,” *Journal of Chemical Physics*, vol. 106, no. 14, pp. 6086–6094, 1997.

[121] R. Car and M. Parrinello, “Structural, dymanical, and electronic properties of amorphous silicon: An ab initio molecular-dynamics study,” *Physical Review Letters*, vol. 60, no. 3, pp. 204–207, 1988.

[122] M. E. Tuckerman, “Ab initio molecular dynamics: Basic concepts, current trends and

novel applications," *Journal of Physics Condensed Matter*, vol. 14, no. 50, 2002.